ALMA MATER STUDIORUM · UNIVERSITÀ DI BOLOGNA

Scuola di Scienze
Corso di Laurea Magistrale in Fisica del Sistema Terra

Data analysis and simulations of VIRTIS Venus spectra

Relatore: Presentata da:

Prof. Tiziano Maestri   Davide Magurno

Correlatori:

Dott. Davide Grassi
Dott. Giuseppe Sindoni

Sessione I
Anno Accademico 2014/2015

Sommario

Venus Express è la prima missione dell'Agenzia Spaziale Europea dedicata al pianeta Venere ed è anche la più lunga missione che ne abbia mai studiato l'atmosfera. VIRTIS (Visible and Infrared Thermal Imaging Spectrometer), a bordo di Venus Express, è uno spettrometro in grado di operare da $0.25\,\mu m$ a $5\,\mu m$. Nel periodo 2006-2011 ha ricavato un'enorme mole di dati nelle più disparate condizioni osservative. A tutt'oggi però le numerose osservazioni effettuate al lembo sono utilizzate soprattutto per studiare la componente gassosa dell'atmosfera mentre risultano poco utilizzate per quanto riguarda lo studio delle nubi e delle hazes sovrastanti, specialmente di notte. Gli spettri al lembo osservati a quote mesosferiche (70-100 km) sono dominati dalla radianza proveniente dalle nubi sottostanti e scatterata in direzione dello strumento dalle particelle di haze. L'interpretazione degli spettri al lembo non può quindi prescindere dalla caratterizzazione dell'intera colonna atmosferica.

L'obiettivo della tesi è quello di proporre una metodologia valida per interpretare le osservazioni notturne al lembo al di sopra del top delle nubi e ricavare una caratterizzazione delle particelle scatteranti, combinando osservazioni al nadir e al lembo a breve distanza temporale. La caratterizzazione delle nubi è avvenuta su un campione adeguatamente selezionato di oltre 3700 osservazioni al nadir, in cui l'haze risulta ininfluente in termini di radianza osservata. È stato creato un ampio database di spettri sintetici modificando, rispetto ad un modello di riferimento iniziale, vari parametri di nube quali composizione chimica, numero e dimensione delle particelle. Alcune di queste modifiche non vengono generalmente prese in considerazione in letteratura, nonostante i numerosi punti ancora dibattuti in ambito scientifico. Un processo di best fit è stato applicato a ciascuna osservazione per stabilire quale modello potesse descrivere lo spettro osservato. Si è poi effettuata una analisi statistica sui risultati del campione. I modelli di nube più efficaci sono risultati avere una concentrazione di acido solforico molto elevata nelle nubi basse, pari al 96% in massa, e più bassa nella parte alta, tra 75% e 84%. Questo si discosta dal valore generalmente utilizzato del 75%, costante in tutta la nube, ma consente di ottenere un buon fit per alcune bande notoriamente problematiche. Rappresenta quindi un miglioramento nella modellizzazione delle nubi. Una volta ricavati i modelli per le radianze uscenti al nadir, si sono integrati tali risultati con uno studio mirato su poche osservazioni al lembo per ricavare informazioni sulle hazes. Le osservazioni al lembo sono state selezionate in modo da intercettare nel punto di tangenza la colonna atmosferica osservata al nadir, a breve distanza temporale. La conoscenza della radianza uscente al top delle nubi, ottenuta al nadir, consente di valutare i cambiamenti delle radianze scatterate al lembo come cambiamenti nelle proprietà dell'haze. I risultati di un modello Monte Carlo indicano che il numero e le dimensioni delle particelle di haze previste dal modello base sono troppo elevate e devono essere ridotte in maniera significativa. In particolare si è osservato un abbassamento della quota massima a cui sono presenti le hazes rispetto ad osservazioni diurne. Processi dinamici e chimici possono spiegare tale abbassamento.

Abstract

Venus Express was the first mission on Venus of the European Space Agency and it was also the longest mission ever devoted to its atmosphere. VIRTIS (Visible and Infrared Thermal Imaging Spectrometer), on board Venus Express, is a spectrometer operating from $0.25\,\mu m$ to $5\,\mu m$. In the period 2006-2011 it obtained a huge amount of data in many conditions of observation. Till now, the observations at limb are mainly used to study the gaseous component of the atmosphere but they are little used to study the clouds and the hazes above, especially at night. Limb spectra at mesospheric altitudes (70-100 km) are dominated by radiance leaving the clouds top and scattered into the line-of-sight by the upper haze particles. Therefore, the interpretation of limb spectra is not able to leave the characterization of the whole atmospheric column out of consideration.

The objective of the thesis is to suggest an efficient methodology to interpret night-time limb observations above the cloud top and obtain a characterization of the scattering particles above, by combining nadir and limb observations at short temporal distance. Clouds characterization was performed on an appropriate sample of more than 3700 nadir observations, in which hazes are non influential in terms of radiance units. It was created a comprehensive dataset of synthetic spectra by changing, in a reference initial model, clouds parameters such as chemical composition, number density and size of the cloud particles. Some of these changes are not usually considered in literature, despite the still open debate in the scientific community. A best fit process was applied to each observation to establish which model is able to describe the observed spectrum. Statistical analysis were then performed on the sample. The most effective models had a very high concentration of sulphuric acid in the lower clouds, equal to 96% by weight, and a lower concentration in the upper clouds, between 75% and 84%. This result is different to the widely used value of 75%, uniform within the whole cloud, but it permits to fit some features that are known to be problematic with the 75% model. Therefore, it represent an improvement in clouds modelling. Once the models for nadir radiances were established, they were integrated with a focused study on few limb observations to obtain information about the hazes. Limb observations were selected to intercept at the tangent point the atmospheric column observed at nadir, at short temporal distance. Knowledge of the upward radiance at the clouds top, obtained at nadir, permits to consider changes of limb scattered spectra as changes of the haze properties. Monte Carlo model results show that the haze particles number density and size of the reference model were too large and so they had to be substantially reduced. In particular, sinking of the hazes top was observed compared to observations at Venus' dayside. Dynamical and chemical processes could explain that sinking.

Contents

List of Figures

List of Tables

Introduction

Venus has been studied for a long time, from the early sixties to date, by over 40 missions. Nevertheless, properties of the thick cloud layers that globally cover the planet are still subject of debate, as well as the properties of the overlaying hazes (Mills et al., 2007; Takagi et al., 2014). The upper haze is very difficult to detect. When observed at limb, it scatters into the line-of-sight the radiance coming from the sun during the daytime or from the lower atmospheric layers at nighttime (de Kok et al., 2011). Therefore, knowledge of the incoming radiation is essential to retrieve hazes properties. Analysis of daytime observations is facilitated by the knowledge on sun emission and so they are the most used (Wilquet et al., 2009, 2012). During nighttime observation a lot of data is not used to infer cloud or limb properties. The main limit to the analysis of nocturnal limb observations is the lack of information on the upward radiance at haze altitude. VIRTIS spectrometer, on board the ESA's mission Venus Express, carried out a huge amount of observations from 2006 to 2011 both at limb and nadir and in presence or not of the sun radiance. VIRTIS nocturnal limb observations are mainly used to study the chemical content and temperature and gases profiles but a limited exploitation has been made to study the cloud layers and the upper hazes.

The main goal of the present work is to derive cloud and haze information from nocturnal data. In particular:

- A standard cloud and atmospheric state is defined and used as the reference model

- Sensitivity studies are performed on key parameters and variations on the upwelling radiances are evaluated

- A wide database of simulated VIRTIS nadir radiance spectra is computed for multiple clouds and atmospheric conditions

- Nadir data are divided into latitudinal/longitudinal bins and cloud properties are derived for each data by means of a statistical retrieval

- Nadir and limb data are co-located

- Limb simulations based on nadir retrieval are tested on data

Nadir results are compared to previous studies and in particular some new assumptions on sulphuric acid concentration along the vertical extent of the clouds and about the effective dimensions of the particles are discussed. Moreover, a methodology to make use of these co-located nadir and limb observations is proposed and suggests as combined observation might potentially add information content and assembled for future mission (on Earth or Planets).

The Thesis work is organised as follows. A brief description of Venus is given in Chapter 1. Venus Express and VIRTIS technical facts are described in Chapter 2. Description and modelling of Venus' atmosphere and computation of gaseous optical properties are given in Chapter 3. Description and modelling of clouds and hazes are given in Chapter 4. VIRTIS observations at nadir are analysed in Chapter 5 to characterize the main cloud deck and compute the upward radiance coming into the haze layer. Analysis of VIRTIS limb spectra above the cloud deck to describe the hazes is given in Chapter 6. Finally, Chapter 7 summarizes main results and conclusions of the thesis.

Chapter 1

Venus: an overview

Known since ancient times, Venus is the brightest natural object in the night sky after the moon. It is usually called "the morning star" or "the evening star", depending on the period, since it is, respectively, the last disappearing or the first appearing "star" in the sky. It is the second planet of the solar system from the Sun, orbiting between Mercury and Earth at a mean distance of 108.2 million kilometres or 0.72 Astronomical Units (AU). The sidereal orbital period lasts for 224.7 Earth days but Venus' rotation velocity is so slow that the sidereal rotation period lasts for 243 Earth days, more than a Venusian year, and the solar day lasts for 116.75 Earth days, the longest day of any planets. Venus is the only planet in the solar system with a retrograde rotation, that is its rotation axis inclination is 177.3° on the ecliptic plane and so the sun rises in the west and sets in the east. Due to its little obliquity and low eccentricity, about 0.0067, Venus isn't affect by evident seasonal variations although the slow rotation highly influences solar energy distribution between dayside and nightside of the planet. Some Venus facts are given in Table 1.1 and compared with Earth's ones.

Figure 1.1: Venus with visible and radar illumination. In the visible, the cloud deck prevents observation of the surface (Mariner 10 mission, top right). Radar highlights surface features; elevated areas are lighter (Magellan mission, bottom left).

Venus belong to the family of terrestrial planets, has no moons, no rings and no intrinsic magnetic field, although it has a magnetosphere which results from the interaction between the planet's ionosphere and the solar wind. Venus is the most similar to Earth in size and density, with mean values of 6051.8 km and 5243 kg/m^3 respectively.

Venus' surface is mainly composed of volcanic materials. Volcanic surface features are common, such as vast lava plains, fields of small lava domes and large volcanoes up to 11 km high, as they were observed by the NASA's Magellan radar in early nineties that mapped the 98% of the surface with high resolution (Figure 1.1). About 80% of the surface is covered by smooth volcanic plains whereas two highland areas are extended in the remaining surface: Ishtar Terra, about the size of Australia, in north polar region, and Aphrodite Terra, about the size of South America, straddling the equator and extending for almost 10000 km. Venus' volcanoes are thought to be still active and to actively influence the atmospheric composition.

Venus is surrounded by an atmosphere mainly composed of CO_2 and N_2, about 96.5% and 3.5% respectively, more similar to Mars' than Earth's. Minor gases are present in parts per million by volume (ppmv) scale such as SO_2, H_2O, CO and many others. Strong runaway greenhouse effect, in addition to mean insolation of about 2613.9 W/m^2, rises the surface temperature up to 735 K. Due to the high temperature, water is only observed as a gas, although oceans are believed to have existed in the past. Due to high atmospheric density (65 kg/m^3 at the surface), Venus' atmosphere has high thermal inertia so that little temperature variations are observed all over the planet, from the equator to the poles and from the dayside to the nightside. Three primary levels can be distinguished in Venus' atmosphere, depending on temperature (Figure 1.2):

Troposphere is the lower part of the atmosphere, up to 70 km about. Temperature in this layer decreases with altitude with a profile close to adiabatic. Only 2.5% of the incoming solar radiation is able to reach the surface because of the thick solid cloud deck which filled the layer between 48 km and 70 km. Clouds also prevent observations of the planet's surface in the visible. InfraRed (IR) radiation emitted by the ground is efficiently absorbed by the CO_2-rich atmosphere so temperature rises up to 735 K near the surface, where pressure reaches a value of 92.1 bar.

Mesosphere extends from 70 km to 100 km and is a near isothermal layer at about 200 K, separating troposphere from thermosphere. Venus' atmosphere lacks of ozone in appreciable quantity so a well defined stratosphere, as in the case of Earth, is not observed.

Thermosphere is the upper part of Venus' atmosphere, above 100 km. Differences in thermal structure of the layer are observed between dayside and nightside. Extreme UltraViolet (EUV) photodissociates CO_2 increasing temperature up to 300 K in the dayside, whereas the nightside temperature drops to a little over 100 K: for this reason the night thermosphere on Venus is often referred as the cryosphere. A pressure difference arises which give raise to a noon-to-midnight pressure gradient force. The dominant circulation pattern in the thermosphere is therefore a flow from the dayside to the nightside.

Venus' atmosphere is said to super-rotate because it takes about 4 Earth days to complete a rotation around the planet at the cloud top level, to be compared to the 243 Earth days of the solid planet rotation. How this atmospheric super-rotation forms and is maintained continues to be a topic of scientific investigation. Winds blow westward increasing speed with altitude up to about 100 m/s at clouds top and then decrease in the mesosphere, whereas winds at the surface blow at only few meters per second. Super-rotation, added to high atmospheric density, helps to reduce temperature differences between the dayside and nightside, which would be extreme without it. In addition to the super-rotation, a meridional circulation exists between equator and poles, driven by convection, but it is much slower than zonal circulation. Two big Hadley cells transport rising air from the equator toward the poles to the limit of about 60° latitudes, where air sinks isolating polar regions. Temperature in the upper

Figure 1.2: Venus' temperature profile.

troposphere at the limit of the Hadley cell is lower than in nearby latitudes, so this region is usually called "cold collar". Odd structures up to 50 K hotter than the collars, known as "hot dipole", lie within the cold polar collars. Such polar vortices are giant hurricane-like storms with two centres of rotation which are connected by distinct S-shaped cloud structures. The first vortex on the north pole was discovered by the Pioneer Venus mission in 1978 and the south pole vortex was observed in 2006 by Venus Express.

Clouds on Venus form a thick continuous layer all over the planet that lend it a visual geometric albedo of 0.67 and gives to Venus its typical brightness in the sky. Unlike Earth, Venus' clouds are mainly composed of an aqueous solution of sulphuric acid with high concentration, between 75% and 98% by weight, mainly formed by photochemical processes at around 60 km altitude. SO_2 and H_2O, mainly of volcanic origin and abundant in the atmosphere, are the precursor gases of these cloud particles. Cloud deck extends between 48 km and 70 km about and can be divided into three main layers, depending on the cloud droplets number density, size distribution and extinction coefficient, mainly obtained by the Pioneer missions in 1978 (Figure 1.3): upper clouds (roughly, 60-70 km altitude), middle clouds (50-60 km) and lower clouds (48-50 km). The upper cloud layer shows a bimodal particle size distribution, contains relatively small particles and their number density increases with decreasing altitude. In the middle cloud layer the particle number density sharply decreases but the extinction coefficient and the mass

Figure 1.3: Vertical structure of Venus cloud system, as seen by the cloud particle size spectrometer (LCPS) on board Pioneer Venus (Knollenberg and Hunten, 1980).

loading increase due to the presence of a third large kind of particle that turns the size distribution into a trimodal. In the lower cloud the particle number density rises again to values similar to the upper layer whereas mass loading and extinction coefficient grow even more due to the great increase of large mode particles. Below and above the main cloud deck, H_2SO_4 small aerosols form two optically thin haze layers of several kilometres depth.

Table 1.1: Venus and Earth facts

ORBITAL PARAMETERS	Venus	Earth
Orbit size (semi-major axis, 10^6 km)	108.209	149.598
Perihelion (10^6 km)	107.476	147.098
Aphelion (10^6 km)	108.943	152.098
Sidereal orbit period (Earth days)	224.7	365.3
Orbit circumference (10^6 km)	679.892	939.888
Mean orbit velocity (10^3 m/s)	35.020	29.783
Orbit inclination (°)	3.39	0.0
Orbit eccentricity	0.0067	0.0167
Equatorial inclination to orbit (°)	177.3	23.44
Sidereal rotation period (Earth days)	-243.018 (retrograde)	1

BULK PARAMETERS	Venus	Earth
Mean radius (km)	6051.8	6371.0
Equatorial circumference (10^3 km)	38.0246	40.0303
Volume (10^{11} km^3)	9.28415	10.8321
Mass (10^{24} kg)	4.8673	5.9726
Density (kg/m^3)	5243	5513
Surface gravity (m/s^2)	8.87	9.81
Escape velocity (10^3 m/s)	10.36	11.19
Visual geometric albedo	0.67	0.367
Mean solar irradiance (W/m^2)	2613.9	1367.6
Black body temperature (K)	184.2	254.3
Topographic range (km)	15	20

ATMOSPHERIC PARAMETERS	Venus	Earth
Surface pressure (bar)	92.1	1.014
Surface density (kg/m^3)	65	1.217
Scale height (km)	15.9	8.5
Total mass of the atmosphere (10^{18} kg)	480	5.1
Average surface temperature (K)	735.3	288
Mean molecular weight (g/mole)	43.45	28.97
Atmospheric composition (near surface, by volume)	Major (%): CO_2 - 96.5; N_2 - 3.5 Minor (ppmv): SO_2 - 150; Ar - 70; H_2O - 20; CO - 17; He - 12; Ne - 7	Major (%): N_2 - 78.08; O_2 - 20.95 Minor (ppmv): Ar - 9340; CO_2 - 400; Ne - 18.18; He - 5.24; CH_4 - 1.7; Kr - 1.14; H_2 - 0.55; H_2O - highly variable, typically makes up about 1%

Chapter 2

Venus Express

Venus was the first planet to be explored by a spacecraft sent from Earth and was the target of over 40 missions launched by the US and Soviet space agencies throughout more than 20 years, from the early 1960s to the late 1980s. In the 1990s the interest in Venus went down while the attention gradually moves toward Mars and, more recently, Jupiter, Saturn and some of their satellites. Just starting from a project related to the Red Planet, Mars Express, the European Space Agency (ESA) launched in 2005 a nearly twin mission to revamp the interest on Venus and called it Venus Express (VEx). The mission was controlled by the Venus Express Mission Operations Centre (VMOC) located at the European Space Operations Centre (ESOC) in Darmstadt, Germany, while science activities were performed by the Venus Express Science Operations Centre (VSOC) located at the European Space Astronomy Centre (ESAC) in Villanueva de la Cañada, near Madrid, Spain. The mission was initially thought to last only two years but it was extended several times until 16 December 2014, when the mission officially finished. The main topics of the mission were: study of the lower atmosphere, below the main cloud deck, and variations of the atmospheric minor constituents (the mains are CO, OCS, SO_2, H_2O, HF, HCl); study of the structure, composition and optical properties of the clouds and their temporal and spatial variability; study of the atmosphere dynamics, in particular the large hot dipole structure at the south pole; retrieval of vertical temperature profiles and surface thermal maps; research of events related to light-
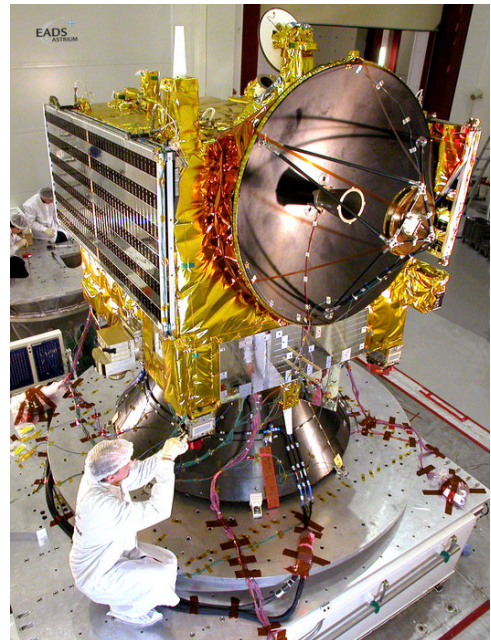
Figure 2.1: Venus Express spacecraft being prepared for tests

ning; understand the transition region between troposphere and thermosphere, in particular Non-Local Thermodynamic Equilibrium (LTE) phenomena; study of variations to be related to surface/atmosphere interactions, dynamics, meteorology or volcanism; study of the magnetosphere.

2.1   The spacecraft: VEx

Venus Express was launched from Baikonur cosmodrome in Kazakhstan on 9 November 2005. It arrived at Venus on 11 April 2006 and braked into a highly elliptical, near-polar orbit which was specifically chosen to ensure the maximum scientific return. VEx moved on a 24 hours orbit with the pericentre located between 80° N and 90° N at 250 km altitude and the apocentre located at 66000 km from the surface. Pericentre altitude was lowered to 165 km during a series of low passes in the period 2008-2013 to permit a series of high resolution observations of the planet, and on May 2014 the orbit was lowered again to a minimum distance of 130 km. The orbit was "locked" in space, with respect to the background stars, while the planet rotated beneath it. As a result, the spacecraft's instruments were able to observe almost the entire planet over a full Venusian day (243 Earth days). The spacecraft was conceived to be rotate at discretion on its axes to change pointing direction of the on board instruments. Such a possibility permitted to change, depending on needs, the kind of observation to be done, keeping a fixed pointing direction, a uniform rotation or an oscillation of the spacecraft, looking at the surface, at limb or toward the space. ESA identified seven different pointing modes:

NADIR This mode is used for looking at the planet.

INERTIAL Used to stare at a fixed direction in space. This mode is employed for stellar and solar occultations and for inertial limb crossings. In the latter, the bore-sight of the spacecraft will slowly sink through the limb. A modification to this mode, the LIMB mode, was later introduced to allow tracking of a fixed altitude in the limb.

MOSAIC This mode facilitates the creation of a large image from a series of smaller ones.

CUSTOM This is applied mostly for the radio science instrument when using atmospheric refraction of radio waves to determine atmospheric temperature at different heights.

PENDULUM This permits NADIR observations in the ascending branch of the orbit in hot seasons when the thermal constraints on the spacecraft normally would prevent any science operations. This has resulted in a factor of 2-3 increase in the number of NADIR-type observations. In this mode the spacecraft alternates

between a NADIR orientation which exposes sensitive faces of the spacecraft to full Sun, followed by a slew to a cooling attitude in which excessive heat can be radiated away. These two orientations are repeated over a period of, typically, 9 hours.

SPOT TRACK Used to continuously track a point on the surface of Venus. The latitude, longitude and height above surface of the target point are pre-programmed into the observation schedule. This was introduced to avoid the inherent drifting that occurs with observations made in NADIR mode.

PLANET TRACK This mode facilitates the continuous tracking of other celestial bodies by actively steering the spacecraft. Celestial coordinates are pre-programmed into the schedule. It is used to make long distance observations of Earth, Mercury and Mars.

The large number of pointing modes allows to obtain a huge variety of information in different conditions but, at the same time, it doesn't allow to have a continuous dataset of observations with the same pointing mode.

VEx had a similar design and payloads to its predecessor Mars Express but some payloads were slightly modified instruments that were originally designed for ESA's Rosetta comet chaser, devoted to study the comet 67P/Churyumov-Gerasimenko. Thanks to this rearrangement of existing instruments, the spacecraft was built in only 33 months. The spacecraft body itself, termed a "bus", was a honeycomb aluminium box 1.5 x 1.8 x 1.4 m wide and with the two solar arrays of 5.7 m^2 extended it measured about 8 m across. A spacecraft coating composed of 23 gold layers, called Multi-Layer Insulation (MLI), reflected radiation away and kept VEx cool. Table 2.1 summarizes some spacecraft facts. Venus Express carried seven payloads (Figure 2.2):

ASPERA-4 (Analyser of Space Plasma and Energetic Atoms)
Analysis of ionized and non-ionized plasma. Derived from ASPERA-3, Mars Express

MAG (Magnetometer)
Measurement of the magnetosphere. Derived from ROMAP, Rosetta

PFS (Planetary Fourier Spectrometer)
Vertical sounding of the atmosphere using infrared spectroscopy. Derived from PFS, Mars Express

SPICAV (Spectroscopy for Investigation of Characteristics of the Atmosphere of Venus)
Atmospheric spectroscopy in solar or stellar occultation. Derived from SPICAM, Mars Express

VERA (Venus Radio science experiment)

Radio sounding of the atmosphere. Derived from RSI, Rosetta

VIRTIS (Visible and Infrared Thermal Imaging Spectrometer)

Spectrographic mapping of the atmosphere and surface. Derived from VIRTIS, Rosetta

VMC (Venus Monitoring Camera)

Ultraviolet and visible imaging. Derived from HRSC/SRC, Mars Express, and OSIRIS, Rosetta

Only VIRTIS is target of the thesis work.

Table 2.1: Venus Express spacecraft facts

Spacecraft bus dimensions	1.5 x 1.8 x 1.4 m
Spacecraft mass	1270 kg (including 93 kg of payload and 570 kg of fuel)
Thrust of main engine	400 N
Attitude thrusters	Two sets of four, each delivering 10 N each
Solar arrays	Two triple-junction GaAs: 5.7 m^2, generating 800 W near Earth and 1100 W at Venus
Power storage	Three lithium-ion batteries
Antennas	Two high-gain dishes: HGA1 = 1.3 m in diameter, HGA2 = 0.3 m in diameter; two low-gain antennas

2.2   The instrument: VIRTIS

VIRTIS was a diffraction spectrometer operating from UV to near-IR wavelengths and it was composed of two separate optics, -M and -H. VIRTIS-M, built by Galileo Avionica in Firenze, Italy, had high resolution imaging capability at moderate spectral resolution in the range between 0.25 µm and 5 µm. It was in turn divided into two component, M-VIS from 0.25 µm to 1 µm and M-IR from 1 µm and 5 µm. VIRTIS-H, built by Laboratoire d'Études Spatiales et d'Instrumentation en Astrophysique (LESIA) in Meudon, France, had high spectral resolution in the range between 2 µm and 5 µm but no imaging capability (Piccioni et al., 2007; Erard, 2012).

Four separate modules composed the instrument: an Optics Module (OM) which housed the optical heads of the two components -M and -H and the Stirling cycle cryocoolers used to cool the IR detectors (see next); two Proximity Electronics Modules (PEM)
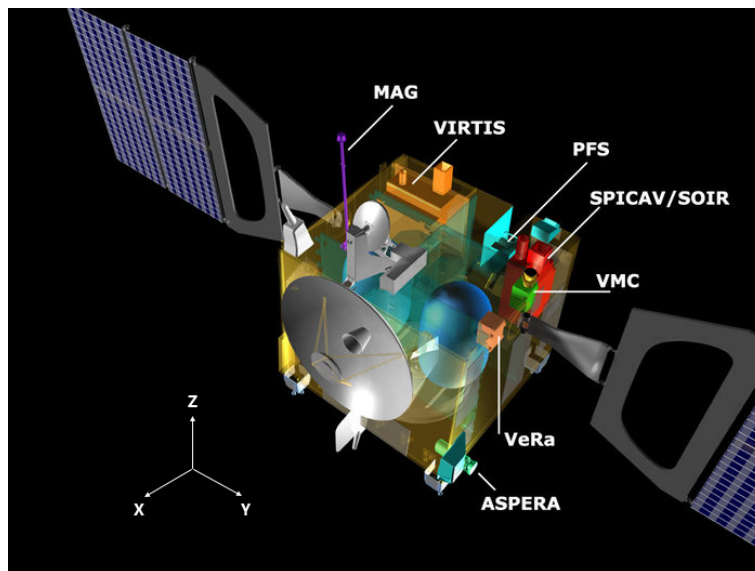
Figure 2.2: Structure and payloads of Venus Express. Spacecraft axes are also indicated.

required to drive the two optical heads, one for each component -M and -H; the Main Electronics Module (ME) which contained the Data Handling and Support Unit (DHSU) and the power supply. The OM (Figure 2.3) was lodged in the external -X panel of the spacecraft (Figure 2.2) with the two optical heads co-aligned, pointing to +Z direction. Both optical systems had slits parallel to the Y axis and VIRTIS-M was also able to scan the scene with a scanning mirror which rotated on the Y axis. The OM was physically divided into two sections, one with the optical heads and one with the cryocoolers, thermally insulated from each other by mean of multi-layer insulation. The heat produced by the cryocoolers was dissipated to the spacecraft, which maintained a temperature of 250-300 K, whereas the optical heads maintained a temperature of 130 K by means of a passive radiator that dissipated to the space. The two Stirling cycle cryocoolers were used to cool the IR detectors to 70 K, to reduce the thermal noise due to dark currents. The two PEM contained the electronics to drive the optical heads, the covers and the thermal control and run the acquisition of the spectra. The ME controlled electronics of the cryocoolers and the power supply for the overall instrument, managed the electric component, interfaced with the OM, the spacecraft and the DHSU for the data storage and processing.

2.2.1   VIRTIS-M

VIRTIS-M was composed of a Shafer telescope provided with five aluminium mirrors, the first of them moving and scanning, and an Offner grating spectrometer provided with glass mirrors to separate the spectral components. A single grating substrate, of two
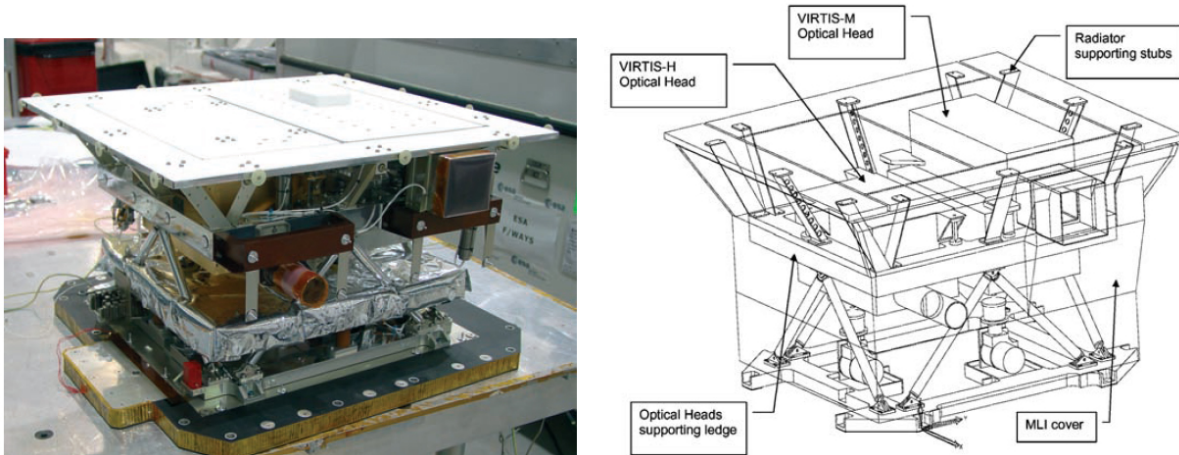
Figure 2.3: VIRTIS optics module

concentric separate regions having different groove densities in the inner and outer part (about 30% and 70% of the grating respectively), permitted to spread the spectrum on the two detectors M-VIS and M-IR depending on wavelength. The shortest wavelengths were collected on a silicon (Si) Charge Coupled Device (CCD) with 512 x 1024 sensitive elements: the first value represents the "spatial resolution" and the second one the "spectral resolution". The longest wavelengths were collected on a mercury cadmium telluride (HgCdTe) InfraRed Focal Plane Array (IRFPA) with 270 x 438 sensitive elements of physical size double than the CCD elements. From both the devices, after some processing to make their spatial resolution uniform and simplify data transmission, 256 spatial and 432 spectral values were selected for each exposure (Figure 2.4). Technical facts of the detector are given in Table 2.2.

2.2.2   VIRTIS-H

VIRTIS-H was composed of an echelle spectrometer provided with two parabolic mirrors that steered radiance from the slit to a lithium fluoride (LiF) dispersion prism, then to a diffraction grid and finally to an IRFPA identical to that of M-IR. Combining the prism with the grid permitted to spread each exposure into 8 spectral orders (limited wavelength bands, achieved by the prism) with 438 spectral point each (sampled by the grid). Therefore, the spectral resolution was improved of a factor 8 compared to VIRTIS-M. However, higher spectral resolution was achieved to the detriment of spatial information which was largely reduced. The eight spectral orders were spread over the detector area so that the spatial resolution was performed only on 5 sensitive elements for each order, to be compared with the 256 elements of VIRTIS-M. Figure 2.5 better illustrates the situation: on the detector area, the 8 spectral orders are spread over all the 438 spectral elements but only over 5 spatial elements each, representing the slit
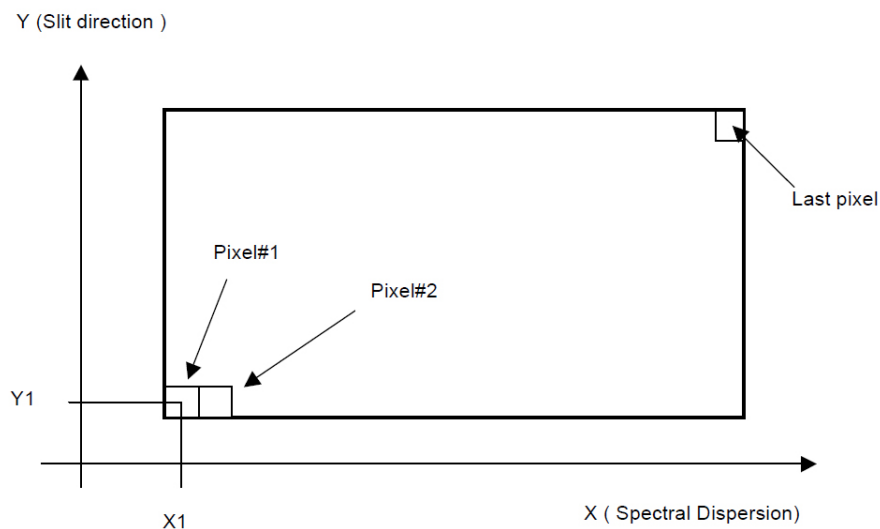
Figure 2.4: Data organization on the CCD and IRFPA detectors of VIRTIS-M. The final dimensions in nominal mode are in both cases 432 x 256

Table 2.2: VIRTIS facts

	VIRTIS-M VIS	VIRTIS-M IR	VIRTIS-H
Spectral range (µm) [1]	0.2882 - 1.1093	1.0305 - 5.1226	*Or0* 4.01206 - 4.98496
			Or1 3.44270 - 4.28568
			Or2 3.01190 - 3.75586
			Or3 2.67698 - 3.33965
			Or4 2.40859 - 3.00570
			Or5 2.18903 - 2.73220
			Or6 2.00565 - 2.50468
			Or7 1.85100 - 2.31194
Spectral resolution $\lambda/\Delta\lambda$	100 - 300	70 - 360	1300 - 3000
Spectral sampling (nm)	1.89	9.44	0.6
Field of View (FOV) (mrad x mrad)	63.6 (slit) x 64.2 (scan) [2]		0.567 x 1.73
Max spatial resolution (µrad x µrad)	248.6 (slit) x 250.8 (scan) [2]		
Telescope	Shafer	Shafer	Parabolic mirror
Slit dimension (mm)	0.038 x 9.53		0.029 x 0.089
Spectrometer	Offner	Offner	Echelle
Detector [3]	Thomson TH7896	CdHgTe	CdHgTe
Sensitivity area format	512 x 1024	270 x 438	270 x 438
Pixel pitch (µm)	19	38	19
Operating temperature (K)	150 - 190	65 - 90	65 - 90
Signal to Noise Ratio (SNR)	> 100	> 100	> 100 @ 3.3 µm
Noise Equivalent Spectral Radiance (NESR) (central band, W / m^2 sr µm)	1.4 10^{-2}	1.2 10^{-4}	1.2 10^{-4}

[1] Spectral range measured on sample files. May depend on temperature, specially for M.

[2] Slit direction: along the slit. Scan direction: across the slit.

[3] VIRTIS-M IR and VIRTIS-H make use of identical IR detectors.
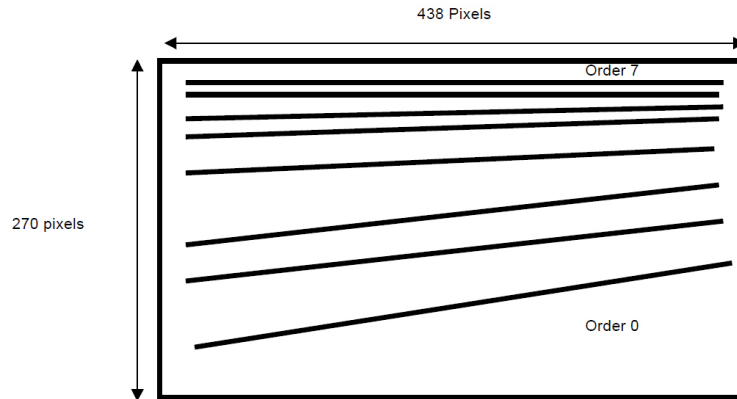
Figure 2.5: Spectrum projection over the H-channel IRFPA. Wavelengths increase from right to left and top to bottom.

projection on the IRFPA. In fact, only 15% of the detector receives useful information. The five spatial elements were then averaged during successive processing to obtain only the spectral datum. Spatial information was completely removed and so VIRTIS-H wasn't able to perform imaging. Technical facts of the detector are given in Table 2.2.

2.3   Data format and content

VIRTIS raw data had been pre-processed several time before they became available as end user data in Planetary Data System (PDS) format on ESA's server:

<div align="center">

`ftp://psa.esac.esa.int/pub/mirror/VENUS-EXPRESS/VIRTIS/`

</div>

The official software to read such data is called LecturePDS (Erard, 2010), is written in Interactive Data Language (IDL) and is also available on ESA's server. Raw data were calibrated at Istituto di Astrofisica e Planetologia Spaziali (IAPS) in Roma, Italy, and at LESIA in Meudon, France. Observations are classified in 24 hours sessions corresponding to a single orbit, with a progressive associated number, and in four weeks period called Medium Term Plan (MTP). Each session could be split in sub-sessions if significant conditions of observation changed during the orbit, such as pointing mode, scanning mode or exposure time. In this way, observations into each sub-session have homogeneous characteristics. For each session/sub-session three kinds of data are available with their own file extension: raw data in numeric format (.QUB), calibrated data expressed in physical units (.CAL, radiances in $W/m^2 \, \mu m \, sr$) and geometry data (.GEO) which gives information on the spatial and temporal positioning of each observation (Erard, 2012; Politi et al., 2014). Depending on the observation channel, three kinds of calibrated data can be available for each session/sub-session with different prefix: VH for VIRTIS-H

data, VV for VIRTIS-M VIS and VI for VIRTIS-M IR. Only the last kind of data in the infrared is considered in the thesis work.

2.3.1 Calibrated data

Each .CAL file contains a structure called QUBE, that is essentially a three dimensional matrix of radiances (a cube). The first dimension, called BAND, represents the spectral dimension defined by the wavelength. The second dimension, called SAMPLE, represents the spatial direction along the slit. These two dimensions relate to a single exposure of the detector. The third dimension, called LINE, represents acquisitions in successive time steps. Successive observations could be done passively taking advantage of satellite motion or actively with the scanning mirror of the instrument. Each element of the cube is called PIXEL and records the radiance observed at such a wavelength, point and time. Some pixel with problems, such as saturated or damaged pixels, are indicated with values lesser than -999 and coded on the type of problem so that it is possible to easily remove useless data.

Besides this basic structure that collects radiance data, other useful information are recorded in the same file. Distinct structures give wavelengths, instrument Full Width at Half Maximum (FWHM), session name, units of measurement, cube dimensions and some temporal information (Cardesin, 2008; Reess and Henry, 2008). Each file is also equipped with a structure called LABEL that gives information on the instrument and the characteristics considered homogeneous during the session (exposure time, mirror motion, spacecraft orientation and so on). One of the main parameters stored in the label is the exposure time, that can change from 0.02 s to 18 s. The majority of nocturnal observations has an exposure time of 3.3 s for long-lasting observations or 0.36 s for brief observations. The advantage in long-lasting records is the high SNR, the disadvantage is the lost of information above 4 µm about since the detector is saturated from internal currents and thermal background (Piccioni et al., 2007). Such a limit is observed in many analysed cubes in the thesis work.

2.3.2 Geometry data

As for the calibrated file, the geometry file contains a cube structure with a spatial dimension (SAMPLE) and a time frame dimension (LINE) to identify each observation, but the spectral information is not necessary. The first cube dimension is replaced, for VIRTIS-M, with 33 spatial and temporal information that are necessary, for example, to locate the pixel footprint on the planet surface, know the viewing angle or know the sun position related to the spacecraft. Available parameters are given in Table 2.3 with a brief description. Parameters related to the surface of the planet are defined with respect to a reference ellipsoid with radius of 6051.8 km, whereas the clouds top is defined as a layer 60 km above the reference ellipsoid (Figure 2.6). Coordinates in the geometry file

refer to the geometric projection of the instantaneous Field of View (iFOV) on this two reference surfaces, without any correction for scattering, refraction or topography.

The geometry file, as the calibrated file, includes other useful information such as the label, session name, cube dimensions, parameters name and a series of multiplicative coefficients necessary to dimensionalize data, not saved in standard physical units (Erard and Garceran, 2008).
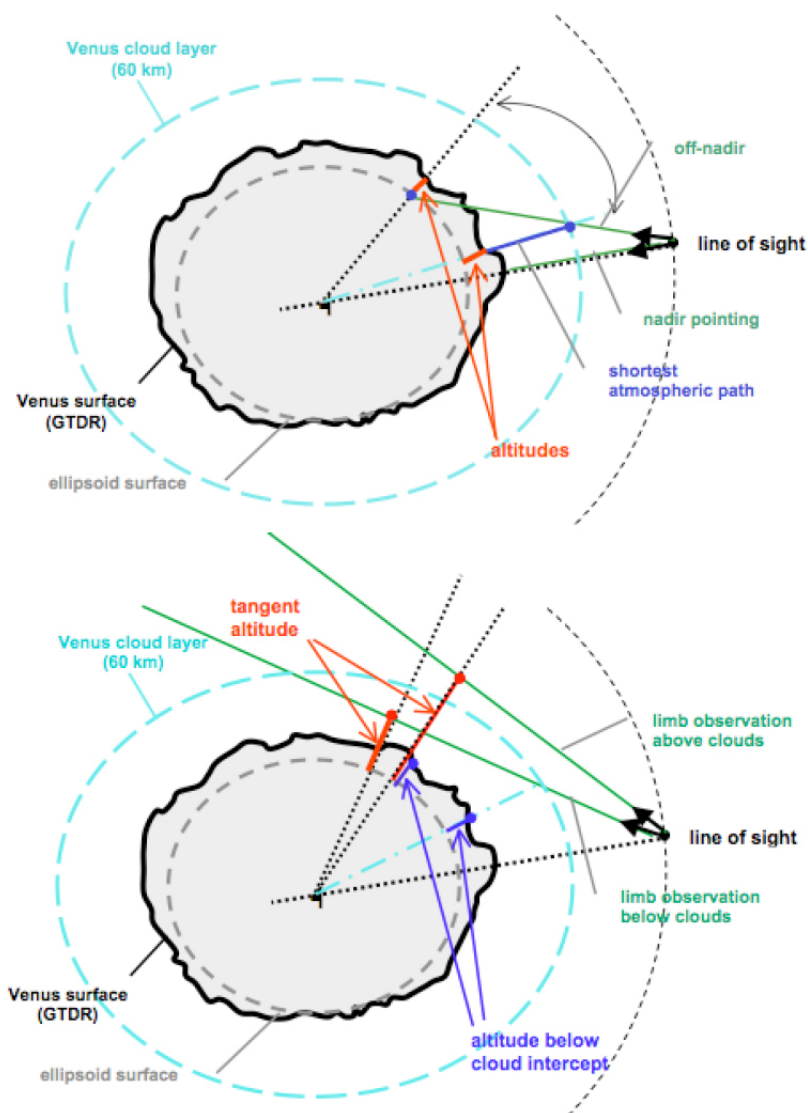
Figure 2.6: Scheme of observations intercepting the surface (top) and limb observation (bottom).

Table 2.3: Geometric parameters associated to a cube.

LINE	Parameter [1]	Comment
1-4	Longitudes of 4 pixel footprint corner points	Geometrical projection on surface ellipsoid, with no correction for scattering or refraction
5-8	Latitudes of 4 pixel footprint corner points	
9-10	Longitude and latitude of pixel footprint centre on surface ellipsoid	
11-13	Incidence, emergence and phase at footprint centre, relative to Venus centre direction	Angles relative to the reference surface (not accounting for topography). Incidence angle is equal to solar zenith angle
14	Surface elevation (footprint corners average)	From topographic model. For limb observations it is the tangent altitude +100 km
15	Slant distance (line of sight from spacecraft to surface ellipsoid at pixel centre)	Does not include topographic model
16	Local time at footprint centre	Expressed in 24-th of the rotation period
17-20	Longitudes of 4 corner points on cloud layer	Geometrical projection on reference cloud layer (60 km)
21-24	Latitudes of 4 corner points on cloud layer	
25-26	Longitude and latitude of pixel centre on cloud layer	
27-29	Incidence, emergence and phase, relative to local normal of cloud layer	
30	Surface elevation at the vertical of cloud layer intercept	From topographic model. For limb observations above the cloud layer it is the surface elevation at the vertical of the tangent point
31-32	Right ascension and declination of pointing direction	J2000 reference frame
33	One frame-common plane	Provides 10 scalar quantities along the frame spatial dimension (SAMPLE). The remainder is set to 0
	1-2 SpaceCraft Elapsed Time (SCET) (on-board time measured in s from launch)	The first value stores the SCET first two words (integer part), the second one stores the third SCET word (fractional part)
	3-4 Universal Time Coordinated (UTC)	The first value contains the number of days since Jan. 1st, 2000, the second value contains the time of the day as 10000 x seconds (starting from 0h)
	5-6 Sub-spacecraft coordinates (longitude/latitude)	
	7-8 Sine and cosine of M mirror angle	
	9 angle between Sun direction and VIRTIS Z axis	
	10 azimuth of Sun direction in instrument XY plane (counted from 0° at X axis)	

[1] Whenever the line-of-sight does not intercept the surface, angles, local time and slant distance are computed at the intersection with the local vertical (tangent point).

Chapter 3

The atmosphere of Venus: gases

To simulate the outgoing radiance observed by VIRTIS it is necessary to adequately model all the atmospheric components of the planet, first of all the gases and their optical properties. To compute gases absorption the software package ARS was used (section 3.3), whereas the scattering properties were computed with a MATLAB code (section 3.6).

3.1 Atmospheric profiles: pressure, temperature and gases concentration

Temperature and pressure profiles of Venus' atmosphere were defined as standard profiles in the eighties, then revised over the years, and they are known as Venus International Reference Atmosphere (VIRA). These profiles describe with 1-2 km of vertical resolution the atmosphere of Venus from the ground up to 100 km altitude (Kliore et al., 1985; Seiff et al., 1985; Moroz and Zasova, 1997; Zasova, 2012). They were acquired through observations from Earth, satellite data of many Soviet and US missions sent over the years (Venera, Vega, Pioneer) and in-situ measurements obtained by probes drop to the surface (although none of the landing craft survived for more than a couple of hours after touchdown). VIRA profiles below 30 km are uniform all over the planet thanks to the high atmospheric density, high thermal inertia and strong convection within the lower layers. Above 30 km the profiles show meridional variability and are defined per latitude bands, with little differences in pressure (Figure 3.1) but more evident in temperature (Figure 3.2). The weighting function of the gases reaches the maximum value always below 100 km, with the exception of few narrow spectral bands that are particularly opaque (see details at section 3.5). As a consequence, it is correct to consider the TOA of the model at 100 km altitude, because the observed radiance come almost entirely from that layers.

With regard to the gases concentration profiles, it was considered a constant value
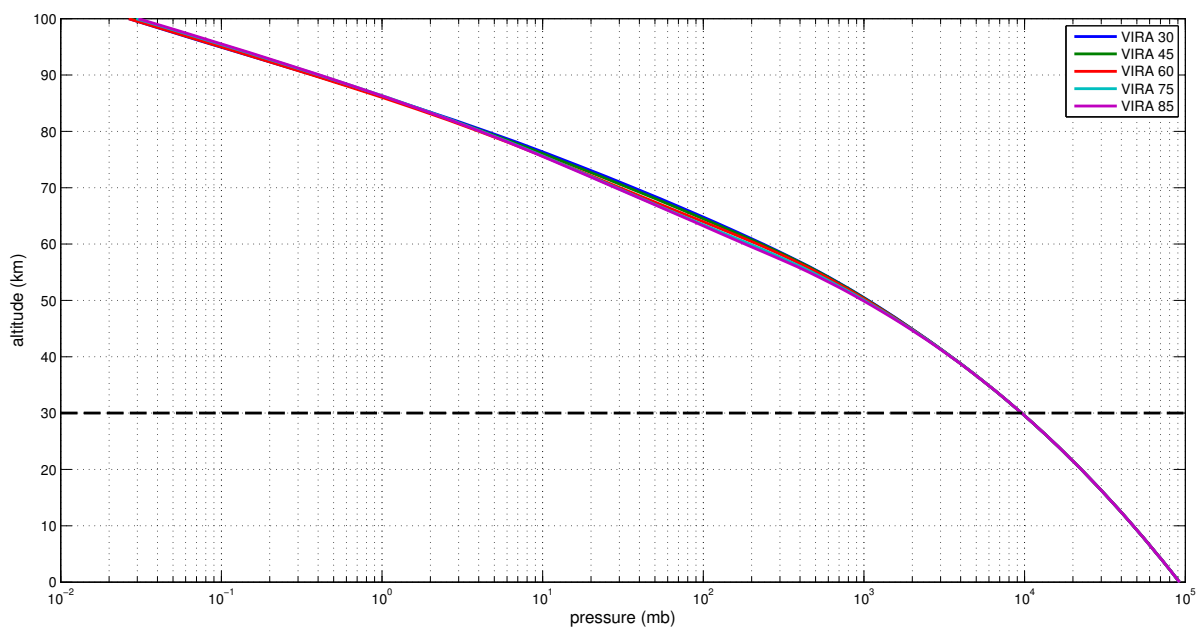
Figure 3.1: Mean vertical profiles of pressure for latitude band (VIRA). Mean latitude is given in legend. Below 30 km all the profiles are equivalent.
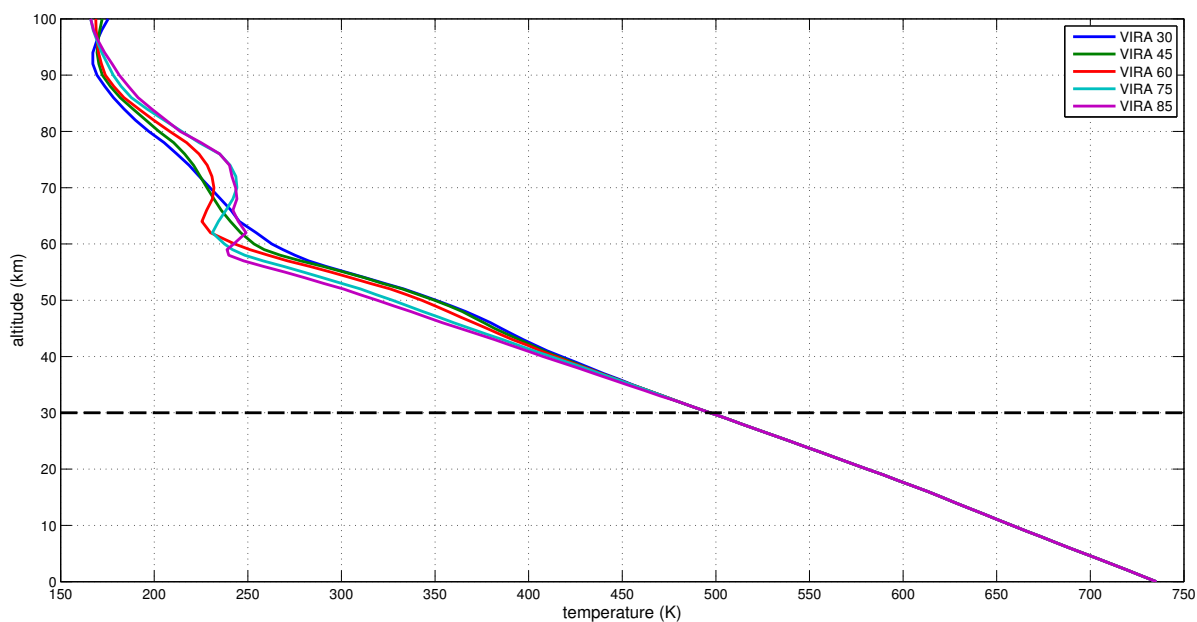
Figure 3.2: Mean vertical profiles of temperature for latitude band (VIRA). Mean latitude is given in legend. Below 30 km all the profiles are equivalent.
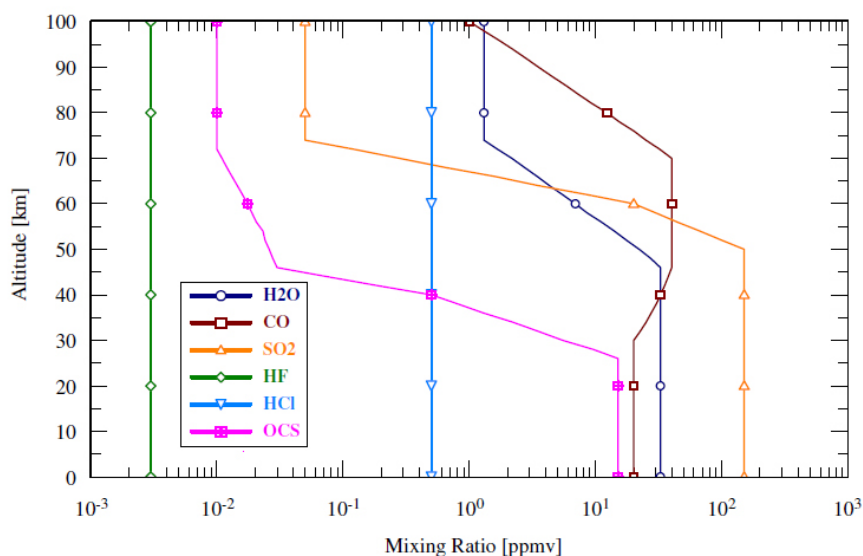
Figure 3.3: VMR profiles for the principal minor constituents in Venus' atmosphere.

for CO_2, that is the main atmospheric constituent: about 96.5% by volume. For the principal minor constituents which are optically active in the VIRTIS 1-5 µm band it was referred to Haus and Arnold (2010), who suggest the vertical profiles of Volume Mixing Ratio (VMR) shown in Figure 3.3 for H_2O, CO, SO_2, OCS, HCl and HF, from the ground up to 100 km. About 3.5% by volume of Venus' atmosphere is composed of N_2, that has no absorption in the analysed spectral band and so it was only considered for molecular scattering. In addition to these gases, Venus' atmosphere has many other compounds (Esposito et al., 1997; de Bergh et al., 2006; Mills et al., 2007; Kransopolsky, 2012) but their VMR is rather low and their interaction with radiation, between 1 and 5 µm, is sufficiently weak to make them negligible for radiative transfer computation.

3.2 Molecular spectroscopic databases

Spectral properties of gases are available in specific databases. The main and most used, but not the only one, is HITRAN (Rothman et al., 2013). This database, continuously updated, is a compilation of spectroscopic parameters necessary to simulate transmission and emission of radiation inside the atmosphere. It contains properties of 47 gaseous species and many isotope (ver. 2012). The spectroscopic parameters are obtained with experiments or quantum theory on a wide range of wavelengths (Rothman et al., 2013). The 19 available parameters are given in Table 3.1.

Despite it is undoubtedly the main available database to describe Earth's atmosphere, HITRAN has some limits for usage in Venus' atmosphere. The high temperatures and
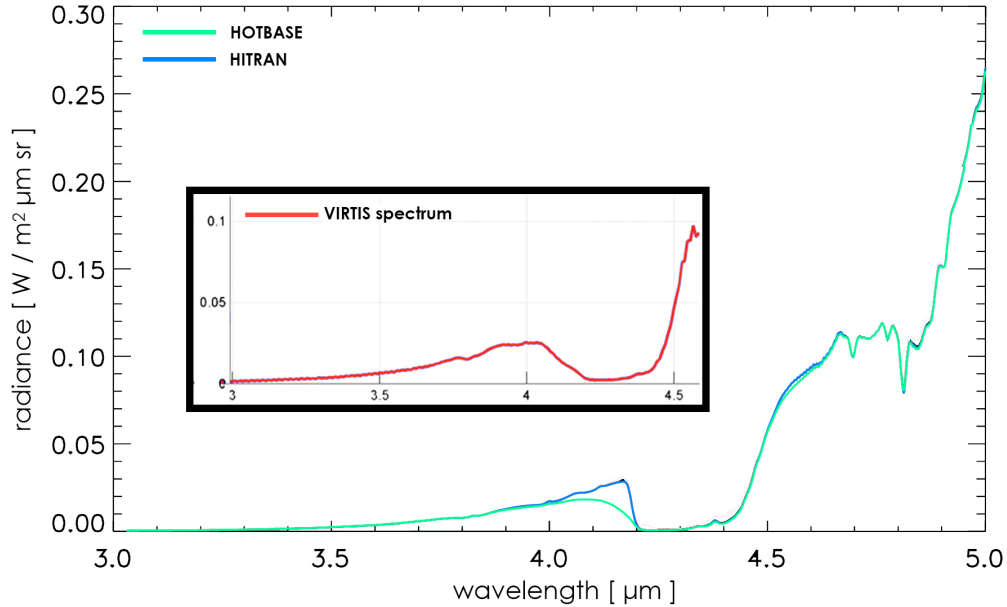
Figure 3.4: Qualitative comparison between radiances simulated with HITRAN or HOTBASE and a typical VIRTIS observation (inset) for the ν_3 band of CO_2. HOTBASE, which accounts for many more weak lines than HITRAN, simulates in more realistic way the observed trend.

pressures give importance to transitions that are too weak in Earth's typical conditions and so they are not adequately represented in HITRAN. Some transitions might have a different behaviour in those extreme condition and need adequate parametrizations. Therefore, specifically created databases are necessary to go beyond these limits. The two databases used for this purpose are HITEMP (Rothman et al., 2010) and HOTBASE (Pollack et al., 1993). They preserve the same basic structure of HITRAN but are specific for high temperatures and pressures. HITEMP has been specifically developed to pass the limits of HITRAN in astrophysics and it supplies valid parameters at temperatures higher than 400 K for five gaseous species: H_2O, CO_2, CO, NO and OH. HOTBASE is a specific database for CO_2, it has been developed with quantum theory specifically for Venus' atmosphere and so it is the most valuable to describe that gas. The difference between HITRAN and HOTBASE in describing CO_2 is evident at 4.3 μm, corresponding to the ν_3 band. A qualitative comparison between a typical VIRTIS observation and two simulations with both the databases shows that HOTBASE makes a more realistic representation between 4 and 4.2 μm, due to the accuracy in describing the many weak spectral lines (Figure 3.4).

Taking advantage of the three database strengths, it was used HOTBASE for CO_2, HITEMP ver. 2012 for H_2O and CO, HITRAN ver. 2012 for SO_2, OCS, HCl and HF.

Table 3.1: Description of the parameters available in the three spectral databases.

Symbol	Parameter	Comments or units
M	Molecule number	HITRAN chronological assignment
I	Isotope number	Ordering by terrestrial abundance
ν_0	Vacuum wavenumber	cm^{-1}
S	Intensity	cm^{-1}/(molecule cm^{-2}) at 296 K
A	Einstein A-coefficient	s^{-1}
γ_{air}	Air-broadened halfwidth	HWHM (cm^{-1} atm^{-1}) at 296 K
γ_{self}	Self-broadened halfwidth	HWHM (cm^{-1} atm^{-1}) at 296 K
E"	Lower-state energy	cm^{-1}
n	Temperature-dependence coefficient	Temperature-dependent exponent for γ_{air}
δ	Air pressure-induced line shift	cm^{-1} atm^{-1} at 296 K
V'	Upper-state "global" quanta	Rothman et al. (2005)
V"	Lower-state "global" quanta	Rothman et al. (2005)
Q'	Upper-state "local" quanta	Rothman et al. (2005)
Q"	Lower-state "global" quanta	Rothman et al. (2005)
I$_{err}$	Uncertainty indices	Uncertainty indices for 6 critical parameters (ν,S,γ_{air},γ_{self},n,δ)
I$_{ref}$	Reference indices	Reference pointer for 6 critical parameters (ν,S,γ_{air},γ_{self},n,δ)
*	Flag	Pointer to program and data for the case of line mixing
g'	Statistical weight of the upper state	Simečková et al. (2006)
g"	Statistical weight of the lower state	Simečková et al. (2006)

3.3 Gases absorption: the ARS package

Atmosphere Radiation Spectrum (ARS) (Ignatiev et al., 2005) is a set of programs implementing line-by-line calculations of gaseous and aerosol opacity, transmittance, atmospheric radiance spectra and other related things. In the thesis, ARS was used to compute the absorption coefficients of the gases which have an active role in Venus' atmosphere in the 1-5 µm band. ARS is structured as a chain of programs giving elements for the final computation. A block diagram is shown in Figure 3.5.

3.3.1 arshls

Arshls is the first link in the chain and it's used to reduce the size of the spectral database. This is performed by limiting the database to the wavenumbers of interest, removing some unnecessary parameters and, if required, removing the weakest spectral lines below a critical intensity threshold, defined in an input file. The requested parametrizations are supplied to the program with a simple text file and the output is a *.l file for each gas, equal to the original database but reduced to the essential components.

To considerably reduce the computation time, referring to Haus and Arnold (2010), the spectral lines weaker than 10^{-28} cm^{-1}/(molecules cm^{-2}) were removed for each gas except CO_2, which was limited to 10^{-35} cm^{-1}/(molecules cm^{-2}). The discarded lines are sufficiently weak to be negligible in the final result but some times are numerous and the computation time for later steps would be too long.
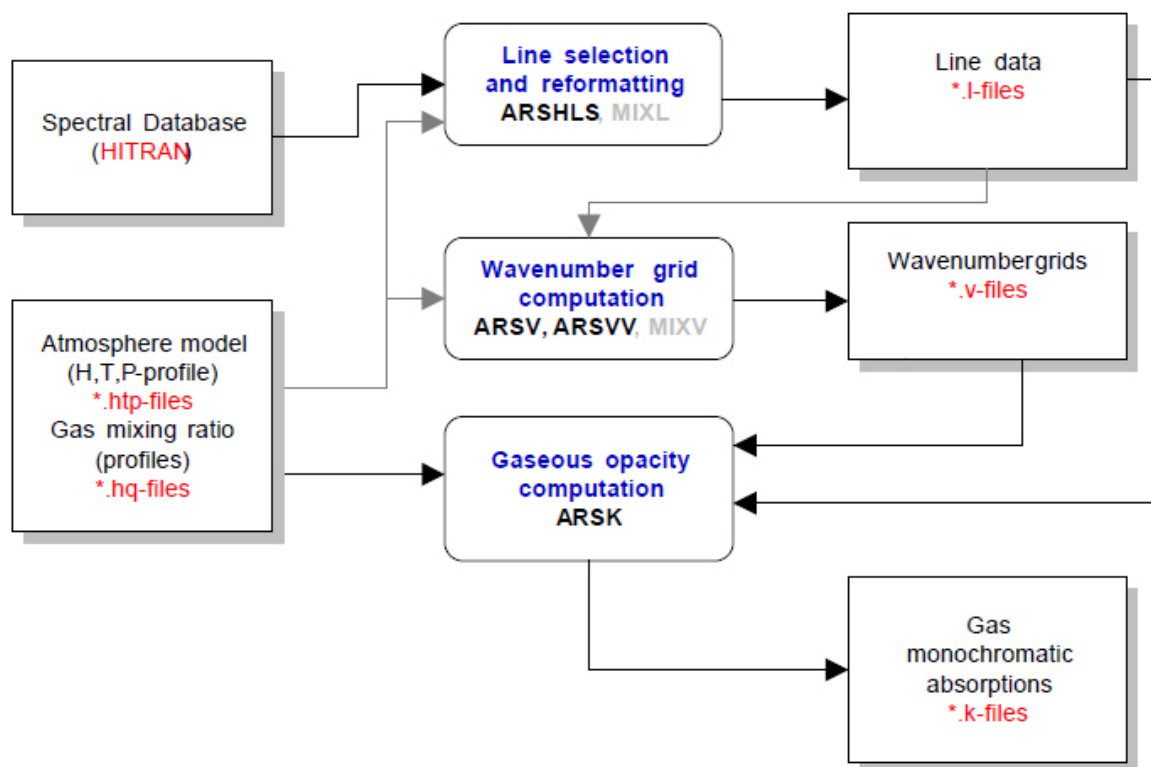
Figure 3.5: Block diagram of the ARS package for computation of gases absorption. Input and output files are given in red.

3.3.2 arsvv

Arsvv produces a *.v file in which it defines the requested wavenumbers for later monochromatic computations and determines the output grid of the final result. The grid can be regular or irregular depending on needs. For this work, a regular grid was chosen with a 0.02 cm^{-1} step between 2000 cm^{-1} and 10000 cm^{-1}, so that the whole VIRTIS-M IR range was represented with high resolution.

3.3.3 arsk

Arsk is the last link in the chain and it's the program that actually computes the absorption coefficients with a line-by-line code. The external input necessary to the program are: a *.htp file defining height (h), temperature (t) and pressure (p) of the atmospheric profile (VIRA profiles); the *.v file produced by arsvv containing the spectral range of interest and the output grid; the *.l files produced by arshls containing the gases spectral properties. In addition to these input files, a series of parametrizations of the spectral

Table 3.2: Parametrizations of the χ factor depending on distance from the line centre ν_0.

Tonkov et al. (1996)		Bézard et al. (2009)	
$\|\Delta\nu\| = \|\nu - \nu_0\|$ (cm^{-1})	χ	$\|\Delta\nu\| = \|\nu - \nu_0\|$ (cm^{-1})	χ
$\|\Delta\nu\| < 3$	1	$\|\Delta\nu\| < 3$	1
$3 < \|\Delta\nu\| < 150$	$1.084^{(-0.027\|\Delta\nu\|)}$	$3 < \|\Delta\nu\| < 60$	$1.051^{(-\|\Delta\nu\|/60)}$
$150 < \|\Delta\nu\| < 300$	$0.208^{(-0.016\|\Delta\nu\|)}$	$60 < \|\Delta\nu\|$	$0.6671^{(-\|\Delta\nu\|/110)}$
$300 < \|\Delta\nu\|$	$0.025^{(-0.009\|\Delta\nu\|)}$		

lines are given to the program to define line profile, cut-off and form factor χ.

The line profile can be chosen between Gaussian, Lorentzian or different approximations of Voigt profiles. The Voigt profile defined by Kuntz (1997) was selected for this work.

The cut-off is the distance, expressed in cm^{-1} from the line centre, where the line wings are cut to remove its less significant part and speed up the computation. To define this parameter it was referred to Haus et al. (2013), setting a cut-off equal to 125 cm^{-1} for each gas except CO_2. CO_2 was limited with a differential cut-off depending on wavenumber: 125 cm^{-1} from 2000 cm^{-1} to 7500 cm^{-1} and 250 cm^{-1} from 7500 cm^{-1} to 10000 cm^{-1}.

The form factor χ is a multiplicative parameter, in the range 0-1, that reduces the line intensity of the far wings. In fact, the line profile is not a perfect Voigt, especially at high pressure, essentially due to collision-induced intensity transfer between transitions (line-mixing effects) and to the finite duration of intermolecular collisions. Considering a Voigt profile overestimates the absorption of the far wings and so a correction is necessary (Tran et al., 2011). Line-mixing effects have been studied in particular for CO_2 and can be described with complicated quantum models or in a simplified way by introducing the form factor χ. Many parametrizations are suggested by different authors (Winters et al., 1964; Tonkov et al., 1996; Bézard et al., 2009; Tran et al., 2011). Referring again to Haus et al. (2013), it was established a χ equal to 1 for each gas except CO_2. It was implemented in ARS the form factor for CO_2 suggested by Tonkov et al. (1996) from 2000 cm^{-1} to 7500 cm^{-1} and that by Bézard et al. (2009) from 7500 cm^{-1} to 10000 cm^{-1}. The two parametrizations are given in Table 3.2 and shown in Figure 3.6. Table 3.3 summarizes all the parameters used in the absorption coefficients computation.

Having defined the spectral parameters, the atmospheric parameters and the other parametrizations just described, arsk computes, for each gas, the monochromatic absorption cross section of the Voigt profile, in cm^2, for each i-th transition:

$$\sigma_i(\nu, p, T) = \frac{Sa}{\pi^{3/2}\beta} \int_{-\infty}^{+\infty} \frac{e^{-t^2}\mathrm{d}t}{a^2 + (x-t)^2} \ , \qquad a = \frac{\alpha}{\beta} \ , \quad x = \frac{\nu - \nu_0}{\beta} \qquad (3.1)$$
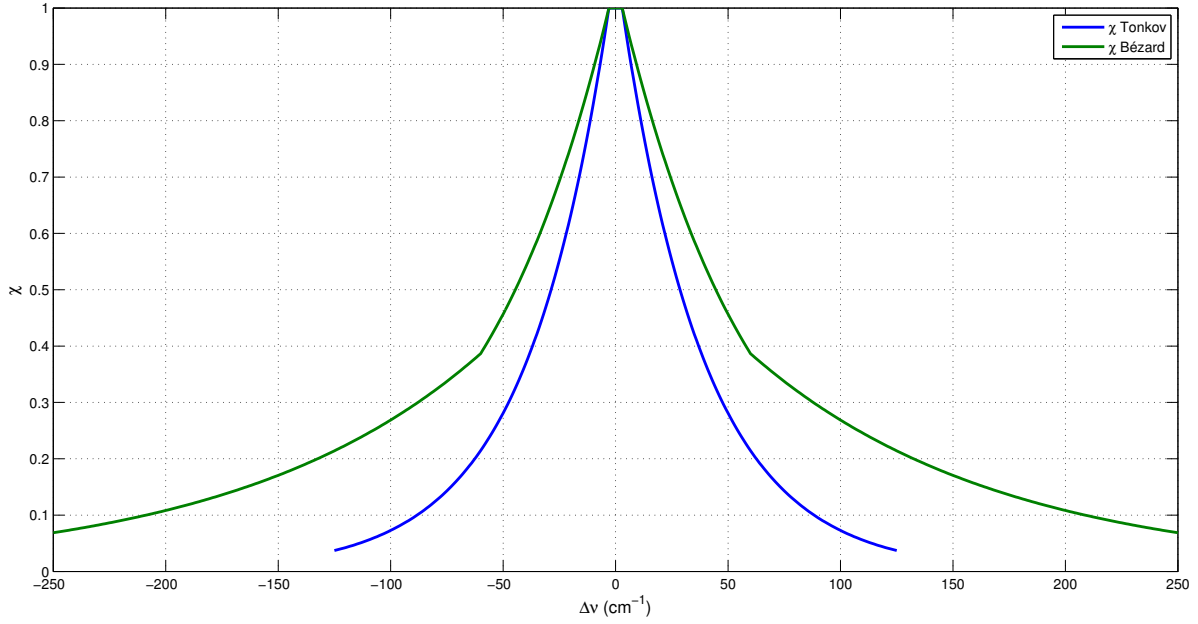
Figure 3.6: Form factor χ defined by Tonkov et al. (1996) and Bézard et al. (2009) depending on distance from the line centre. To the curves, it was applied the cut-off set in the model for the respective spectral band (125 cm^{-1} to Tonkov (2000-7500 cm^{-1}), 250 cm^{-1} to Bézard (7500-10000 cm^{-1})).

where S is the line intensity, ν_0 is the line centre, α is the Lorentzian Half Width at Half Maximum (HWHM) and β is the Doppler HWHM, defined as:

$$\alpha(p,T) = \gamma_{\text{self}}(p_0, T_0)\frac{p}{p_0}\left(\frac{T_0}{T}\right)^n \ , \quad \beta(T) = \frac{\nu_0}{c}\sqrt{\frac{2RT}{M}} \tag{3.2}$$

where γ_{self} is the self-broadened HWHM, p$_0$=1 atm and T$_0$=296 K (reference parameters of the database), n is the temperature-dependence coefficient, R is the gas constant and M is the molecular weight (g/mole) of the considered gas. The line intensity S at temperature T is defined as:

Table 3.3: Overview of the parametrizations used to compute gases absorption properties.

Gas	Spectral band cm^{-1}	Database	Intensity threshold cm^{-1}/(molecule cm^{-2})	Cut-off cm^{-1}	χ
CO$_2$	2000-7500	HOTBASE	10^{-35}	125	Tonkov et al. (1996)
	7500-10000	HOTBASE	10^{-35}	250	Bézard et al. (2009)
H$_2$O, CO	2000-10000	HITEMP-12	10^{-28}	125	1
SO$_2$, OCS, HCl, HF	2000-10000	HITRAN-12	10^{-28}	125	1

$$S(T) = S(T_0) \frac{Q(T_0)}{Q(T)} e^{-c_2 E'' \left(\frac{1}{T} - \frac{1}{T_0} \right)} \frac{1 - e^{-c_2 \nu_0 / T}}{1 - e^{-c_2 \nu_0 / T_0}} \ , \qquad c_2 = \frac{hc}{k_b} \tag{3.3}$$

where E" is the lower state energy and Q is the Total Internal Partition Sum (TIPS), obtained as the sum over all the molecular energy levels:

$$Q(T) = \sum_j e^{-c_2 E_j'' / T} \tag{3.4}$$

The total absorption cross section for that gas is the sum of the contributions of all the transitions:

$$\sigma(\nu, p, T) = \sum_i \sigma_i(\nu, p, T) \tag{3.5}$$

Finally, the absorption coefficient k for a VMR equal to 100% is obtained:

$$k(\nu, p, T) = n \, \sigma(\nu, p, T) \ , \qquad n = \frac{p}{k_b T} \tag{3.6}$$

The result of the arsk computations is a *.k file containing the absorption coefficients of a pure gas, depending on wavelength and altitude (that is temperature and pressure), expressed in km^{-1}.

3.4 Continuum of CO$_2$

Despite all the corrections previously described are ameliorative in terms of radiative transfer calculation, the comparison with experimental data keeps substantial differences. This is true for the typical Earth's conditions and even more in the extreme conditions of temperature and pressure of Venus. Because of the incomplete knowledge of CO$_2$ properties, it is usual to define an additional absorption term called "continuum" (Haus and Arnold, 2010; Tran et al., 2011; Haus et al., 2013). At present, usage of continuum is not completely justifiable but it is in practice essential to obtain realistic simulations. Part of the continuum is justifiable because the previous procedure removed, to save computation time, the far wings of the spectral lines. The wings contribution of one line alone is actually negligible but in some bands, where there are many lines and they are close together, the simplification can be excessive as a whole and an additional correction is necessary. Moreover, the line profile far from the centre is never known with accuracy. However, the continuum is totally empirical and it is defined "ad hoc" to correct the simulations once all the other information are considered. As a result, the continuum is always related to the other corrections. Obviously, the same reasoning has to be done

Table 3.4: CO_2 continuum parametrization depending on spectral band.

Band centre (cm^{-1})	9804	9091	8475	7813	7634	5747	4348	2326
Band centre (µm)	1.02	1.10	1.18	1.28	1.31	1.74	2.30	4.30
Continuum (cm^{-1} amagat^{-2} x 10^{-9})	0.025	0.45	0.15	0.76	-0.59	4.1	43	0

1 amagat = 2.686777 x 10^{19} molecules cm^{-3} at T=0 ˚C and p=1 atm

for each gas and not only for CO_2 but, due to the relative abundance of gases on Venus, about all the available literature concerns CO_2.

To preserve homogeneity of parametrizations, it was considered the continuum defined by Haus et al. (2013) depending on spectral interval, given in Table 3.4. The high value at 2.3 µm denotes poor knowledge of CO_2 behaviour in that band. The null continuum at 4.3 µm is due to the fact that the observed signal in that band comes from high atmospheric layers (Figure 3.8), where low pressure and temperature make the continuum negligible, even though not completely absent. A short IDL code was used to compute the continuum for each atmospheric layer, obtaining an absorption coefficient to be added to the coefficients computed with arsk.

3.5 Optical depth and weighting function

The overall contribution of each gas can be evaluated through its optical depth X, integrated from TOA to the ground (Figure 3.7):

$$X(\lambda) = - \int_{TOA}^{0} k(\lambda, z') \, VMR(z') \mathrm{d}z' \tag{3.7}$$

where k is the absorption coefficient computed by arsk for a specific profile of temperature and pressure, with the addition of continuum for CO_2, corrected for the observed VMR profile (arsk computes k with VMR=100%). It is evident in Figure 3.7 that CO_2 prevails in almost the whole spectrum, with the exception of some small bands in which minor constituents arise: H_2O at 1.13 µm, 1.38 µm and 1.85 µm, CO at 2.35 µm, OCS at 2.44 µm and 3.44 µm, HCl from 3.25 µm to 3.75 µm, SO_2 at 3.95 µm. Total atmospheric optical depth is the sum of the single gas contributions. The total weighting function of the atmosphere can be calculated as:

$$W_{tot}(\lambda, z) = \frac{\partial \tau_{tot}(\lambda, z, TOA)}{\partial z} \tag{3.8}$$

where the atmospheric transmittance from TOA to height z id defined as:

$$\tau_{tot}(\lambda, z, TOA) = e^{-\int_{TOA}^{z} \sum_i [k_i(\lambda, z') \, VMR_i(z')] \mathrm{d}z'} \tag{3.9}$$
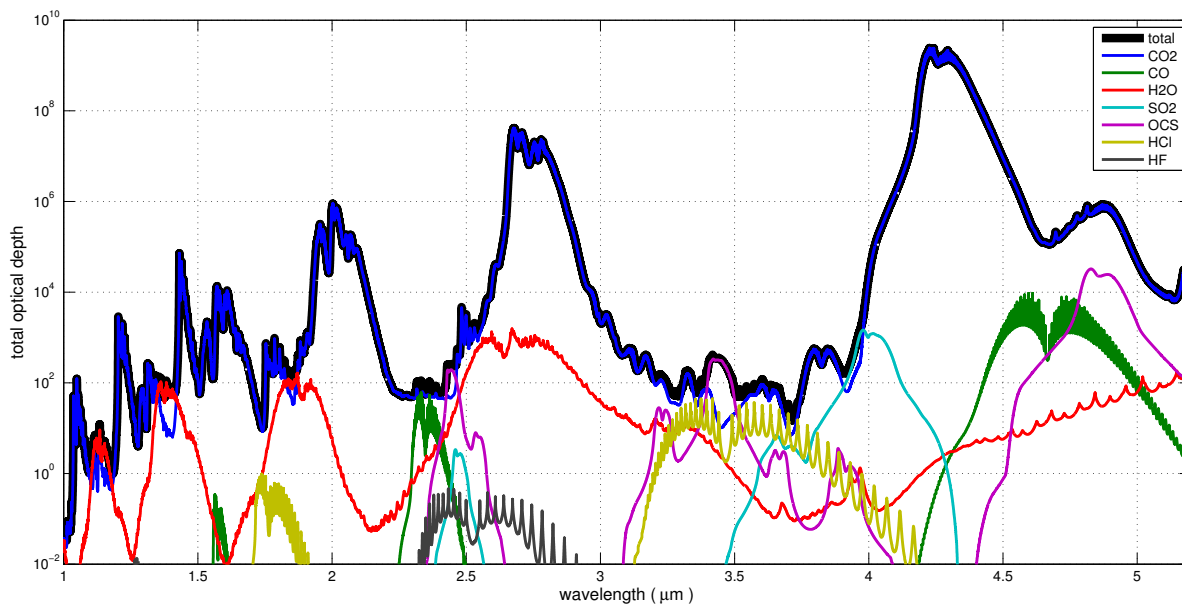
Figure 3.7: Optical depth integrated from TOA (100 km altitude) to the ground for each gas, computed with VIRA 45 profile. Total optical depth highlights the prevailing contribution of CO_2.
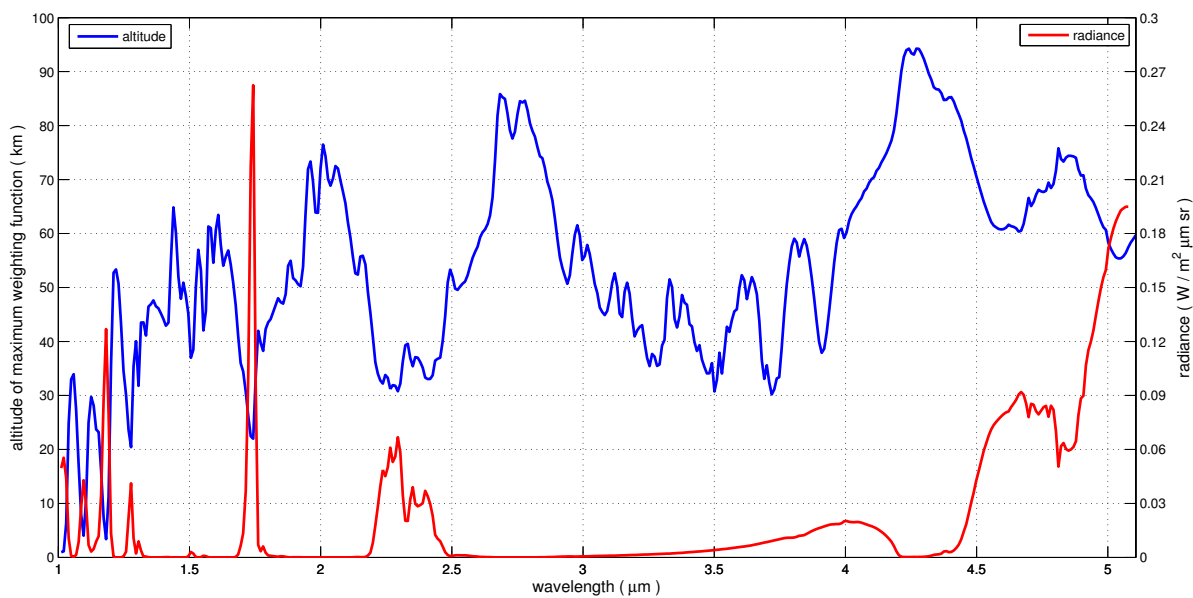
Figure 3.8: Height of maximum weighting function compared with a VIRTIS spectrum observed at nadir.

Table 3.5: Parameters used to define the Rayleigh scattering coefficients.

Gas	VMR	Depolarization factor δ	Refractive index
CO_2	0.965	0.080	$n - 1 = 0.000439 \left(1 + \frac{0.0064}{\lambda^2}\right)$
N_2	0.035	0.023	$n - 1 = 0.0002906 \left(1 + \frac{0.0077}{\lambda^2}\right)$

where the integral of the sum over all the i-th gases is the total optical depth from TOA to z. The altitude of maximum weighting function gives the maximum contribution to the observed radiance. It is noticed that at shortest wavelengths there are some atmospheric windows where radiance comes from the lower layers, almost to the surface (Figure 3.8). Their contribution is evident compared with peaks of a VIRTIS spectrum at $1.0\,\mu m$, $1.1\,\mu m$ and $1.18\,\mu m$. At other wavelengths the situation is diametrically opposite and the observed radiance comes almost entirely from the highest layers, in particular at $2.7\,\mu m$ ($\nu_1 + \nu_3$ band of CO_2) and $4.3\,\mu m$ (ν_3 band of CO_2).

3.6   Rayleigh scattering

The coefficients for molecular scattering, or Rayleigh scattering, also have to be defined. It was developed a MATLAB code to produce, given the profiles of pressure, temperature and VMR, a file similar to arsk output but containing the scattering coefficients, computed as suggested by Maiorov et al. (2005):

$$k_m(\lambda, p, T) = \frac{32\pi^3}{3L^2 k_b} \frac{1}{\lambda^4} \frac{p(z)}{T(z)} \times \sum_i f_i (n_i - 1)^2 \frac{6 + 3\delta_i}{6 - 7\delta_i} \qquad [m^{-1}] \qquad (3.10)$$

where L is the Loschmidt number, k_b is the Boltzmann constant, f_i is the VMR of the i-th gaseous species, n_i is the refractive index and δ_i is the depolarization factor. Wavelength is expressed in µm while the other parameters are expressed in SI units. To compute Rayleigh scattering only the two most abundant species, CO_2 and N_2, were taken into account, with parameters given in Table 3.5. The contribution of minor constituents is negligible, as well as the dependence of n on temperature and pressure (Maiorov et al., 2005).

The phase function for Rayleigh scattering is pre-set in the program used for radiative transfer computation, called libRadtran and described later in section 5.2, and is defined as:

$$P_m(\Theta) = a + b\cos^2\Theta \qquad (3.11)$$

where Θ is the scattering angle and
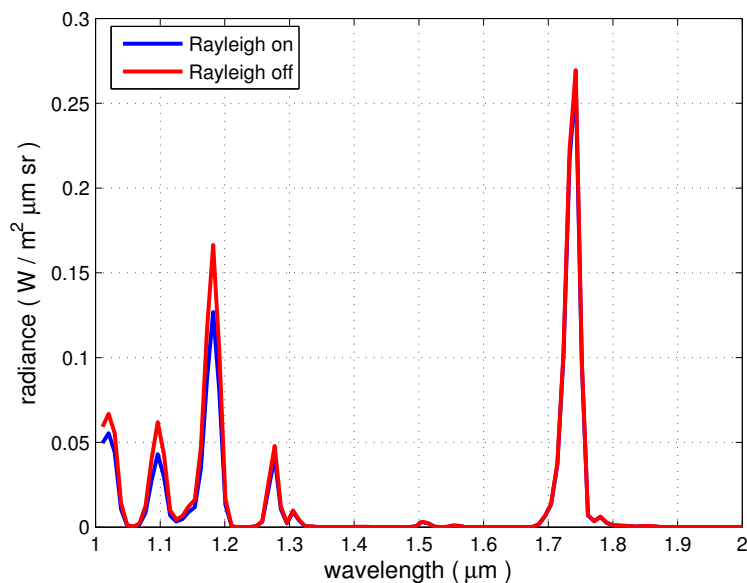
Figure 3.9: Comparison between synthetic spectra with or without Rayleigh scattering. Scattering contribution is negligible above 2 µm.

$$a = 1.5 \; \frac{1 + \delta}{2 + \delta} \; , \quad b = 1.5 \; \frac{1 - \delta}{2 + \delta} \tag{3.12}$$

where δ is the depolarization factor (Bodhaine et al., 1999). On Venus, where almost the entire atmosphere is composed of CO_2, it is $\delta \approx \delta_{CO_2} = 0.08$.

Dependence of the scattering coefficient on $1/\lambda^4$ reduces its importance with increasing wavelength, so that it becomes minimum just at 1.5 µm and completely negligible above 2 µm. On the contrary, at about 1 µm the scattering contribution must not be neglected because it affects spectrum from 15% to 45% (Figure 3.9).

Chapter 4

The atmosphere of Venus: clouds and hazes

In addition to gases properties, it is necessary to describe the aerosols distribution and optical properties. The chemical composition of Venus' aerosols is completely different to the Earth's. It is an aqueous solution of sulphuric acid with concentration varying, by weight, between 75% and 98% (Mills et al., 2007). It is believed that H_2SO_4 formation mainly occurs by photochemical processes at about 62 km altitude from H_2O and SO_2 of volcanic origin. The main cloud deck on Venus extends all over the planet between 48 and 70 km altitude about (Knollenberg and Hunten, 1980). The clouds top is usually defined as the height where the aerosols optical depth, integrated from TOA at 1 µm, becomes unitary (Esposito et al., 1983; Zasova et al., 2007; Haus et al., 2014). The vertical structure of the clouds is characterized by growth of aerosols size with decreasing altitude, so that the clouds can be divided into upper, middle and lower clouds (see Chapter 1). The particles grow by coagulation or direct condensation of H_2SO_4 on volcanic ashes nuclei. Above this cloud layer, submicrometer aerosols were observed, usually called hazes. Hazes in the upper atmosphere of Venus form in part by condensation of H_2SO_4 on meteoritic dusts (Kalashnikova et al., 2000; Gao et al., 2014) and in part they are the result of transport of small aerosols from the upper clouds layer.

4.1 Aerosol distributions

In literature they usually defined 3-4 particles types depending on their size, mainly deduced from Pioneer missions data (Kawabata et al., 1980; Knollenberg and Hunten, 1980) and called "modes" (Figure 4.2). Mode 1 is formed of small size particles, with typical modal radius equal to 0.3 µm, which are distributed throughout the cloud layer and also form the upper hazes. Mode 2, with modal radius 1.0 µm, is mainly observed in the upper and middle layer of the cloud deck; it's the most studied and well-known.

Table 4.1: Parameters of the log-normal distribution.

Mode	1	2	2'	3
r_m (µm)	0.3	1.0	1.4	3.65
σ	1.56	1.29	1.23	1.28

Mode 2' is a variation of mode 2 extending in the middle and lower clouds. It is defined to describe the growth of mode 2 size with decreasing altitude and has modal radius equal to 1.4 µm. Mode 3 corresponds to the bigger particles, with modal radius 3.65 µm, present in the middle and lower layer of the clouds. Characterization of mode 3 is a still unresolved controversy (Mills et al., 2007; Zasova et al., 2007). Some observations of Pioneer missions seem to be compatible with solid, non spherical, asymmetric, possible crystalline particles with irregular shape and chemical composition that may actually be different from the other modes (Knollenberg and Hunten, 1980) but no proposed solutions come to a definitive agreement for now. Since their characterization is not a goal of the thesis, mode 3 particles will be considered as spherical particles made of H_2SO_4 in aqueous solution as well as the other modes, as usually considered in literature (Pollack et al., 1993; Tsang et al., 2008; Haus and Arnold, 2010; Haus et al., 2013).

The most cited parametrization in literature to describe Venus' aerosols is that suggested by Pollack et al. (1993), who is cited by almost all the authors. It is considered a log-normal particle size distribution $n(r)$, whose typical parameters are given in Table 4.1 for the four modes and a graphic representation is shown in Figure 4.1.

$$n(r) = \frac{1}{\sqrt{2\pi}\ln\sigma}\frac{1}{r}e^{-\frac{1}{2}\left(\frac{\ln(r/r_m)}{\ln\sigma}\right)^2} \qquad [\mu m^{-1}] \tag{4.1}$$

To describe the cloud deck, the initial model was referred to the parametrization suggested by Haus et al. (2013), but at least other four possible clouds models are reported in Barstow et al. (2012). The particle number density depending on altitude is defined as:

$$N(z) = \begin{cases} N_0(z_b)e^{-(z-(z_b+z_c))/H_{up}} & z > (z_b + z_c) \\ N_0(z_b) & (z_b + z_c) \leq z \leq z_b \qquad [cm^{-3}] \\ N_0(z_b)e^{-(z_b-z)/H_{lo}} & z < z_b \end{cases} \tag{4.2}$$

where the parameters are described in Table 4.2.

The suggested particle density distributions don't consider aerosols above 86 km altitude. On the contrary, analysis by Wilquet et al. (2009) of solar occultation observations by SPICAV, on board Venus Express, show hazes well above this limit, up to 100 km. The profiles suggested by Haus et al. (2013) were then completed with the results of Wilquet et al. (2009). The resulting profiles are shown in Figure 4.2. In section 5.3.6 it will be shown that the upper hazes added above 86 km have negligible influence on
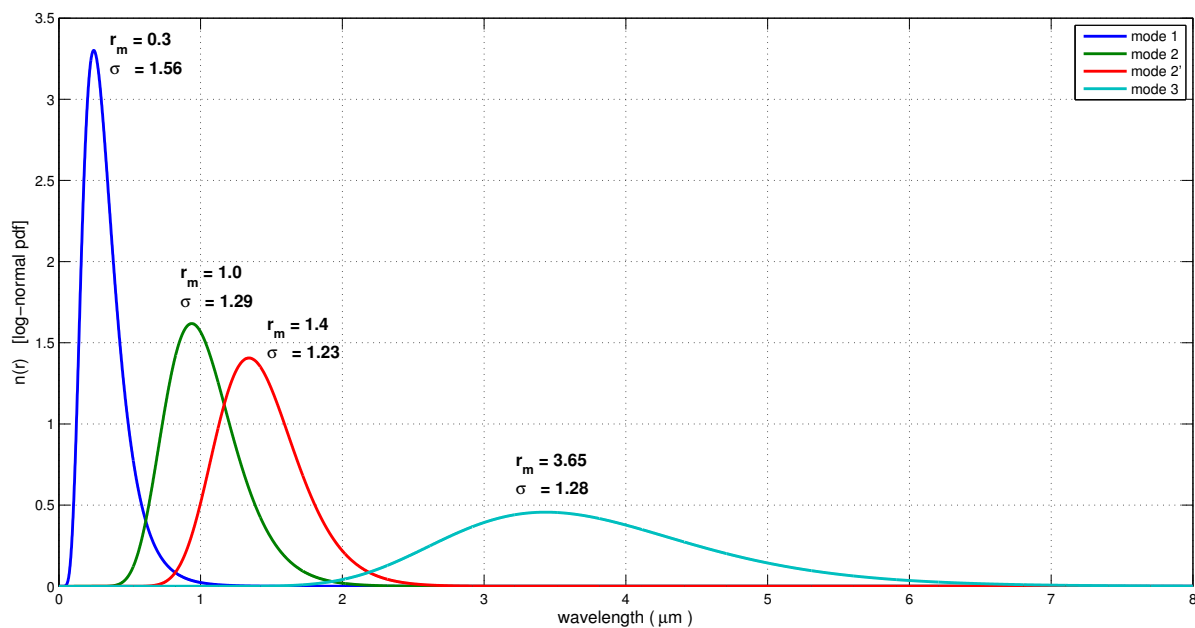
Figure 4.1: Particle size distribution for the four modes.
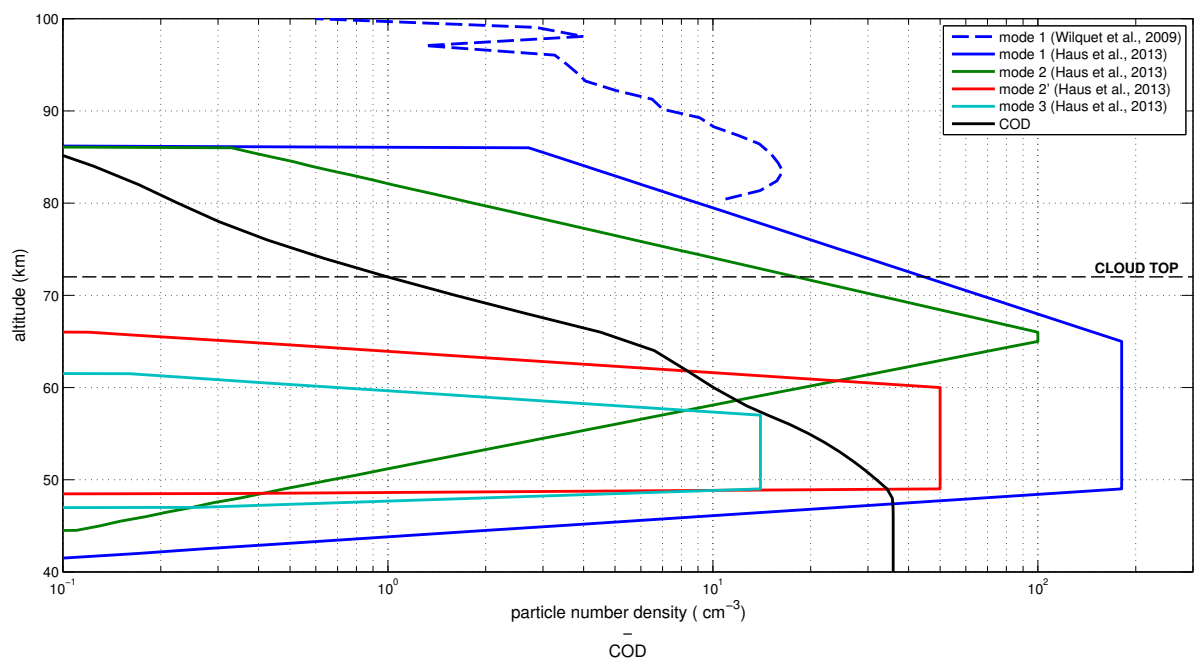
Figure 4.2: Particle number density depending on altitude for the four modes defined in the model. Cumulative Optical Depth (COD) from TOA at $1\,\mu m$ is also indicated. Cloud top is defined where COD=1.

Table 4.2: Parameters for the analytical description of the initial cloud model.

Mode	1	2	2'	3
Lower base of peak altitude z_b (km)	49	65	49	49
Layer thickness of constant peak particle number z_c (km)	16	1	11	8
Upper scale height H_{up} (km)	5	3.5	1	1
Lower scale height H_{lo} (km)	1	3	0.1	0.5
Particle number density N_0 at z_b (cm^{-3})	181	100	50	14

nadir observations. From now on, this vertical cloud profile with 75% concentration of sulphuric acid will be cited as "reference model".

4.2   Chemical composition

Usually in literature they consider for aerosols a 75% or 84% solution by weight of H_2SO_4 for all the modes, where 75% is the widest accepted (Pollack et al., 1993; Zasova et al., 2007; Grassi et al., 2008; Tsang et al., 2008; Bézard et al., 2011; Haus et al., 2014). Nevertheless, still exist an open debate about aerosol composition. For example, Kransopolsky (2012) states that the widespread value of 75% at the clouds top is incompatible with spectroscopic data and requires the H_2O mixing ratio of 25 ppm at 68 km that is not supported by the observations. Values of 25%, 38%, 50%, 75%, 84% and 96%, whose refractive indexes are described in Palmer and Williams (1975), were all verified. Solutions lower than 75% have no match in literature but they were considered for some sensitivity analysis (section 5.3.3). Refractive index values are shown in Figure 4.3. At wavelengths shorter than 2 µm the imaginary index is negligible, so aerosols at these wavelengths have no absorption properties and they are pure scatterers. Single scattering albedo is indeed close to 1 at short wavelength, then it rapidly diminishes above 2.5 µm about (Figure 4.4). It is noticed an evident separation of refractive indexes in two groups, for solutions higher than 75% or lower than 50%, depending on the predominant chemical species, H_2SO_4 or H_2O respectively.

To verify if the condensation nuclei contribute to the optical properties of the aerosol particles, some tests were performed. Optical properties were computed for H_2SO_4 particles with a meteoritic dust nucleus of 1 nm radius, as suggested by Gao et al. (2014) for the haze particles. The optical properties of meteoritic dust were taken from Shettle and Volz (1976). Sensitivity analysis show that such a small nucleus doesn't produce significant changes in particle optical properties. Differences between particles with and without nucleus are lesser than 2‰.
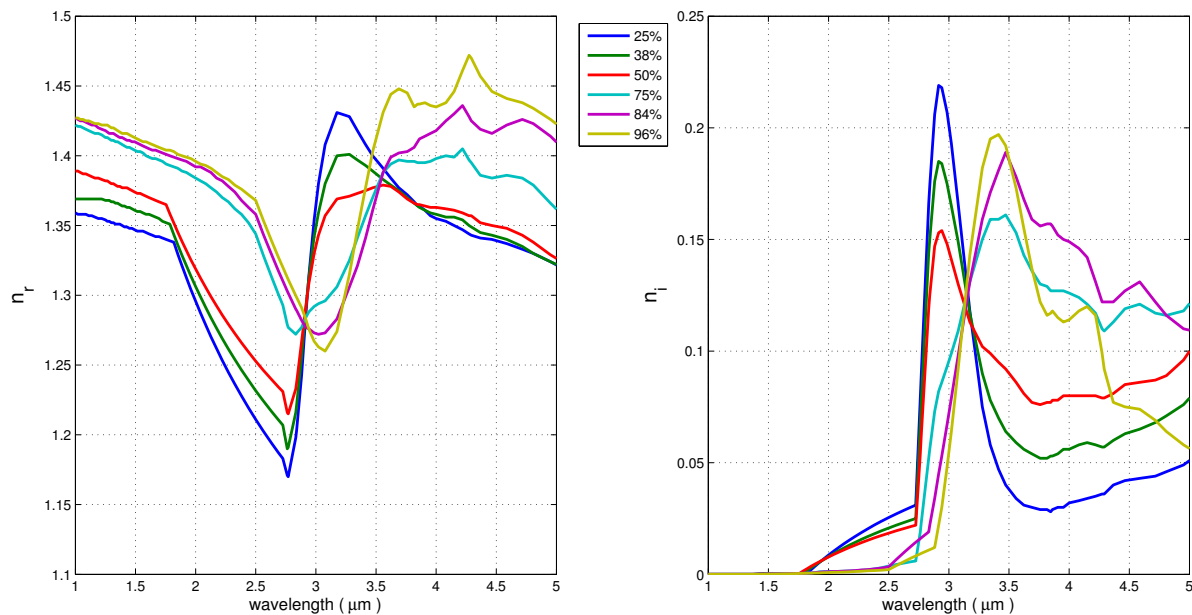
Figure 4.3: Real (left) and imaginary (right) refractive index for different concentrations of sulphuric acid.
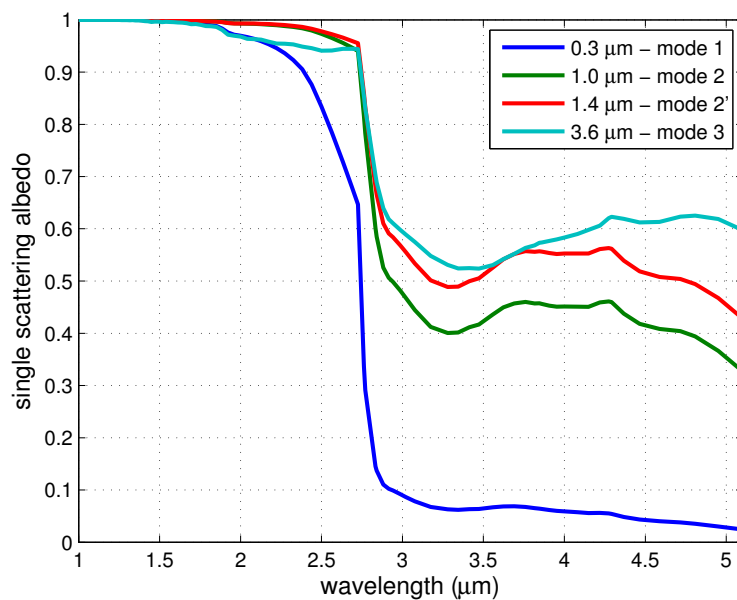
Figure 4.4: Single scattering albedo for the four particles modal radii. H_2SO_4 solution is at 75%.

4.3   Optical properties

To compute the aerosols optical properties it was used the software Scattnlay by Peña and Pal (2009) and its output was then processed with a MATLAB code. Scattnlay computes the optical properties of a spherical particle, knowing its radius and refractive index. It's also able to handle the particle as a series of concentric shells with variable properties in each one. This capability was used in the previous section to test the meteoritic nucleus. Depending on the scattering parameter $x = 2\pi r/\lambda$ (r =particle radius, λ =wavelength), Scattnlay computes extinction efficiency Q_e, scattering efficiency Q_s and scattering amplitudes S_1 and S_2. The phase function P, normalized to 4π, is:

$$P(\Theta, \lambda, r) = \frac{2}{x^2 Q_s(x)} (|S_1(\Theta, x)|^2 + |S_2(\Theta, x)|^2) \tag{4.3}$$

where Θ is the scattering angle, which is related to zenith angle θ and azimuth angle ϕ by:

$$\cos\Theta = \cos\theta\cos\theta' + \sin\theta\sin\theta'\cos(\phi - \phi') \tag{4.4}$$

Since each mode is defined by the particle size distribution n_i (equation (4.1)), the phase function P_i for each mode can be computed as:

$$P_i(\Theta, \lambda) = \frac{\int P(\Theta, \lambda, r) Q_s(x)\pi r^2 n_i(r)\mathrm{d}r}{\int Q_s(x)\pi r^2 n_i(r)\mathrm{d}r} \tag{4.5}$$

where i refers to mode 1-2-2'-3 respectively. The total phase function P_{tot}, which represents the aerosol mixing at each altitude z of the model, is defined as:

$$P_{tot}(\Theta, \lambda, z) = \frac{\sum_i P_i(\Theta, \lambda) k_{s,i}(\lambda, z)}{\sum_i k_{s,i}(\lambda, z)} \tag{4.6}$$

where $k_{s,i}$ is the scattering coefficient of the i-th mode at different altitudes, defined as a function of the particle number density N_i (equation (4.2)):

$$k_{s,i}(\lambda, z) = \int Q_s(x)\pi r^2 N_i(z) n_i(r)\mathrm{d}r \tag{4.7}$$

The libRadtran package used to solve the radiative transfer equation (see section 5.2) needs as input the phase function defined as Legendre polynomials. An expansion of 48 polynomials was established as a good compromise between phase function description accuracy and computation time. Phase functions are sufficiently "smooth" to be adequately described with such polynomials (Figure 4.5):

$$P_{tot}(\Theta, \lambda, z) = \sum_{l=0}^{48} (2l+1)\,\omega_l(\lambda, z) P_l(\Theta) \tag{4.8}$$
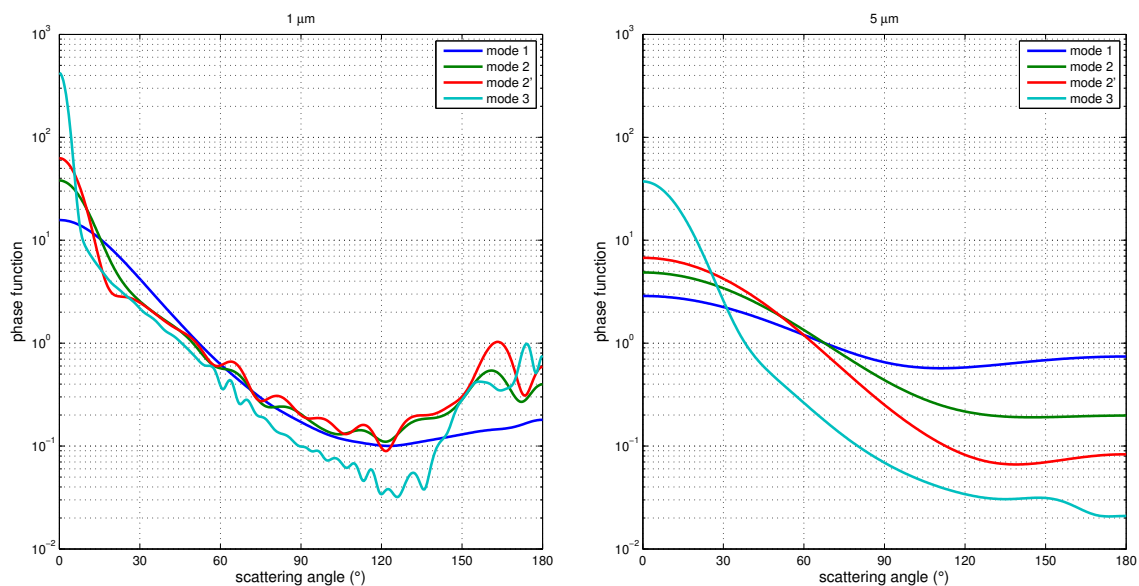
Figure 4.5: Phase function for the four particle modes, computed at $1\,\mu m$ (left) and $5\,\mu m$ (right) as in equation (4.5). H_2SO_4 solution is at 75%.

where

$$P_l(\Theta) = \frac{1}{2^l l!} \frac{\mathrm{d}^l}{\mathrm{d}(\cos\Theta)^l} [\cos^2\Theta - 1]^l \tag{4.9}$$

and

$$\omega_l(\lambda, z) = \frac{1}{2} \int P_{tot}(\Theta, \lambda, z) P_l(\Theta) \mathrm{d}(\cos\Theta) \tag{4.10}$$

In addition to phase function, libRadtran needs other input to define the aerosol optical properties. For each layer of the model, the total extinction coefficient:

$$k_{e,tot}(\lambda, z) = \sum_i k_{e,i}(\lambda, z) = \sum_i \int Q_e(x) \pi r^2 N_i(z) n_i(r) \mathrm{d}r \tag{4.11}$$

and the single scattering albedo of the particle distribution:

$$\tilde{\omega}_{tot}(\lambda, z) = \frac{\sum_i \tilde{\omega}_i(\lambda, z) N_i(z)}{\sum_i N_i(z)} \ , \quad \tilde{\omega}_i(\lambda, z) = \frac{k_{s,i}(\lambda, z)}{k_{e,i}(\lambda, z)} \tag{4.12}$$

Chapter 5

Statistical retrieval of Venus' clouds parameters

Analysis of the VIRTIS data archive requires long computational time because of the large number of data and the large number of degrees of freedom of the problem. Data selection was performed to reduce the archive size with the criteria defined in section 5.1. An extensive dataset of synthetic simulated spectra was created by assuming multiple atmospheric and clouds conditions by means of a line-by-line multiple scattering forward model. For each observation an atmospheric and cloud state was retrieved. In addition to the usual cloud parameters that are considered in the models proposed in literature (that are the aerosol particles number density and the clouds height) other parameters were taken into account and tested, such as changes in the particles size distribution (usually assumed constant all over the planet) and variations of the sulphuric acid concentration within the cloud deck (usually assumed constant throughout the entire atmosphere).

5.1 Data selection

The archive of VIRTIS-M IR data consists of 517 orbits performed from 14 May 2006 to 3 February 2011 (after this date the instrument went off). Each orbit is divided into sub-sections so that the total number of available cubes is 4537, with several different conditions of observation all over the planet. Only observations above the northern hemisphere of Venus were selected because the orbit is closest to the surface and the pixel footprint is relatively small at nadir. VEx reaches pericentre between 80° N and 90° N, obtaining a spatial resolution of about 500 m at 45° N, observed from 760 km altitude. In the southern hemisphere the pixel footprint is very wide, about 7.8 km resolution at 45° S, observed from 32000 km altitude. Only cubes in nocturnal observations were selected, with a viewing angle of the instrument between 0° and 1° (that is considered nadir viewing). These conditions reduce the dataset to only 90 cubes available (90 different
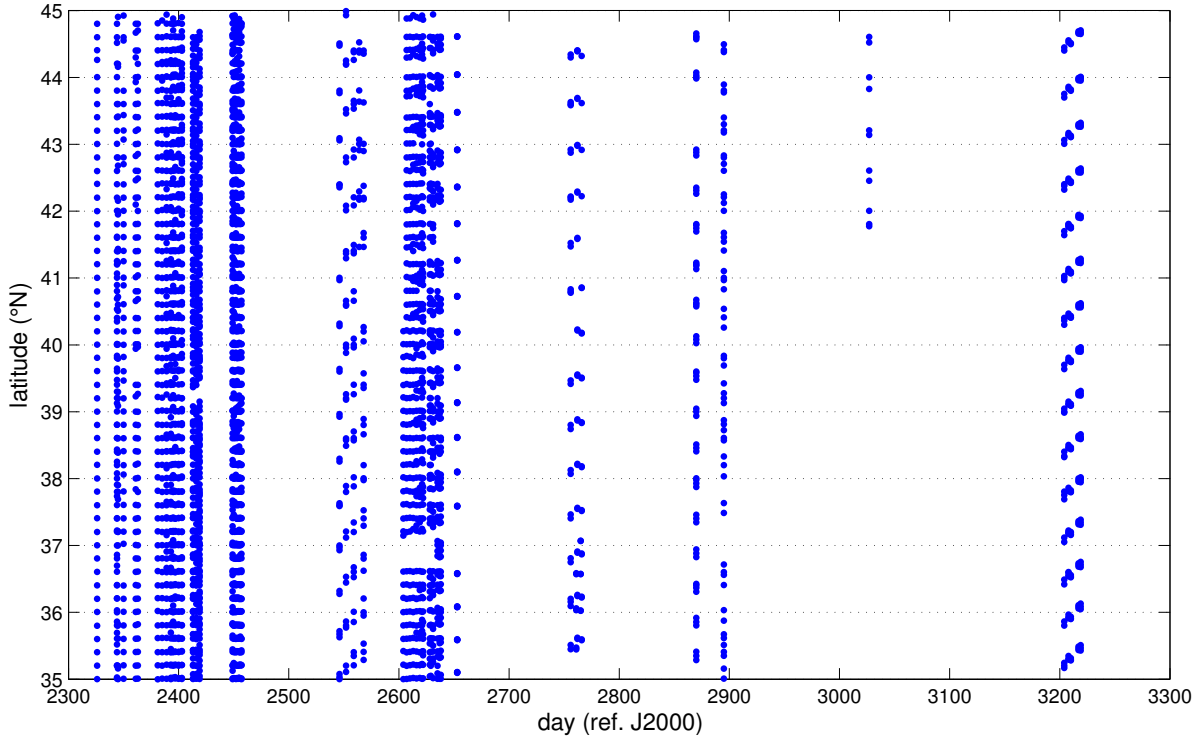
Figure 5.1: Distribution of nocturnal nadir looking VIRTIS observations as a function of day (reference is 01/01/2000) for the analysed latitude band (35-45° N).

days spanned over the whole lifetime mission). The useful observations are strongly reduced with respect to the initial database since the majority of nadir observations were taken in the southern hemisphere.

To carry out a statistical analysis of the nadir dataset an additional selection was performed limiting the latitude band between 35° N and 45° N. This choice allows to maintain a small pixel footprint (benefiting of spatial homogeneity within the pixel) avoiding possible interactions with the cold collar (60°-80°) and the hot dipole (75°-85°) (Zasova et al., 2007). The selection includes 59 cubes and 38401 observations (Figure 5.1). All the cubes have a similar structure for nadir observations: a very narrow scan in longitude (the maximum width is about 0.8°) but extended in latitude from the north pole to the equator due to the near polar orbit. Therefore, atmospheric changes are mainly visible as meridional variations looking as horizontal stripes in the images (Figure 5.2). Observations were then grouped into bins of 0.2° of latitude and 0.2° of longitude (about 21 km x 16 km footprint at 40° N). For each bin data are averaged with the assumption that the measured radiance is representative of an homogeneous scene (Figure 5.3). The choice of the bin amplitude has been made after testing the latitudinal/longitudinal variation of radiance from one pixel to another. Figure 5.4 shows radiance changes
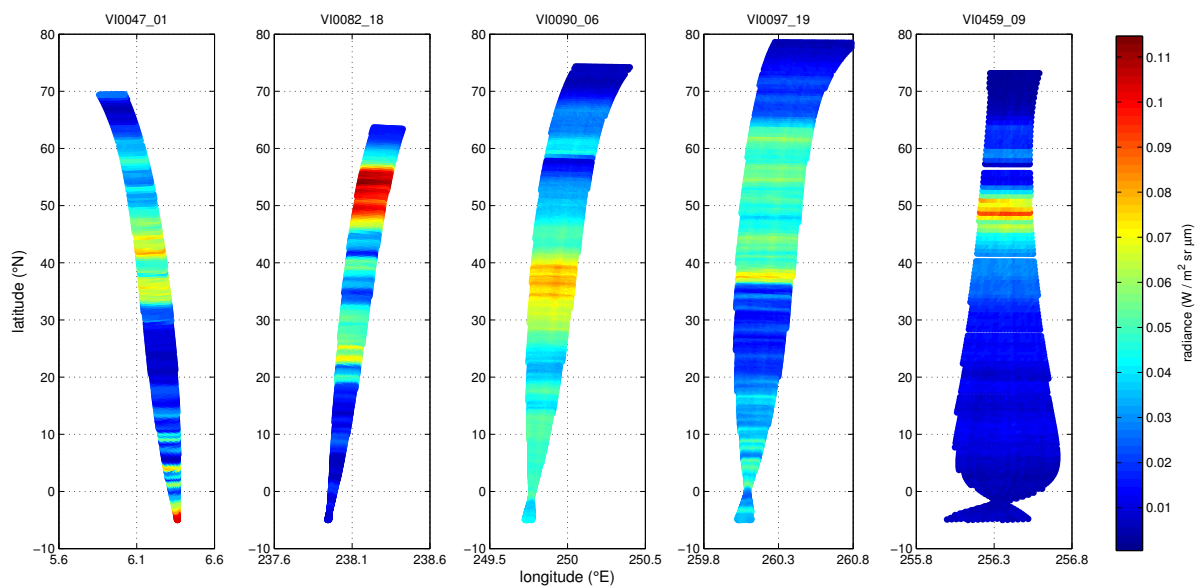
Figure 5.2: Radiances observed at 1.74 µm for five different cubes. Zonal features are clearly visible.
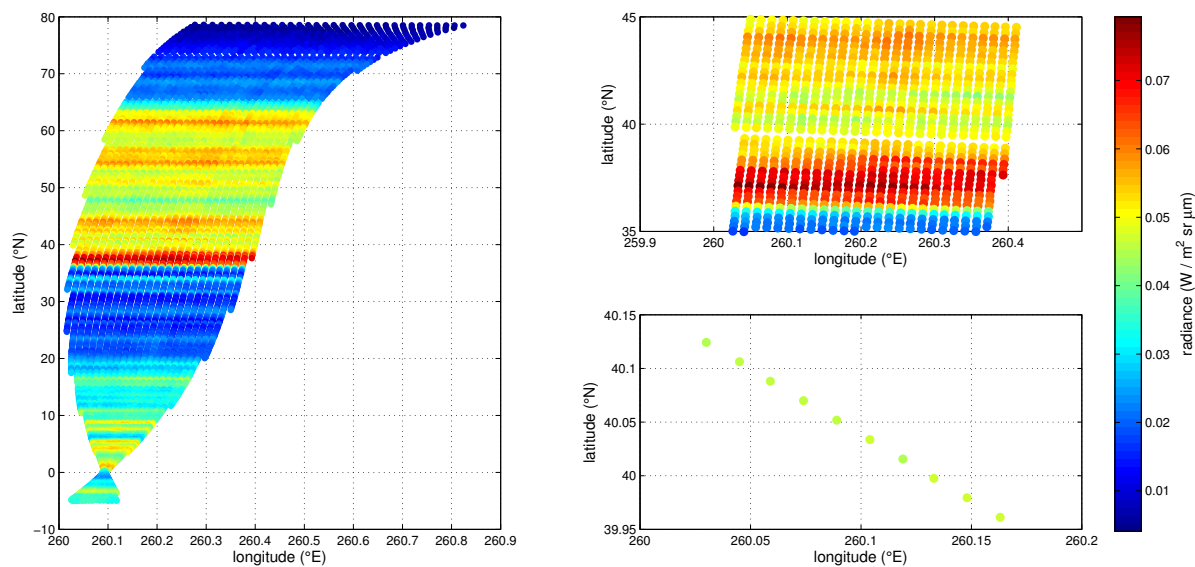
Figure 5.3: Example of data selection on the cube VI0097_19 (27/07/2006). Each dot corresponds to a single observation; radiances are measured at 2.3 µm (colorbar on the right). Left: all the nocturnal nadir observations of the cube. Top right: observations in the latitude band 35-45° N. Bottom right: one of the selected bins of 0.2°x0.2°.
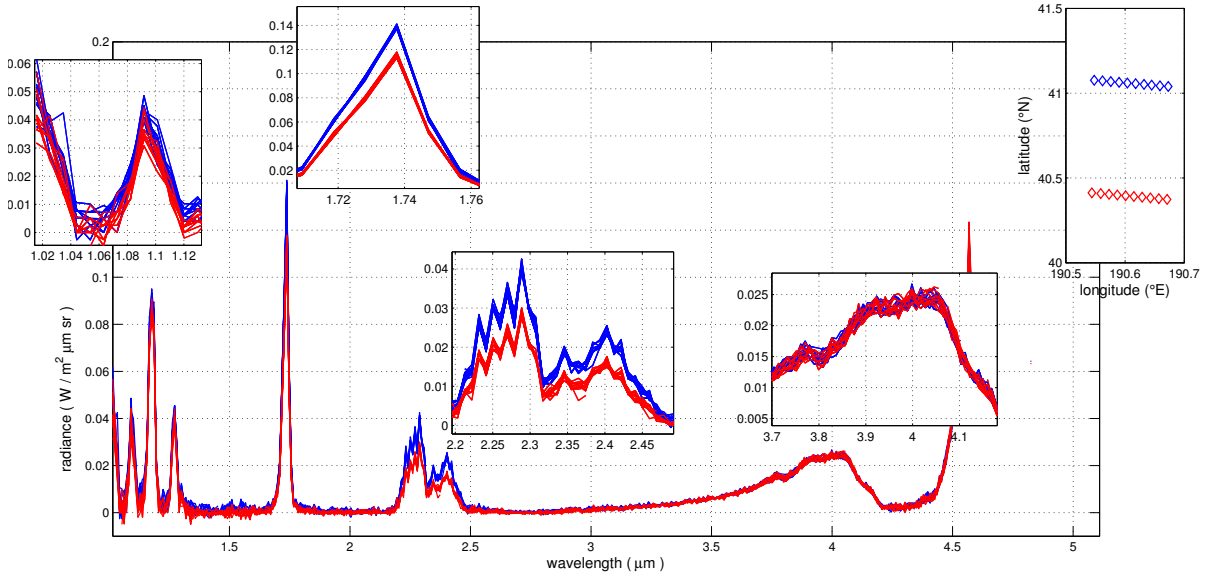
Figure 5.4: 20 observations in the cube VI0901_03 (08/10/2008). Differences between observations at different latitudes are noted (shown in the top-right inset) in the 1.74 µm and 2.3 µm windows, whereas measured radiances are almost identical near 1 µm and at 4 µm.

over about 0.7° of latitude for the cube VI0901_03, where evident separation of two groups of observations is noticed depending on latitude, whereas little changes are visible depending on longitude. Bin selection was performed automatically with a MATLAB script; bins containing only one or two observations were removed from the dataset because it was impossible to implement Chauvenet's criterion for outliers removal (section 5.1.1). Finally, the dataset was reduced to 3738 bins for a total of 37635 observations.

5.1.1   Chauvenet's criterion: outliers removal

Radiance measures at specific wavelengths show evident outliers mainly due to cosmic rays, ionising radiation or electrical surges. They look like isolated peaks in the spectrum with very high absolute values, both positive and negative. To remove these outliers, before averaging data inside each bin, the Chauvenet's criterion was used. Chauvenet criterion states that: given a sample of N measurements $x_1, x_2, \ldots, x_n$ assumed to be normally distributed around the mean x_m with standard deviation σ_m, a datum x_i can be rejected if the probability to obtain a value as deviant as x_i is less than $1/(2N)$ (Figure 5.5). The criterion was applied to each bin at every wavelength to remove the outliers. After the outliers removal, data within each bin were averaged and standard deviations were calculated. These final spectra (band representative) were then analysed to retrieve clouds properties.
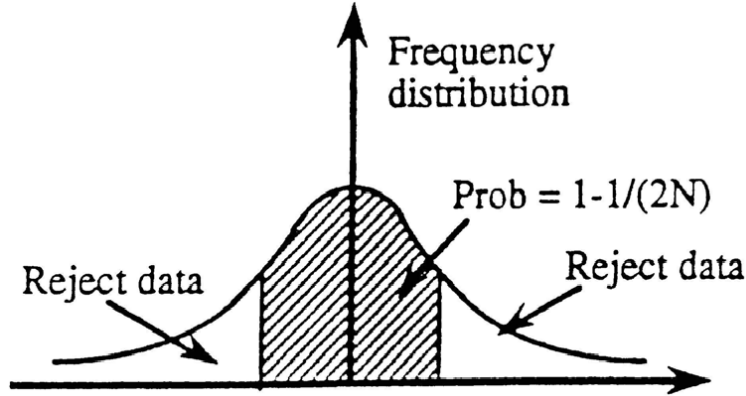
Figure 5.5: Graphic representation of the Chauvenet's criterion. N is the number of data.

5.2 The radiative transfer model: libRadtran

To create the database of synthetic spectra for the comparison with VIRTIS observations, the software package libRadtran (Mayer and Kylling, 2005) was used. The software package consists of a collection of C and Fortran functions and programs for calculation of solar and thermal radiation in the Earth's atmosphere. Since libRadtran was created for the Earth system some adaptation were necessary to work for the Venus atmosphere also. For example, thermal emission is not computed below 2 µm in the original version of the code, since it is negligible at Earth's typical temperatures; in the case of Venus thermal emission between 1 and 2 µm is significant, so the code has been implemented to perform the computation of the emitted component for lower wavelengths.

Depending on necessity, libRadtran offers different solvers for the radiative transfer equations. To simulate nadir radiances it was used DISORT, a discrete ordinate method code developed by Stamnes et al. (1988, 2000) for calculations in a plane-parallel atmosphere, and in particular the last C language implemented version CDISORT by Buras et al. (2011). In a plane-parallel atmosphere, the monochromatic equation for radiative transfer in multiple scattering conditions for an emitting atmosphere, without solar component (we are interested in nocturnal conditions), can be written as:

$$-\mu \frac{\mathrm{d}I(z,\mu,\phi)}{k_e(z)\mathrm{d}z} = \begin{aligned} &I(z,\mu,\phi) + \\ &- \frac{\tilde{\omega}(z)}{4\pi} \int_0^{2\pi} \int_{-1}^1 P(z,\mu,\phi;\mu',\phi')\, I(z,\mu',\phi')\, \mathrm{d}\phi'\mathrm{d}\mu' + \\ &- (1 - \tilde{\omega}(z))B[T(z)] \end{aligned} \qquad (5.1)$$

where $\mu = \cos\theta$ is the cosine of zenith angle, ϕ is the azimuth angle, $I(z,\mu,\phi)$ is the radiance observed at altitude z into the direction μ, ϕ, k_e is the extinction coefficient,
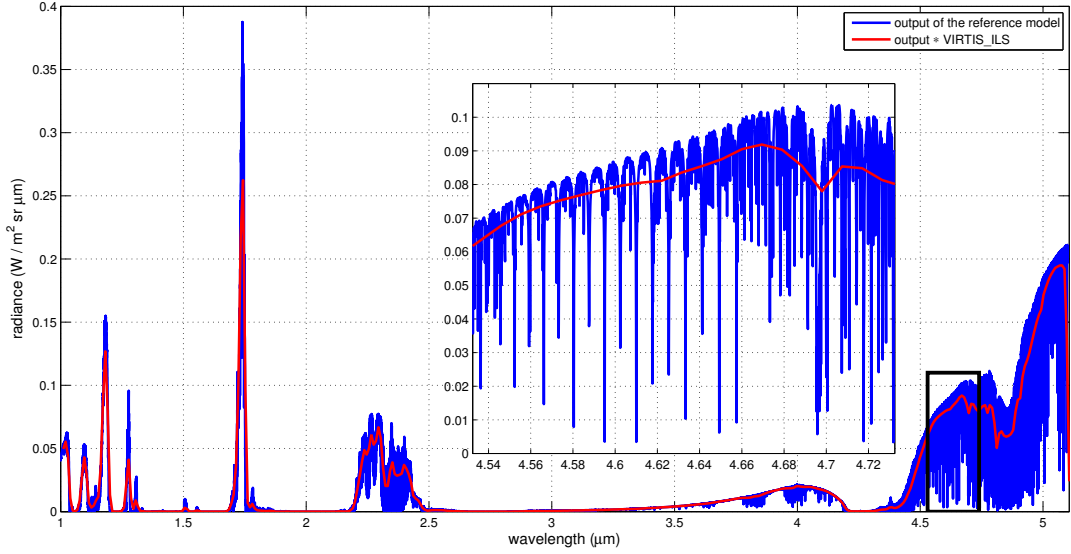
Figure 5.6: Reference model spectrum R_{ref}: 75% H_2SO_4, VIRA 45, r_1=0.3 μm, r_2=1.0 μm, $r_{2'}$=1.4 μm, r_3=3.65 μm, f_1=f_2=$f_{2',3}$=1. Blue line: libRadtran output with wavelength grid step of 0.1 nm; many gas absorption lines are evident. Red line: convolution of the high resolution output with the VIRTIS ILS. The inset shows a zoom of the selected black rectangle.

$\tilde{\omega}$ is the single scattering albedo, $P(z, \mu, \phi; \mu', \phi')$ is the phase function for radiation coming from μ', ϕ' then scattered to μ, ϕ and B is the black body emission of the layer at temperature $T(z)$. The radiative transfer equation is solved subject to boundary conditions. The bottom boundary condition, assuming Lambertian properties of the surface $(z = 0)$, can be written as:

$$\pi I(z = 0, \mu, \phi) = \pi \epsilon B(T_s) + 2\pi A \int_0^1 \mu I(0, -\mu, \phi) \, d\mu \qquad (5.2)$$

where T_s is the surface temperature, A is the surface albedo and $\epsilon = 1 - A$ is the emissivity, from Kirchhoff's law.

To solve the equation and to obtain the outgoing radiance at the top of the atmosphere it is necessary to provide a series of input to libRadtran to define the atmosphere, described in previous chapters: pressure and temperature profiles; optical depth for gases absorption; optical depth for Rayleigh scattering; extinction coefficient, single scattering albedo and phase function for aerosols. In addition, surface albedo and geometry of observation have to be defined. The output of the solver is a synthetic spectrum observed at nadir at 100 km altitude (TOA), which can be compared with an observed VIRTIS spectrum. The libRadtran output was computed with a grid step of 0.1 nm, much less that the 9.5 nm resolution of VIRTIS-M IR. Convolution of libRadtran output with the VIRTIS Instrumental Line Shape (ILS), defined as a Gaussian with FWHM

equal to 12.005 nm, in addition to sampling on VIRTIS-M IR wavelength grid generates a spectrum comparable with the observations. This process reduces information on many individual absorption lines, only visible at 0.1 nm resolution (Figure 5.6). The spectrum shown in Figure 5.6 was obtained with aerosols composed by an aqueous solution of sulphuric acid at 75%, atmospheric profile VIRA 45, modal radii r_1=0.3 µm, r_2=1.0 µm, $r_{2'}$=1.4 µm, r_3=3.65 µm, mode scale factors f_1=f_2=$f_{2',3}$=1 (see section 5.3.4). Such a spectrum will be mentioned in the text as the reference model R_{ref}.

5.3 Sensitivity analysis

To understand the way different parameters act on the modelled spectrum, some sensitivity analysis were performed by changing one degree of freedom per time.

5.3.1 Gases and aerosols

First, the bulk effect of gases and aerosols was evaluated separately simulating the atmosphere radiative transfer assuming only one of the two components respectively (Figure 5.7). Simulated brightness temperatures show the main role of the gaseous component corresponding to CO_2 absorption maxima at 1.6, 2.0, 2.7 and 4.3 µm, that it's simple to relate with results of section 3.5 about gases absorption. Aerosols effects dominate between 3 and 5 µm, with the exception of the ν_3 band of CO_2, where radiation mainly comes from layers on top of the cloud deck, from about 67 to 72 km. At other wavelengths, contributions of the two components are both important and they must be considered together, in particular, in the atmospheric windows at 1.74 and 2.3 µm as well as at shorter wavelengths, where the reference spectrum in Figure 5.6 shows a significant amount of radiance coming from the lowest part of the atmosphere.

5.3.2 Surface albedo

At the shortest wavelengths, radiance observed at TOA not only depends on the atmospheric characteristics but it is also affected by the direct contribution of the planet's surface: this is observable by evaluating the simulated radiance sensitivity to changes in surface albedo. Previous studies report a spectrally constant Lambertian surface with values ranging from 0.15 to 0.4 (Devaux and Herman, 1975; Hashimoto and Sugita, 2003; Arnold et al., 2008; Haus and Arnold, 2010). Simulations obtained in such a range of values show that the influence of the surface albedo is observed only between 1.0 and 1.2 µm, with changes from 2% to 8% in terms of radiance units (Figure 5.8). Since the albedo has a limited effect on radiance when compared to changes relate with aerosols properties (section 5.3.4) and cloud geometry all the simulations were computed assuming an albedo value of 0.2.

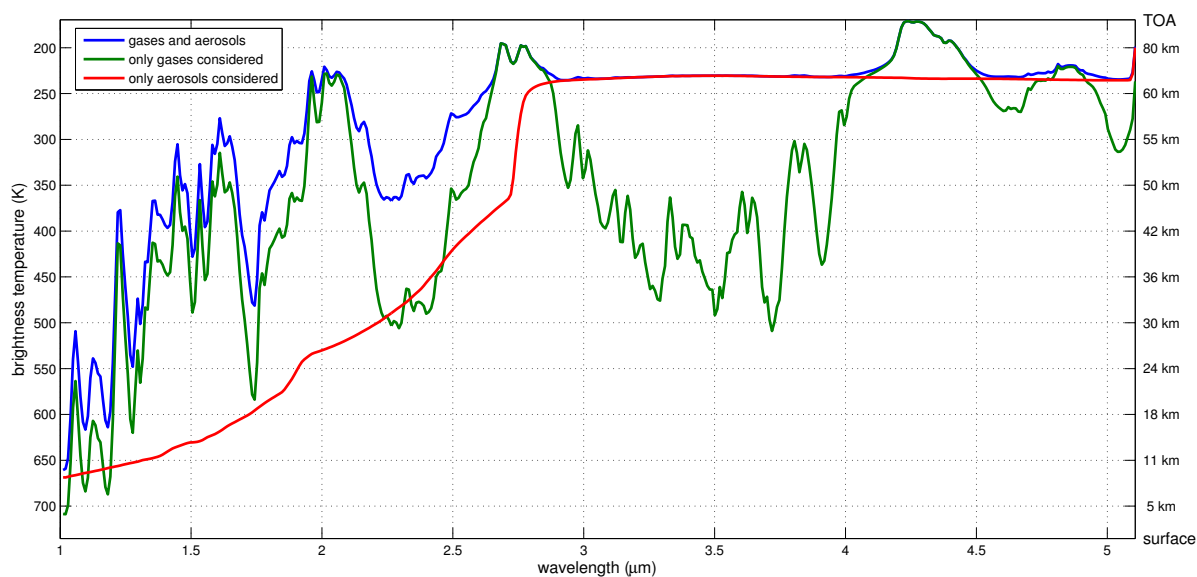**Figure 5.7:** Synthetic spectra converted into brightness temperature. Simulations without gases or aerosols are in red and green respectively. Tick marks on the right axis stay for the altitude of the VIRA 45 profile, while on the left the temperatures levels are reported.
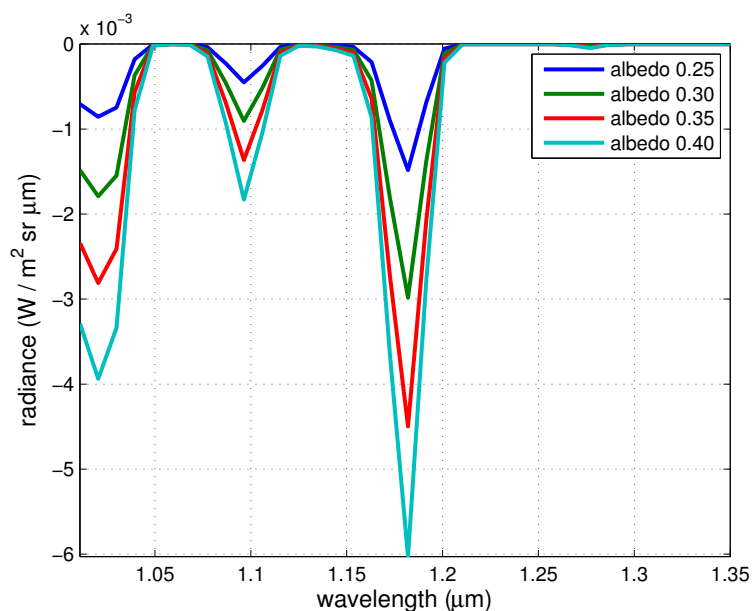
Figure 5.8: TOA Radiance sensitivity (R_{sim}-R_{ref}) to changes in surface albedo. The surface is assumed Lambertian. R_{ref}: A=0.2.

5.3.3 Sulphuric acid concentration

Modifying the H_2SO_4-H_2O solution concentration changes the optical properties of aerosols at different extent depending on wavelength. Effect on TOA VIRTIS radiances of aqueous solutions of sulphuric acid at 25%, 38%, 50%, 75%, 84% and 96% by weight were tested. Large differences in the upwelling radiance are observed for solutions of less than 75%. These kind of solutions are not reported in literature. In fact the lack of features in the 2.3 µm window does not allow any fit with the observed data. The reason lies in the fact that the imaginary refractive index of the low concentration solutions is significant in this spectral interval, due to the large percentage of water assumed in the solution (Figure 4.3. As a consequence, the derived aerosols properties are such that absorb the upwelling radiance and the resulting synthetic spectra show low radiances values that are not representative of VIRTIS observations (Figure 5.9). Therefore, Venus' clouds are not composed of such low concentration aerosols.

Solutions with concentrations of sulphuric acid larger than 75% show limited differences at the VIRTIS shortest wavelengths and at 4 µm, whereas at 2.3 µm and above 4.5 µm differences are the largest, mainly for the 96% case (Figure 5.10). In recent literature a uniform solution of sulphuric acid is considered for the modelling of Venus' clouds. The same concentration value is assumed along the whole vertical extent of the cloud layer, as stated at section 4.2. Nevertheless, many authors suggest that an increment in sulphuric acid concentration could be possible when descending through the clouds as deduced by probes data (Knollenberg and Hunten, 1980; James et al., 1997; Mills et al., 2007). To test such possibility, the cloud deck was split in two parts depending on the particles size: the modes 1 and 2 and modes 2' and 3 are dealt together. In particular it is assumed that mode 1 and 2 are representative of the upper clouds and modes 2' and 3 of the lower clouds.

Sulphuric acid mixtures of 75%/84%, 75%/96% and 84%/96% were tested, with the first term (referred to the upper part of the clouds: modes 1 and 2) always lower than the second one (referred to the lower cloud). The consequences of this cloud model, usually not performed in literature, will be evident with the analysis of data at section 5.4.

5.3.4 Particle number density and size distribution

Changes in the particle number density affect spectra at every wavelength with different strength depending on the mode considered (Figure 5.11). Sensitivity studies with respect to the reference model (Figure 4.2) were performed introducing a multiplicative factor f_i, where i refers to different aerosol modes The factor scales the particle number density equally at each altitude.

Large sensitivity of upwelling radiances due to variation of f_2 is observed for wavelengths larger than 3 µm. Mode 1 particle number density affects also (even at less extent with respect to mode 2) the radiance field above 4.5 µm. To note that most of the ra-

Figure 5.9: Simulated radiance spectra with different concentration of H_2SO_4. Values lower than 75% are not able to adequately reproduce VIRTIS features in the 2.3 µm window.
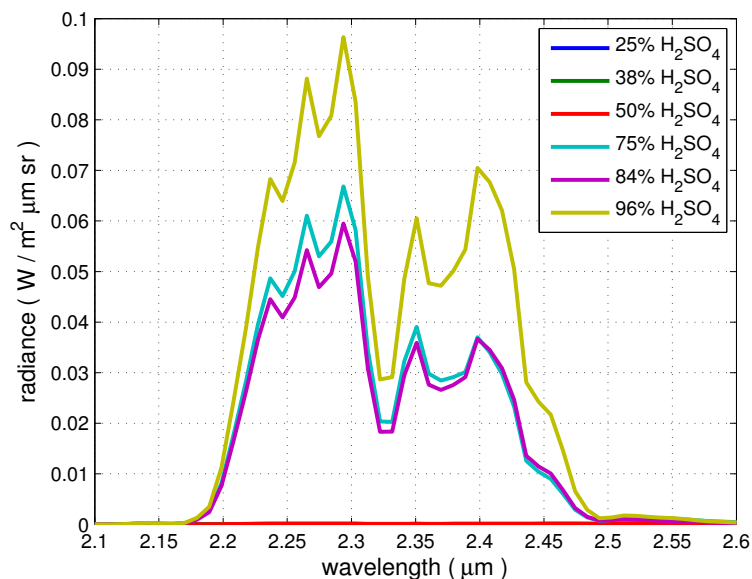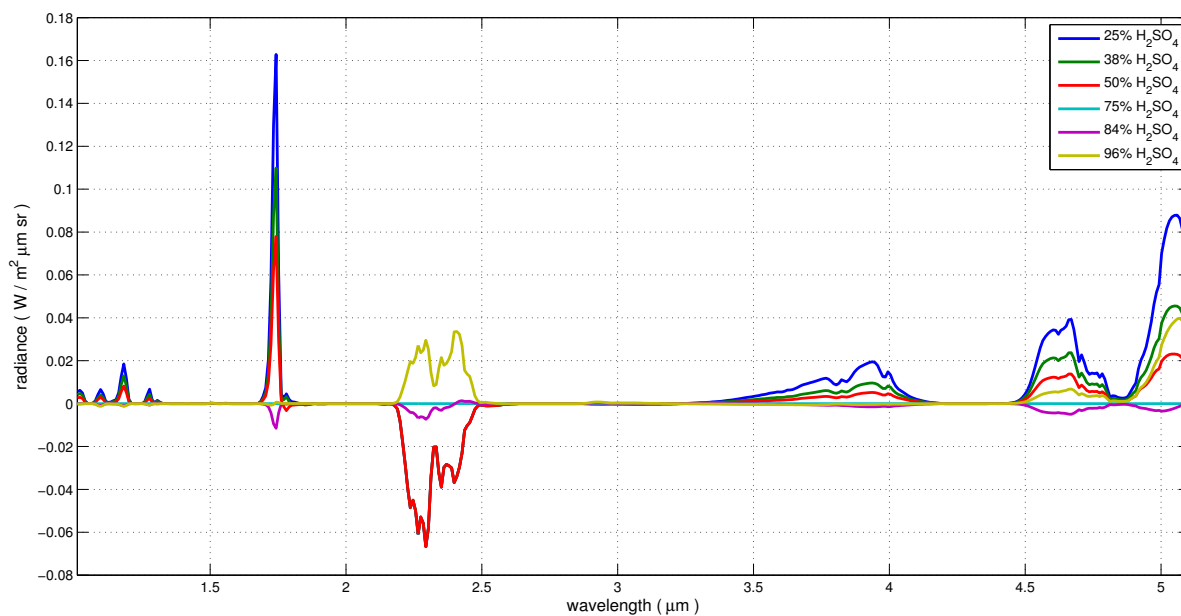

Figure 5.10: Radiance differences (R_{sim}-R_{ref}) for changes in H_2SO_4 solution. R_{ref}: 75% H_2SO_4.
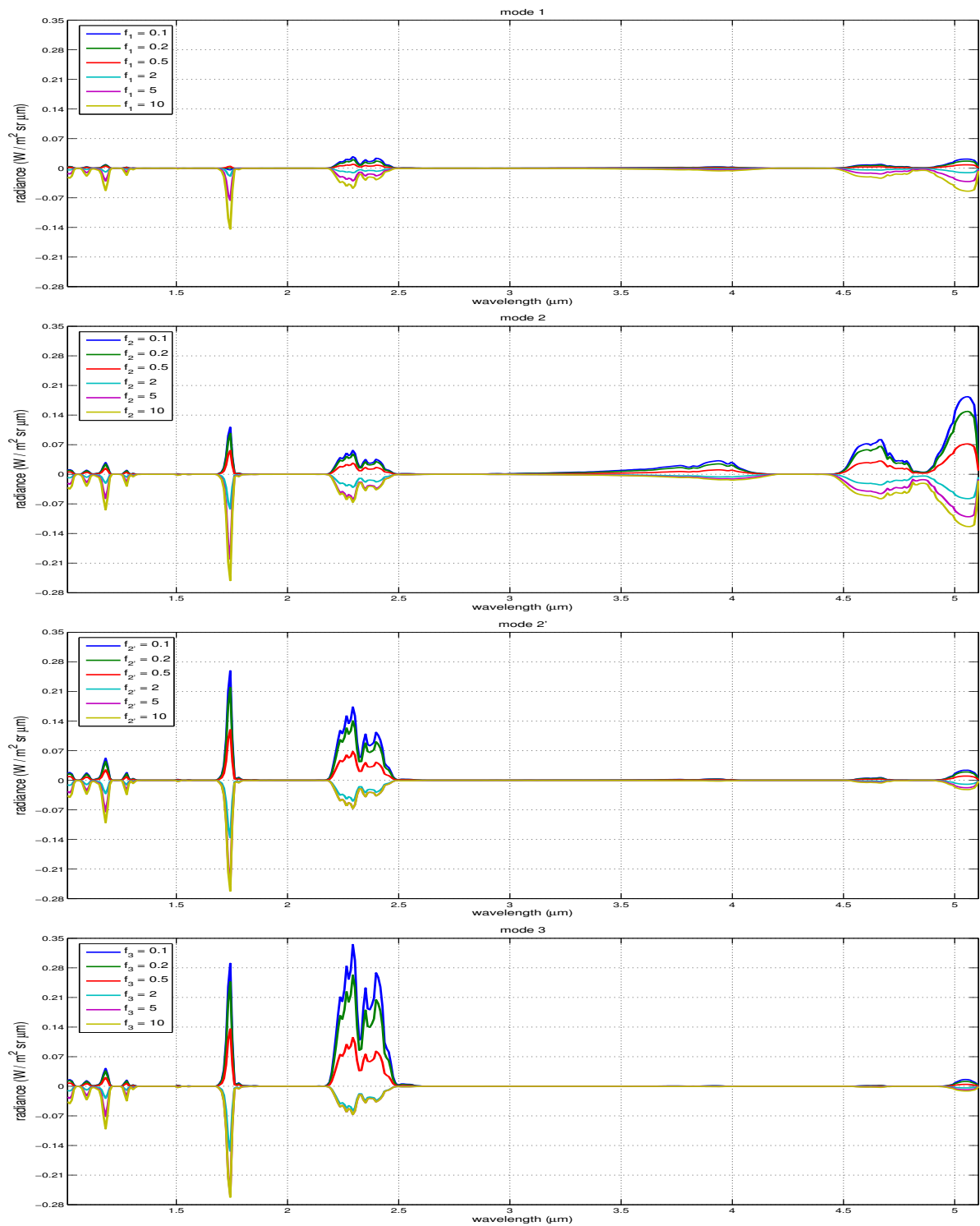
Figure 5.11: Radiance differences (R_{sim}-R_{ref}) for changes in scale factor for the four modes. R_{ref}: f_i=1.

diance at the largest wavelengths comes from the upper cloud layers, where only modes 1 and 2 have a not negligible concentration. Variations in number densities of modes 2' and 3 highly affect the spectrum features at wavelengths shorter than 2.3 µm where upwelling photons mainly originates from the lower part of the atmosphere. The effect is particularly evident when reducing their number density, whereas a high scale factor (5 or 10) acts in a similar way for modes 2, 2' and 3. For simplicity, the same scale factor was considered for modes 2' and 3 ($f_{2'}=f_3=f_{2',3}$) that have the same behaviour depending on wavelength and both describe the lower part of the cloud. What is important to note here is that for any wavelength the effect of changes in the particles number density of mode 1 are smaller than those due to other modes.

In addition, variations of modal radius r_m for the four modes were considered. Studies found in recent literature describe the aerosol microphysical properties using the modal radii defined by Pollack et al. (1993) (see section 4.1). No changes in the shape of the particles size distribution are generally accounted for. For the present study we assume realistic changes in modal radius for the log-normal particle size distribution of each mode. The ranges of used values are given in Table 5.1. The sigma of the distributions are kept fixed for simplicity. Note that increasing the modal radius of mode 2, for example, acts in a similar way to increase the mode 2' scale factor, since the two modes become similar, but the two modal radii never converge at all and they are partially defined at different altitudes. Therefore, modal radius and scale factor have different weight in the computation and their individuality is preserved.

5.3.5 Temperature and pressure profiles

Since analysed VIRTIS spectra were observed in the latitude band between 35° N and 45° N only two VIRA profiles were considered: VIRA 30 and VIRA 45. The maximum difference between the two profiles is about 3.7% in temperature at 59 km and 7.2% in pressure at 72 km. The influence on the retrieved spectrum is evident only for wavelengths above 3 µm (Figure 5.12). At short wavelengths most of the radiance comes from the lowest atmospheric layers where VIRA profiles are identical. Variation of radiance at 4 µm, due to change in VIRA profile, is about 50% of that obtained with a mode 2 scale factor equal to 0.5 and it is about 60% above 4.5 µm, so it could be masked by the uncertainty on scale factor. The actual atmospheric profile could be evaluated by comparison between the 4 µm window and one of the windows at shorter wavelength but the latter are dominated by mode 3, which however has no influence at 4 µm, so it is very difficult to disentangle doubts on temperature and pressure.

5.3.6 Upper atmospheric layers

For the nadir viewing geometry, the effect of changes in both temperature and particle number density of the uppermost layers (from 80 to 100 km altitude) on the radiance
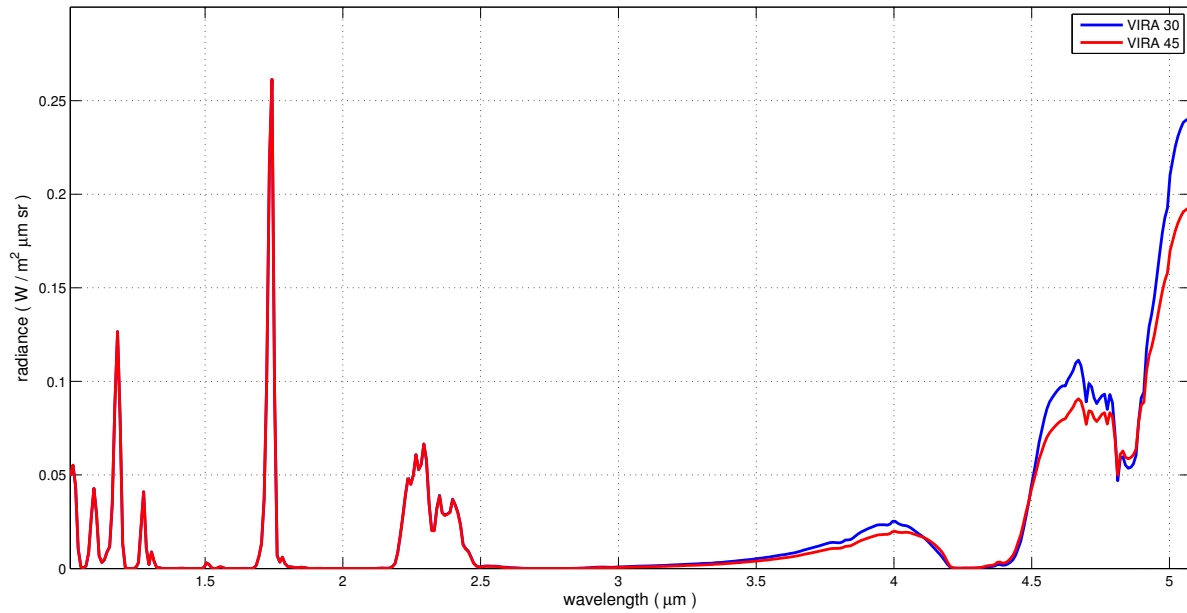
Figure 5.12: Dependence on temperature and pressure profile for the simulated spectra.
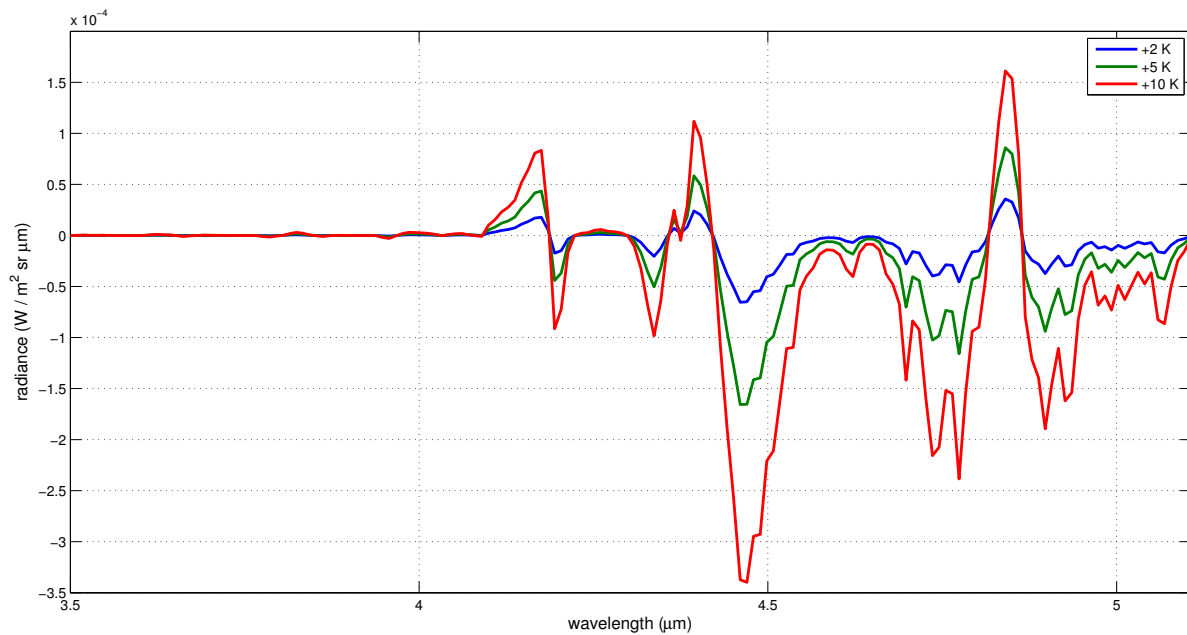
Figure 5.13: Radiance differences (R_{sim}-R_{ref}) obtained for changes in the temperature profile only above 80 km. The extent of the change is reported in the legend. The reference model assumes R_{ref}: VIRA 45.
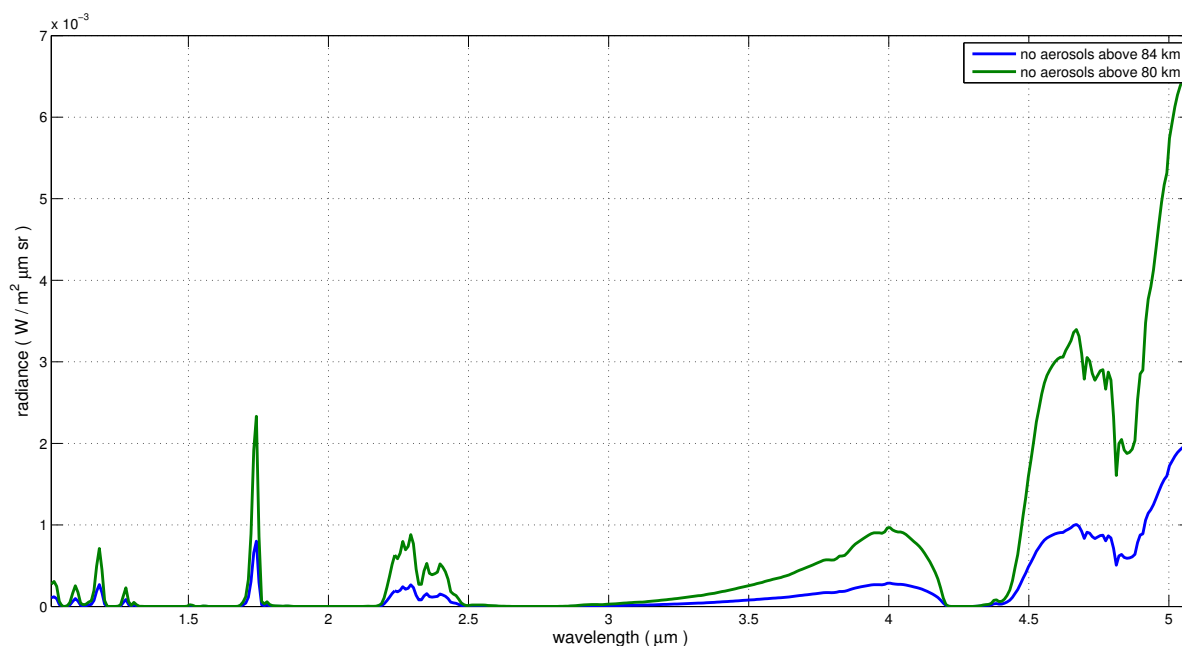
Figure 5.14: Radiance differences (R_{sim}-R_{ref}) obtained with aerosols removal from the upper atmospheric layer. Differences expressed as a percentage vary from 0.5% to 5% and from 0.2% to 1.5% for particles removal above 80 km and 84 km respectively.
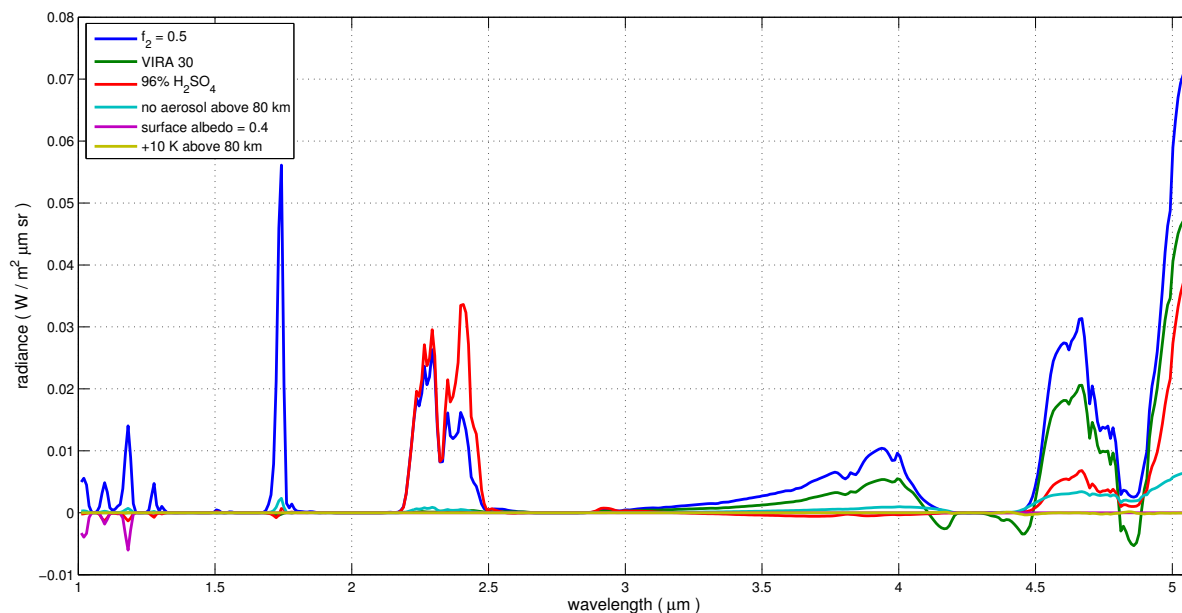
Figure 5.15: Comparison between radiance differences (R_{sim}-R_{ref}) obtained as response to parameters change reported in legend. R_{ref}: f_2=1, VIRA 45, 75% H_2SO_4, aerosols up to 100 km, surface albedo=0.2.
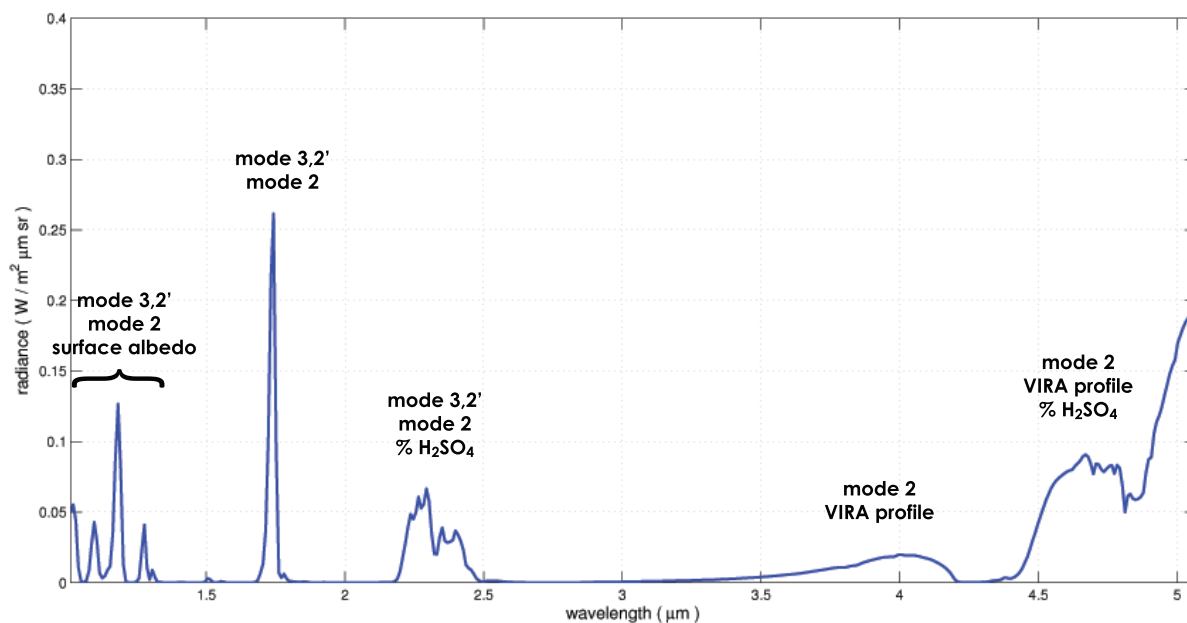
Figure 5.16: Main parameters which affect each atmospheric window, ordered in magnitude from top to bottom. Mode 1 is effective in each window but with very low magnitude so it is not indicated.

spectra is very small all over the VIRTIS spectrum. Variations of the temperature profile up to 10 K in the upper layers has an impact on the spectrum limited to wavelengths longer than $4\,\mu m$ and the effect on radiance is below 0.5% with respect to the reference model (Figure 5.13).

Complete removal of aerosols particles above 80 km (that is an extreme assumption) modifies the reference spectrum of only 0.5% at $1\,\mu m$ and 5% at $4\,\mu m$. Removal of particles above 84 km, that is the upper haze described by Wilquet et al. (2009), provide a radiance variation ranging from 0.2% to 1.5% (Figure 5.14). Such a change is at least one order of magnitude lower than that due to f_2 (Figure 5.15), so the actual contribution of the upper atmospheric layer is assumed secondary in the model.

The assumption that the nadir radiance field measured at TOA is mostly due to layers below 80-85 km allows us to retrieve the atmospheric and cloud properties below that level. This is fundamental in the analysis of limb observations (Chapter 6).

Figure 5.15 summarises some parameters used in the sensitive study and it allows a direct comparison between the orders of magnitude of each one. Figure 5.16 highlights the main parameters which affect each atmospheric window.

Table 5.1: List of variables of the model. Range of variation is also indicated.

Variable	Range or Values
p - T vertical profile	VIRA 30 - VIRA 45
H_2SO_4 concentration	75% - 84% - 96% 75%/84% - 75%/96% - 84%/96% [1]
Scale factor	
f_1	$0.1 \div 2.0$
f_2	$0.2 \div 2.0$
$f_{2',3}$	$0.7 \div 2.0$
Modal radius	
r_1	$0.1 \div 0.5$
r_2	$0.4 \div 1.4$ [2]
$r_{2'}$	$1.4 \div 2.0$
r_3	$2.8 \div 4.4$

[1] The two values refer to modes 1-2 and 2'-3 respectively.

[2] The value 1.4 was only used when $f_{2'} \neq 1.4$ to preserve modes distinction.

5.4   Best fit criterion

A large number of simulations were run with multiple assumption on the sensible parameters. Since the number of degrees of freedom is very high it is impossible to cover all the possible combinations (several billions) that can be derived from variations reported in Table 5.1. Only specific combinations were used. Some combinations were specifically chosen to perform simulations of the basic cases frequently reported in the literature.Some more simulations were performed after that a combination of parameter was chosen with a random selector over the whole sample. This allowed to have a wide representation of the typical variation of the system parameters. A database with 10227 different spectra was created, which represents the variety of the analysed VIRTIS spectra. The mean of the 37635 sampled VIRTIS observations, with three standard deviations, is within the mean of the simulated spectra when accounting for three standard deviations (Figure 5.17). Little exceptions are visible where radiance approaches zero because libRadtran always returns radiances with physical meaning (greater than zero) whereas VIRTIS data may be negative because of fluctuations on the dark current, causing calibration errors (Erard, 2012).

To retrieve the atmospheric and cloud status for each sampled bin, a comparison between the mean radiance spectrum of the bin and the whole synthetic database was performed. Best fit model was defined as the one that minimized the root mean square γ of the differences, over wavelength, between the observed spectrum R_{bin} and the simulated spectra R_{sim}, weighted on the standard deviation of the whole analysed sample:
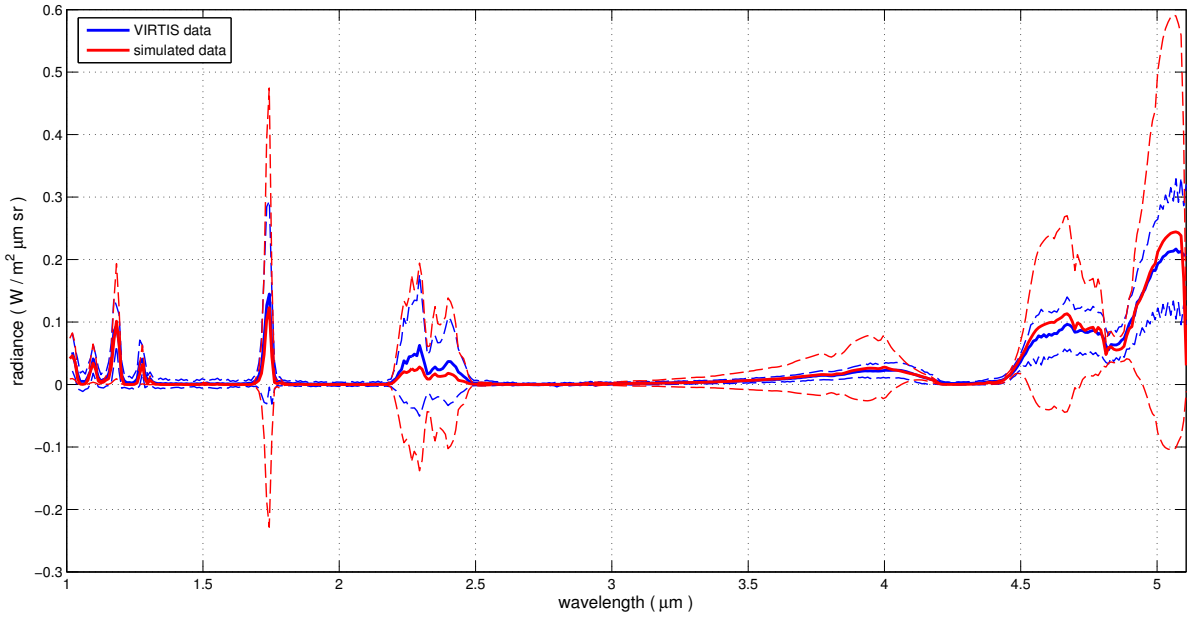
Figure 5.17: Mean of all the VIRTIS spectra (37635) acquired between 35° N and 45° N in nocturnal nadir looking (blue solid line) and mean of all the simulated spectra (10227) obtained with libRadtran (red solid line). Broken lines are plotted at three standard deviations from the means.

$$\gamma = \sqrt{\frac{1}{N} \sum_{i=1}^{N} [(R_{sim}(\lambda_i) - R_{bin}(\lambda_i))^2 \, W(\lambda_i)]} \,, \quad W(\lambda_i) = \frac{\sigma_{tot}(\lambda_i)}{\sum_{i=1}^{N} \sigma_{tot}(\lambda_i)} \tag{5.3}$$

where i refers to a specific wavelength, N is the total number of wavelengths, W is the weight associated to each wavelength. Non-window wavelengths and those above 4.5 µm were excluded from the fit: the former because we are particularly interested in fitting the cloud parameters and atmospheric windows produce useful information about the clouds; the latter because the detector often saturates in that band so most of data is missing. The weight W is defined as the standard deviation σ_{tot} of all the VIRTIS observations acquired between 35° N and 45° N in nocturnal nadir looking at that specific wavelength (all the acquired spectra, not averaged in bins) divided by the sum over wavelength. This fitting procedure focuses on radiances in the windows where largest dependence on cloud parameters is expected (which globally have larger standard deviation).

The gain obtained from the fit process is evaluated with respect to a standard simulation. The gain of information is compared with the mean noise associated to VIRTIS observations that is used as a-priori threshold. The noise of VIRTIS is not evaluated in a rigorous way for each observation because it requires the instrument transfer function
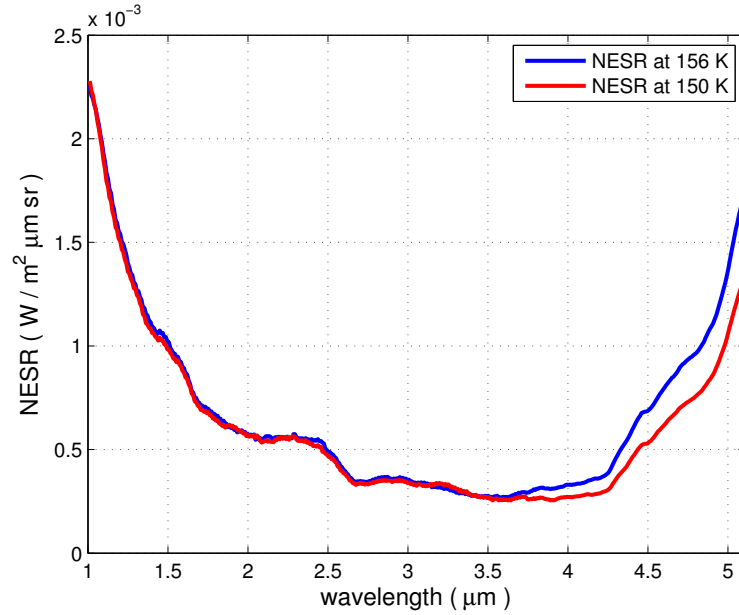
Figure 5.18: Noise Equivalent Spectral Radiance for two temperature of the detector and 0.3 s of exposure time.

to be applied to raw data and it goes beyond the scope of the present work. A Noise Equivalent Spectral Radiance (NESR) is evaluated for some "typical cases" depending on detector temperature end exposure time (personal communication). An equivalent source having a radiance equal to the NESR gives a signal equal to the noise; in other words, a SNR of 1. Figure 5.18 shows typical NESR for a 0.3 s exposure for two temperatures of the detector, which are typical conditions for nadir observations. The mean value is about 10^{-3}. As a consequence a best fit was accepted as valid if $\gamma \leq 10^{-3}\ W/m^2 \mu m\ sr$. Otherwise, the fit was rejected and it is assumed that the synthetic database was not representative of the observation (Figure 5.19). Such a procedure reduced the number of bins which could be accurately described with the current simulated radiance database to 3460. The discarded bins are the 7.4% and mainly grouped in few days rather than distributed all over the sample, so they could be associated to particular cloud and atmospheric conditions not assumed within the database.

The results of this simple model show that the reference assumptions on clouds are almost ever far from describing the observations. Ratios between the γ parameters calculated for the best fit of each bin and the reference model reveal a gain ($1 - \gamma_{bin}/\gamma_{ref}$, Figure 5.20) greater than 50% for the majority of the bins, with a maximum of 97.5%, and never lower than 39% when the discarded bins are not considered (they would have a minimum gain of 16.5% anyway), hence an evident improvement in clouds representation was obtained.
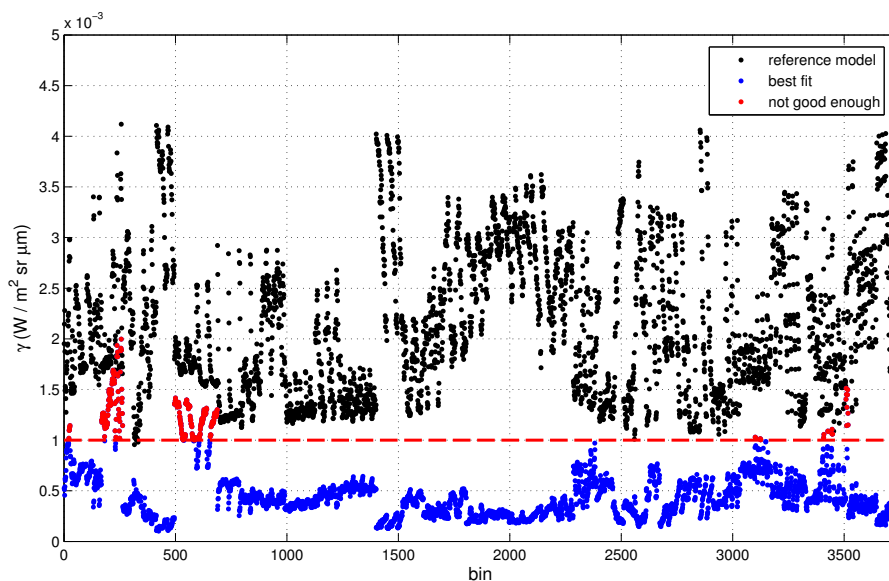
Figure 5.19: Root mean square γ calculated with the reference model (black dots) and the best fit model (blue dots). Fits producing a $\gamma \geq 10^{-3}$ are assumed not enough accurate and they are rejected (red dots). Each dot represent a bin, ordered from the first to the last day of VIRTIS observation.
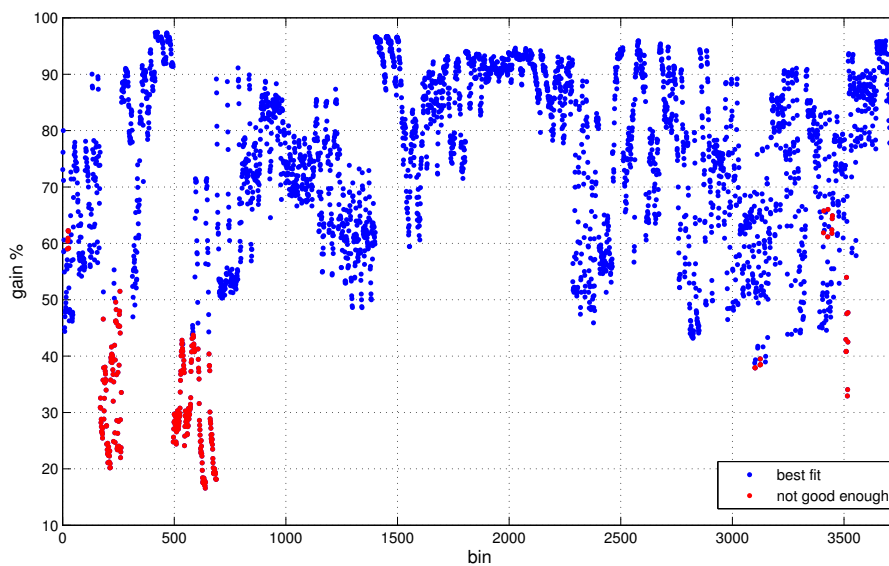
Figure 5.20: Gain percentage $(1 - \gamma_{bin}/\gamma_{ref})$ describing bin's averaged radiance with the best fit spectrum rather than the reference one. Red dots are bins rejected because the value of γ is larger than the assumed threshold value.
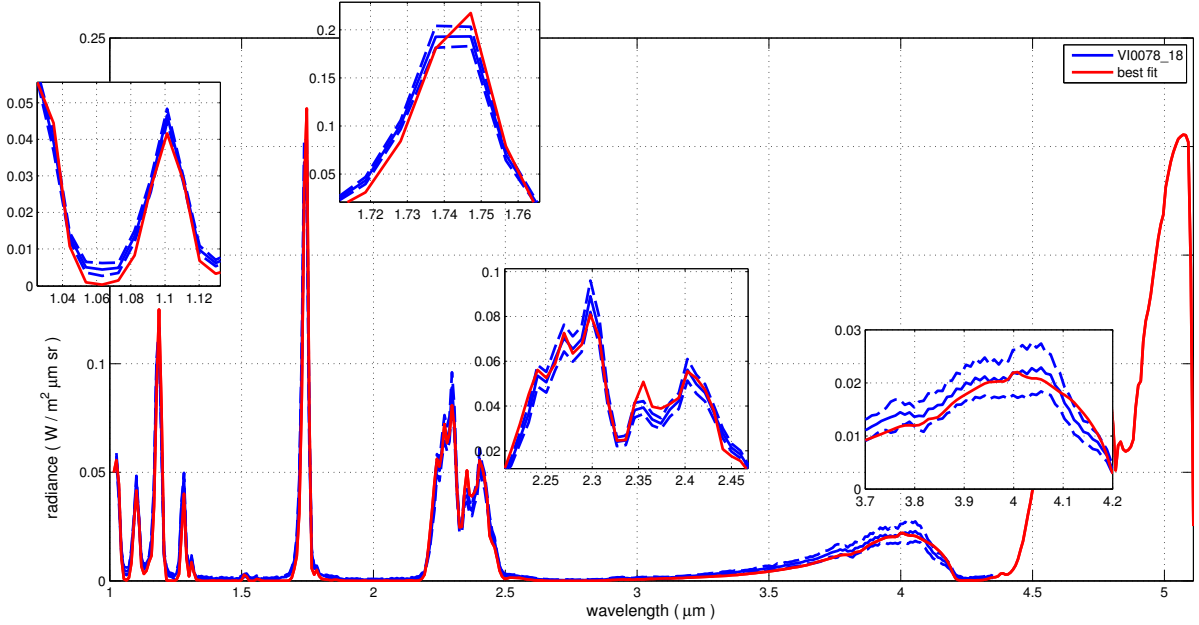
Figure 5.21: Best fit spectrum for 19 averaged spectra of the cube VI0078_18 (08/07/2006). Broken lines are plotted at three standard deviations from the mean. Bin edges: lon. 232.164-232.276° E, lat. 38.2039-38.3903° N. Best fit model: 75%/96% H_2SO_4, r_1=0.5, r_2=0.8, $r_{2'}$=1.8, r_3=3.65, f_1=0.2, f_2=1.8, $f_{2',3}$=0.8, VIRA 45.

5.5   Results analysis

It was noticed that describing the clouds with the same sulphuric acid concentration at every altitude made it difficult to fit the whole VIRTIS spectrum. In particular, with the assumption that the sulphuric acid concentration does not vary along the vertical extent of the clouds layers did not allow to fit with sufficient accuracy at the same time the 1.74 μm peak (which has high standard deviation and hence high weight in the best fit criterion) and the other radiance features observed in the data in other spectral windows (results are not shown here). Assuming different H_2SO_4 concentrations in the cloud layers significantly improved the fit quality. In particular the 1.74 μm window fit was improved and an excellent fit of the spectrum at every wavelength was obtained in most of the cases. An example of best fit spectrum is shown in Figure 5.21 for a bin of the cube VI0078_18. Best fits all over the sample show a result that is in contrast with the generally assumed value of 75% H_2SO_4 solution for the whole cloud layer that is extensively used in literature (Pollack et al., 1993; Zasova et al., 2007; Grassi et al., 2008; Tsang et al., 2008; Bézard et al., 2011; Haus et al., 2014). None of the bins was, in fact, fitted by a synthetic simulation with such an hypothesis (Figure 5.22). Not only the 75% case but also the pure 84% case has no correspondence with the observations (except for only two cases), and about 8% of the bins were fitted by a mixed cloud 75%/84%.
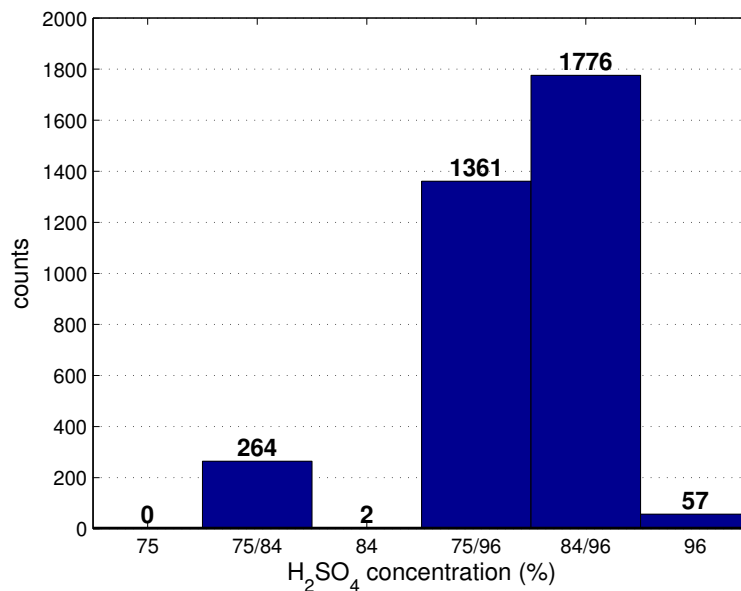
Figure 5.22: Counts of the sulphuric acid concentrations retrieved for every bin of the sample. Double values in abscissa refer to the upper cloud and the lower cloud respectively.
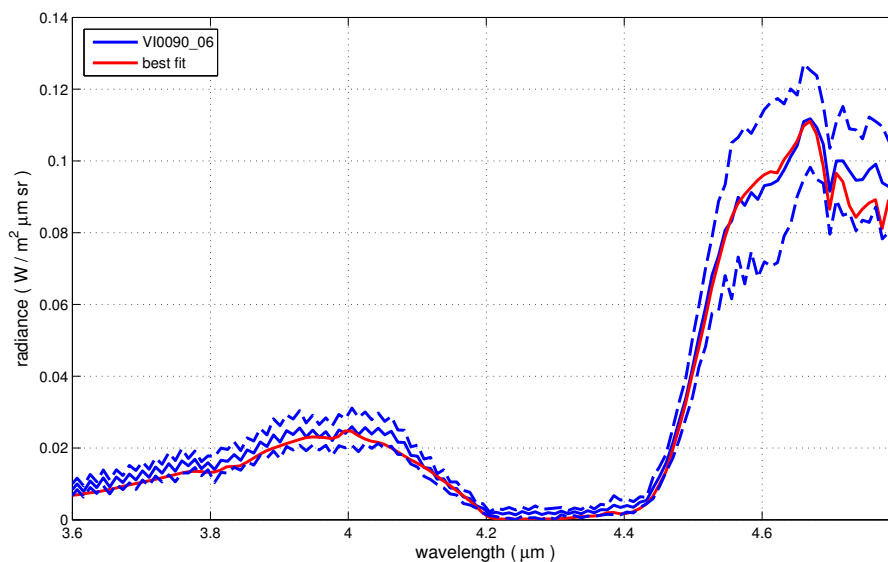
Figure 5.23: Best fit spectrum for 16 averaged spectra of the cube VI0090_06 (20/07/2006). Broken lines are plotted at three standard deviations from the mean. Bin edges: lon. 249.780-249.966° E, lat. 35.8163-35.9906° N. Best fit model: 75%/96% H_2SO_4, r_1=0.5, r_2=0.6, $r_{2'}$=1.4, r_3=2.80, f_1=1.4, f_2=2.0, $f_{2',3}$=1.0, VIRA 30.
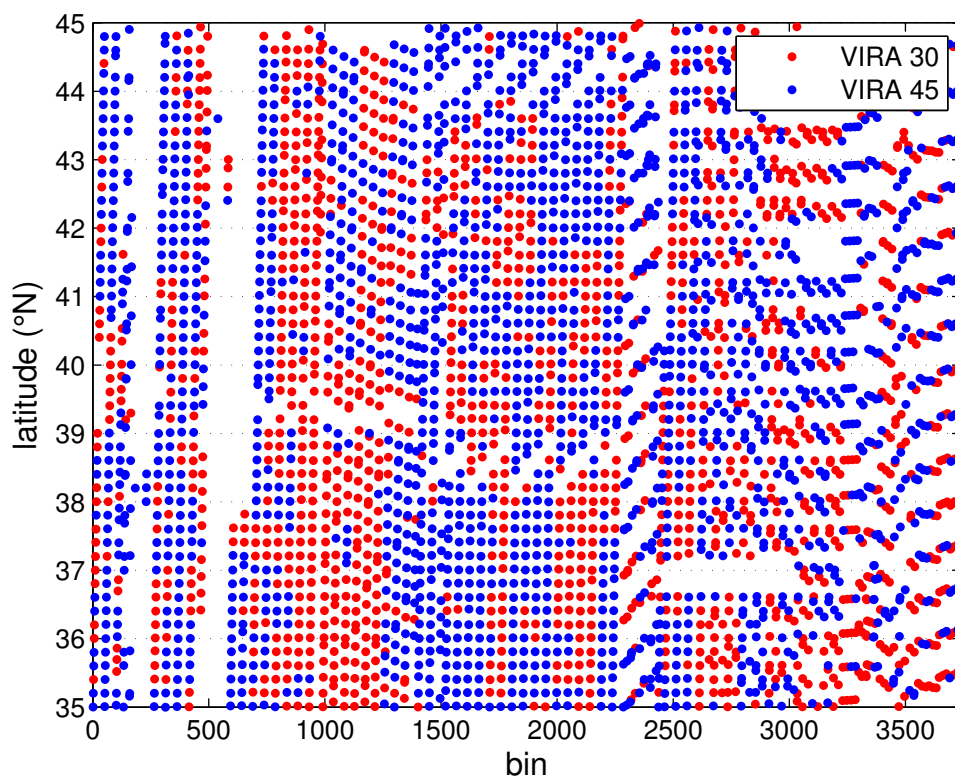
Figure 5.24: Distribution over latitude of the retrieved VIRA profiles. The two profiles are almost equally distributed and no geographical dependence arises.

Therefore, the usual assumption of relatively low concentration (75%) is rejected by our analysis. On the contrary, the hypothesis of a stratified cloud with high acid concentration in the bottom layer, up to 96%, is supported (92% of the instances). In particular, the 84%/96% combination results in more than half of the observations. Using the stratified cloud also allowed to adequately fit the left side of the 4.3 µm band (Figure 5.23) which is known to be problematic when the 75% concentration is assumed in the model (Grassi et al., 2014). Pure 96% models represent only a little percentage of the retrieved sample but they are not negligible and outnumber the frequency of conditions with lower uniform concentrations.

The two atmospheric profiles VIRA 30 and VIRA 45 used to model gas absorption are distributed through the sample without an evident latitude separation (Figure 5.24). The differences between the two profiles are too small compared to aerosols effect on radiance, as stated at section 5.3.5. For this reason a pressure-temperature retrieval should be done with a different methodology and for each bin separately.

Figure 5.25, left column, shows counts of the retrieved aerosols modal radii for the four modes all over the sample. It is noticed that modes 2 and 2' have the best accordance with the reference model of Pollack et al. (1993). The main value of the histogram is $0.8\,\mu m$ and $1.4\,\mu m$ respectively, to be compared to modal radii of $1.0\,\mu m$ and $1.4\,\mu m$ of the reference model, hence very similar. Mode 3, whose characteristics are still highly debated, has largest number of counts for the modal radius of $2.8\,\mu m$, hence for particles 55% smaller in volume than those assumed in the reference literature model. Nevertheless the reference model of $3.65\,\mu m$ fits well the observations for a significant percentage of the retrieved cases.

Differences larger than expected are observed for the mode 1: the largest part of the bins are fitted by particles with assumed modal radius equal to $0.5\,\mu m$. It is to note that the radiance sensitivity to mode 1 is the lowest with respect to other modes. Nevertheless, it is found that mode 1 particle number density is reduced in many cases, by a scale factor of about 0.2 with respect to the reference model (Figure 5.25, right column).

Mode 2 scale factor is very variable all over the considered range, without any predominant value, even though the most common instances are 0.8 and 1 and the reference model is an adequate representation for this parameter for that analysed cases. Modes 2' and 3 are instead multiplied by a higher number density to fit the observations, about the 30% more. This is similar to results obtained by Haus et al. (2013) (who defined the initial cloud model adopted in section 4.1), who retrieved a mode 3 scale factor of 1.5-1.6.

To verify the presence of possible correlations between the tested parameters of Table 5.1, Spearman's rank correlation coefficients were calculated. None of the possible combinations showed any evident correlation and so the parameters can be considered independent.
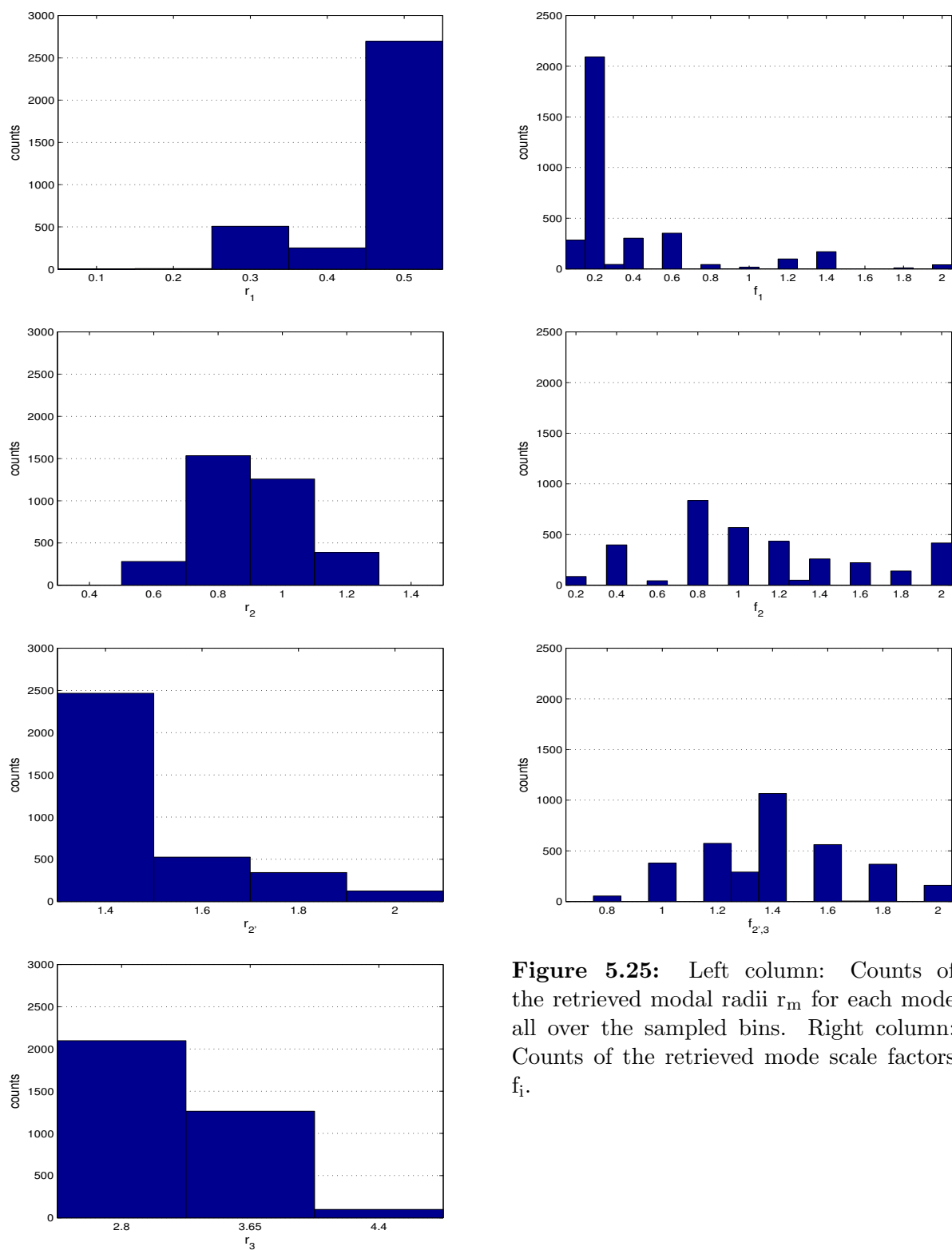
Figure 5.25: Left column: Counts of the retrieved modal radii r_m for each mode all over the sampled bins. Right column: Counts of the retrieved mode scale factors f_i.

Chapter 6

Upper haze properties from limb observations

Changing the observation geometry of VIRTIS from nadir to limb viewing angles, it is expected that intensity and shape of the spectrum gradually change from the typical nadir case, in which features of the surface or low atmosphere are observed and gases contribution is mainly absorptive, to a spectrum dominated by gaseous emission in the upper, optically thin, atmospheric layers. VIRTIS observations at limb show instead the same typical features of nadir observations even at altitudes as high as 85 km, well above the clouds top, where they look like scaled downward-looking spectra, with clearly visible surface features at short wavelength (Figure 6.1). The main difference with nadir spectra is observed at 1.27 μm and is related to the oxygen emission, that will be discussed in section 6.2. A physical explanation for these limb spectra is that thermal radiation from below is scattered into the line-of-sight by hazes or cloud particles at high altitude. These kind of spectral features wouldn't be observed if aerosols would not be present above clouds top (70 km about) and the only contribution was from gases.

Since the atmosphere of Venus at high altitude (higher than about 80 km) is optically thin, its contribution to the nadir measured radiance is small as seen in section 5.3.6. Therefore, it's almost impossible to retrieve the aerosol properties of those layers by nadir observations because the signal is dominated by the lower atmosphere's properties, from clouds tops to the surface. On the contrary, limb observations strongly depend on the presence of the upper hazes and by their physical features. Also the radiance from below has a significant contribution since it is scattered into the limb line-of-sight and dominates over the radiance directly emitted from the upper layer.

To study the upper layer of hazes by limb observation during the night a new methodology is proposed that exploit the nadir observations to accurately describe the signal exiting from the low-middle part of the atmosphere and from cloud layers. The main steps of the method are:
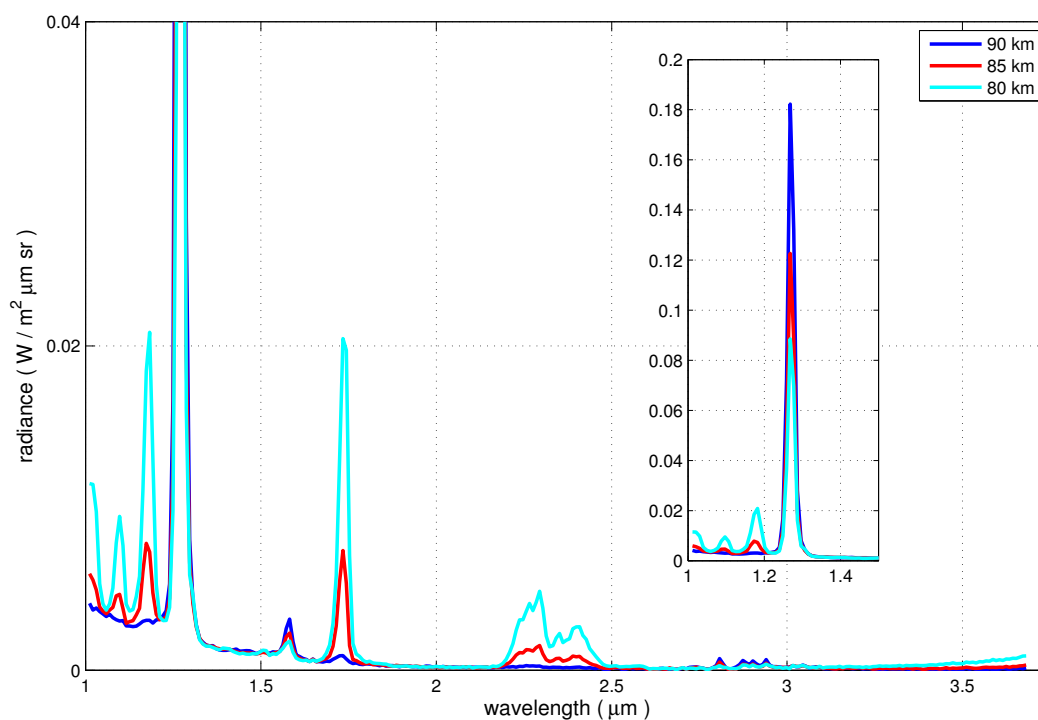
Figure 6.1: Example of limb observations above the main cloud deck for the cube VI0901_04 (08/10/2008). Typical nadir looking features are clearly visible even at high tangent altitude (given in the legend). The inset plot shows a focus of the high emission peak of oxygen airglow (1.27 µm).

1. Retrieve and define the atmospheric status for each nadir observation by using the best fit retrieval described in the previous chapter

2. Co-locate nadir observations with limb observations

3. Use the retrieved atmospheric and cloud parameters to compute the radiance expected at limb for selected data

4. Perform a comparison between simulated nighttime limb radiances and VIRTIS observations

5. Estimate the amount and properties of the upper haze layers

The nadir component has been already analysed in Chapter 5. In this Chapter the limb observations of the VIRTIS-M IR archive are analysed.

6.1 Data selection

As for the nadir data selection, research of limb looking observations into VIRTIS-M IR archive was limited to the northern hemisphere in nocturnal conditions. Limb cubes were chosen with a tangent altitude between 40 and 100 km, the lower limit of the clouds and the upper limit of the modelled atmosphere respectively. These conditions reduce the dataset from the available 4537 cubes to 903 cubes. Since limb data should be co-located with nadir observations, cubes within the same orbits of the nadir ones were selected, reducing to only 94 cubes in 49 different orbits. As a general rule, one cube per orbit is recorded but it is not uncommon that more than one cube is defined if conditions of observation change significantly during the orbit. To note that each nadir cube analysed in the previous chapter belongs to a single orbit.

The spatial co-location methodology requires that the tangent point of the limb observation falls within the atmospheric column observed with the nadir viewing configuration. Since the limb and nadir observations are not performed at the same time, a time lapse should be accounted for. That implies a dynamical evolution of the system. The dynamical evolution of the air column observed at nadir cannot be forecasted since a global atmospheric model of Venus' atmosphere is not available. At this regard, a simplistic assumption is made that accounts for an average rotation of the Venus air masses. In fact, Venus' atmosphere super-rotate from east to west at about 100 m/s at 60 km altitude, that is about the middle cloud deck altitude (Yamamoto and Takahashi, 2003; Moissl, 2008). This value is accounted for to find the final co-location. The times of nadir and limb observations were compared to approximately evaluate the longitudinal shift $\Delta\phi$ of the clouds between the two series of observations (limb and nadir) and to establish which cubes to account for. The meridional motion is slow and it was neglected during the co-location procedure.

$$\Delta\phi = \frac{\Delta t\ V}{R\cos\theta} \tag{6.1}$$

where Δt is the time shift, in seconds, between nadir and limb observations, $V \approx 0.1$ km/s is the speed of the clouds due to super-rotation, $R = 6051.8$ km is Venus' mean radius and θ is the latitude.

Only 39 cubes in 23 different orbits, all over the northern hemisphere, throughout the 5 years mission, satisfied this requirement. Many of them had a time shift too long (more than 13 hours) so they were rejected. Within the latitude band from 35° N to 45° N, 10 cubes in 5 orbits had the necessary requirements and so only a very small sample was available for this kind of analysis. Selected cubes are given in Table 6.1 and represent the best compromise, all over the VIRTIS archive, between time shift (a maximum value of about 40 minutes was assumed) and number of available observations (some other orbits satisfy the requirements in different latitude bands but have less than 10 useful observations).

Table 6.1: Cubes selected for nadir-limb comparison

Nadir	Limb	Date
VI0901_03	$\dfrac{\text{VI0901\_04}}{\text{VI0901\_05}}$	08/10/2008
VI0905_03	$\dfrac{\text{VI0905\_04}}{\text{VI0905\_05}}$	12/10/2008
VI0907_03	$\dfrac{\text{VI0907\_04}}{\text{VI0907\_05}}$	14/10/2008
VI0914_03	$\dfrac{\text{VI0914\_04}}{\text{VI0914\_05}}$	21/10/2008
VI0916_03	$\dfrac{\text{VI0916\_04}}{\text{VI0916\_05}}$	23/10/2008
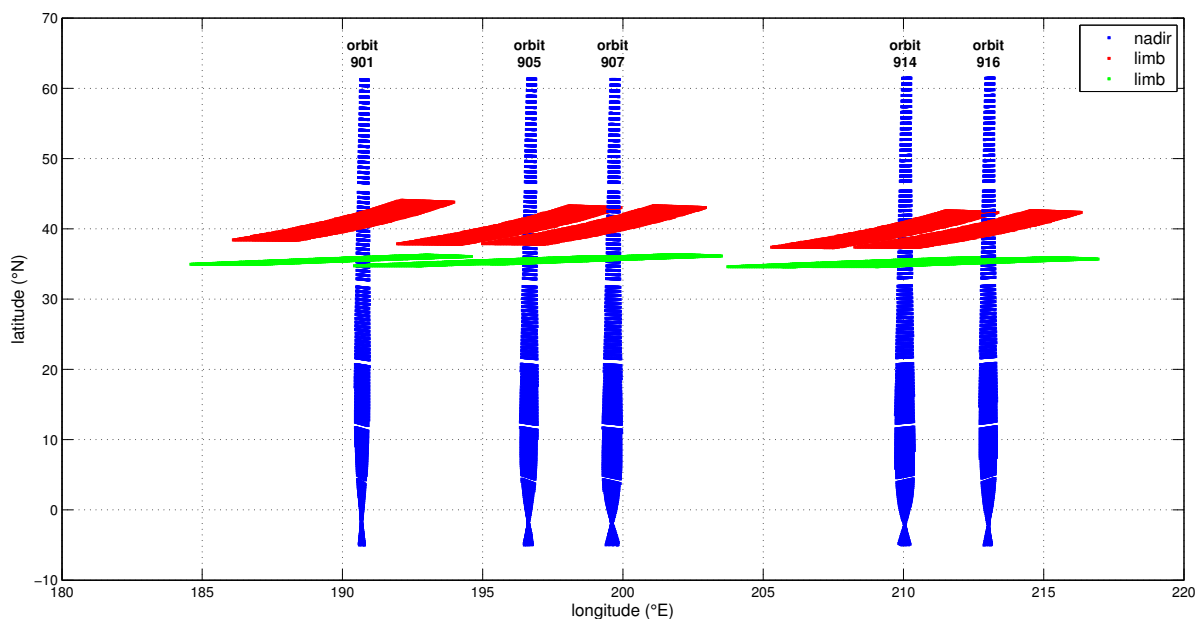
Figure 6.2: Geographic location of the 5 analysed nadir cubes (blue) and the 10 corresponding limb cubes (red and green). Each dot represent an observation (a complete spectrum). The orbit number is shown in the upper part.
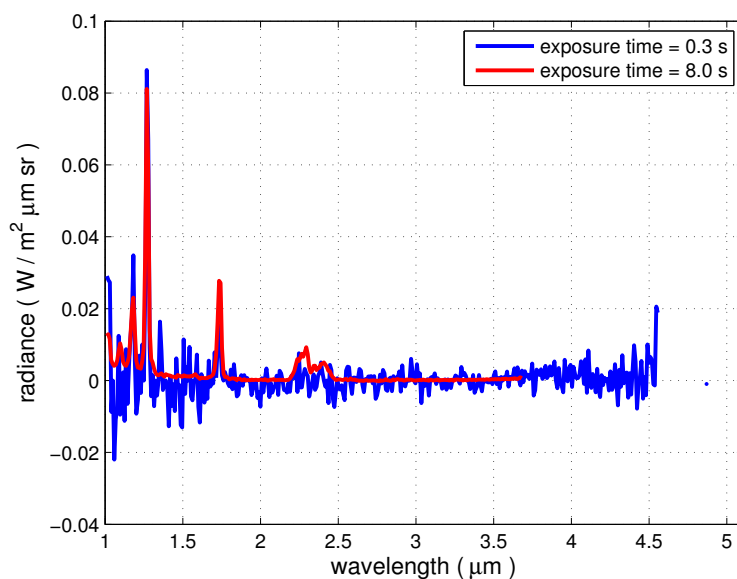
Figure 6.3: Limb spectra for two different exposure times. Both the spectra are observed at 80 km altitude. They refer to cubes VI0901_05 (blue line) and VI0901_04 (red line).
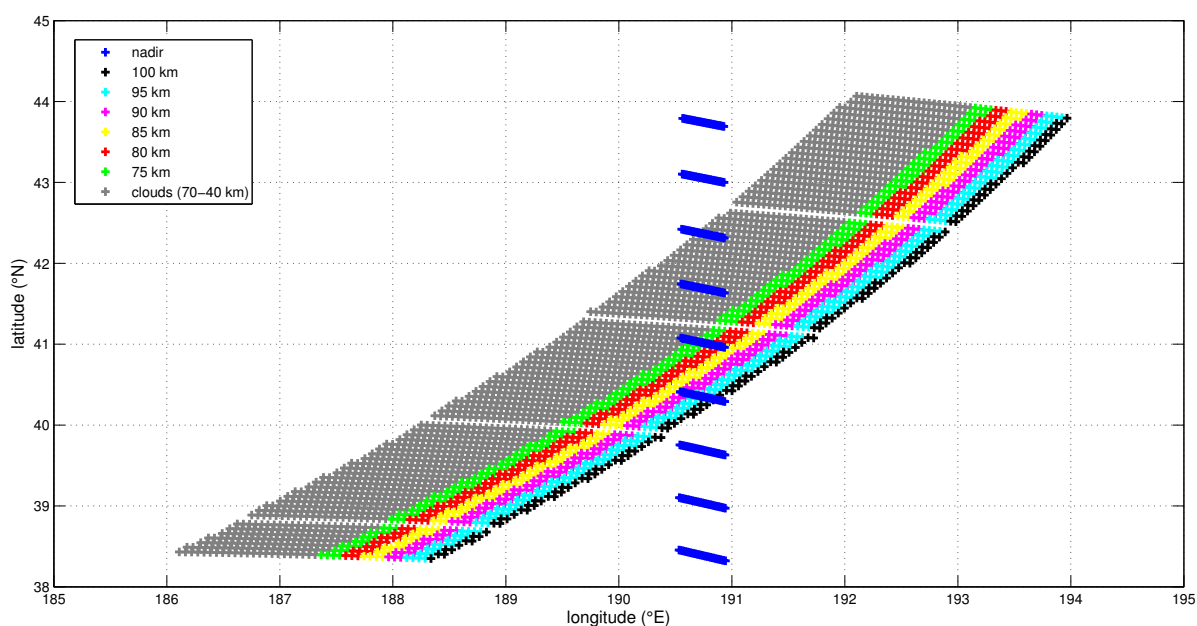
Figure 6.4: Altitude band sampling for the cube VI0901_04 (08/10/2008). Each band is 5 km high and the mean tangent altitude is given in legend. The grey band is the main cloud deck and blue dots are the co-located nadir observations. Latitude sampling is done in order to collect each nadir set of observation (a blue "stripe") at the band centre. The other selected cubes have the same structure.

The 5 selected orbits are near together, both in time and in space, and they have a similar structure shown in Figure 6.2. The exposure time is the main difference between the limb cubes: northern cubes (the red ones in the figure) have a 8.0 s exposure whereas southern cubes (the green ones in the figure) have a 0.3 s exposure. Since the observed radiance is very small at high altitude, a short exposure time produce a spectrum with a low SNR and the atmospheric features are completely masked by noise, whereas a long exposure time guarantees a clear spectrum (Figure 6.3). Adequate analysis of short exposure data requires additional filtering methods not considered in the thesis work and so limb data analysis focuses only on the 5 sets with long exposure data.

The limb data were then divided into latitude bands corresponding to the nadir bins and divided into altitude bands of 5 km, that is about the pixel vertical resolution at the tangent point for the considered set of observations. 9 latitude bins per orbit were obtained for each altitude band (Figure 6.4). In the analysed cases, wind speed of 100 m/s shifts the clouds of about 3.5° westward. As a result, only the clouds at 38.5° N in Figure 6.4 could be effectively co-located with limb observations. It was assumed that no significant variations existed into each latitude band (at least for little longitude and time shifts as those assumed) so that all available data in the selected cubes were exploited in the analysis.

As in the nadir case, some wavelengths show evident outliers that were removed with Chauvenet's criterion, described in section 5.1.1. Finally, spectra were averaged inside each bin.

6.2   Oxygen airglow emission

Observing radiance at limb in the upper atmosphere of Venus a strong emission stands out at $1.27\,\mu m$ increasing with altitude, while at other wavelengths the radiance gradually decreases (Figure 6.5). This feature is due to the intense emission in the $a^1\Delta_g - X^3\Sigma_g^-$ airglow band of molecular oxygen (Bailey et al., 2008; Gérard et al., 2008; Piccioni et al., 2009). The airglow emission is thought to be the result of oxygen atoms formed by photodissociation and electron impact dissociation of CO_2 and CO on the dayside at wavelengths $\lesssim 200\,nm$. Oxygen atoms are then carried by the solar to anti-solar circulation in the upper atmosphere to the nightside where they can descend to higher density regions. Here the O atoms can recombine through three body or catalytic reactions to produce O_2 molecules in excited states whose lifetime is about 70 minutes, which then emit the airglow photons:

$$
\begin{aligned}
O + O + M &\longrightarrow O_2^* + M \\
O_2^* + M &\longrightarrow O_2 + M + h\nu
\end{aligned}
\tag{6.2}
$$
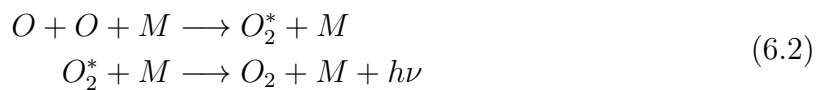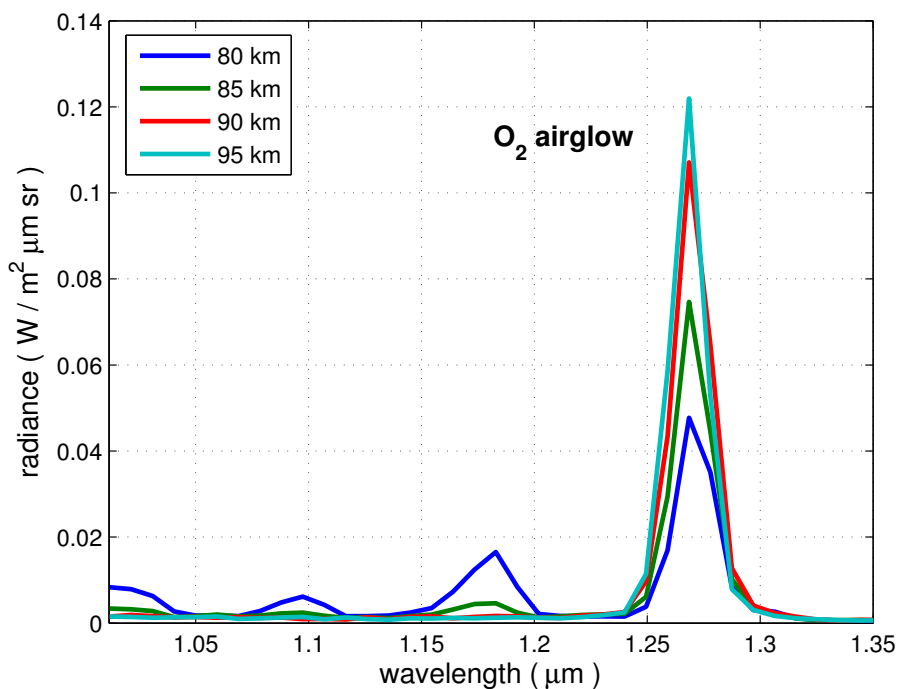
Figure 6.5: Oxygen airglow is clearly visible in VIRTIS limb observations at $1.27\,\mu m$, growing with tangent altitude up to 95 km. The observations refer to the cube VI0914_04 at the tangent altitudes given in legend.

where M = CO_2 or N_2. Airglow emission is highly variable from day to day and shows variations on time scales as short as one hour. The location of the O_2 airglow emission is constrained by the requirement that the atmospheric density must be high enough for the three body reactions needed to produce the excited O_2, but not so high that collisional quenching by CO_2 will dominate over radiative decay. These constraints resulted in chemical model predictions that the emission should occur at altitudes between 90 and 100 km. Observing the O_2 airglow in limb viewing geometry Drossart et al. (2007) show that the emission peaks at 96 ± 1 km with little emission above 100 km. A second oxygen airglow emission is also observed at $1.58\,\mu m$, but it is about one order of magnitude weaker than the main peak at $1.27\,\mu m$.

Such kind of emission needs a chemical diffusive model to be correctly described. Nevertheless, the process is highly variable to be modelled in accurate way and it is highly variable for each observed case. Therefore, oxygen airglow was not parametrized in the presented model and the peak never appears in the synthetic spectra, that is the 1.27 and $1.58\,\mu m$ wavelengths were ignored for the comparisons of simulations with observations.
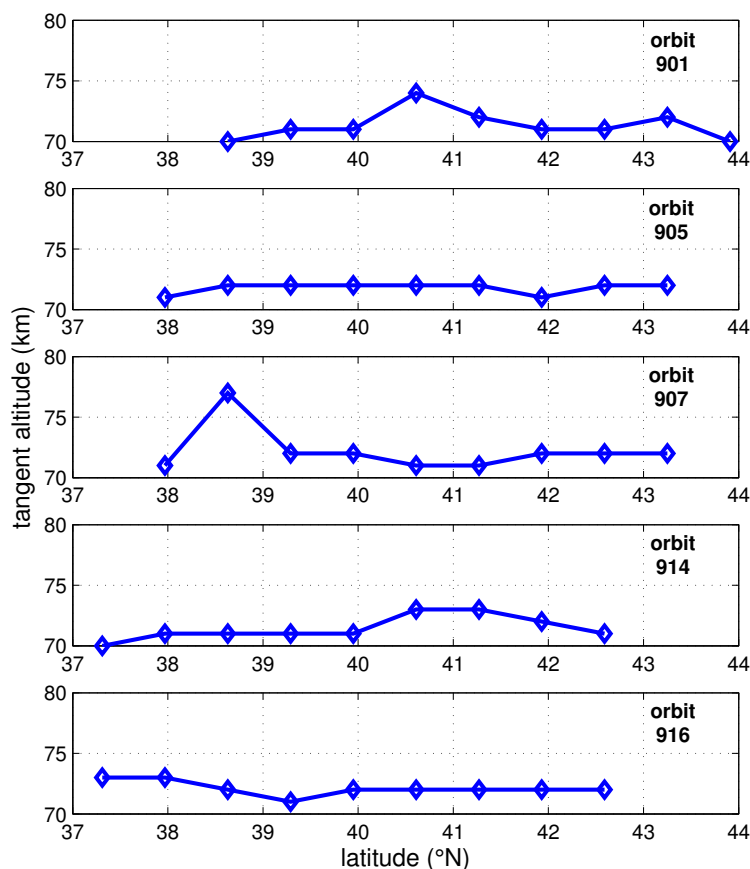
Figure 6.6: Clouds top for the five selected orbits (given in each subplot), retrieved with the best fit technique on VIRTIS nadir data.

6.3   Data analysis

Increasing the tangent altitude while crossing the main cloud deck, from about 40 to 70 km, has only little influence on the outgoing observed radiance because the line-of-sight of VIRTIS intercepts the clouds top (defined as the layer where the cloud optical depth approaches unity) so the main contribution to the observation comes from that altitude. The clouds top, which was retrieved with the best fit model in the previous chapter, is observed between 70 and 73 km for all the bins, with the exception of one bin of the cube VI0907_03 where a higher cloud is retrieved, up to 77 km (Figure 6.6). Above the cloud top the emitted radiance gradually decreases until the typical surface features of the spectrum completely disappear just as the scattering hazes disappear. Figure 6.7 shows a vertical scan of the atmosphere for the cube VI0905_04, from 40 to 100 km: the typical nadir features (superimposed in the figure from the same orbit) are clearly visible up to about 87 km, that is recognised as the limit of the upper hazes.
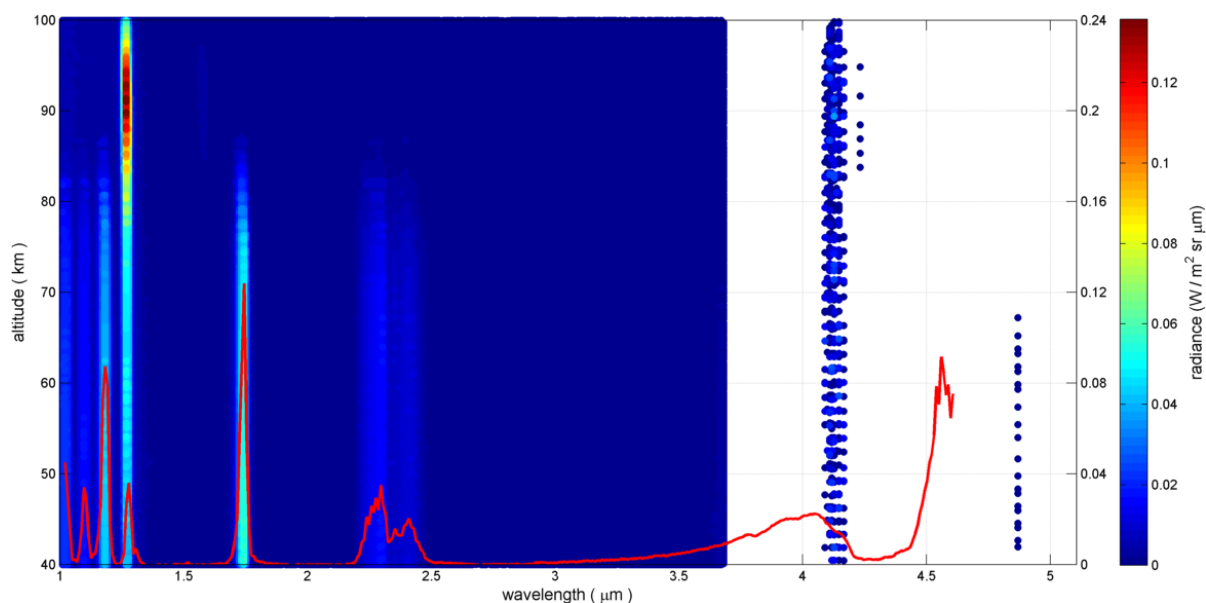
Figure 6.7: Radiance observed at limb depending on the tangent altitude (color scale plot) for the cube VI0905_04 (12/10/2008). Oxygen airglow emission peak is clearly visible at 1.27 μm at about 90 km. The superimposed red curve is a nadir spectra for the same orbit (cube VI0905_03, radiance scale on the right side).

The oxygen airglow at 1.27 μm dominates the spectra beyond 75 km with a maximum at 91 km and also the second weak oxygen emission at 1.58 μm is visible from 85 to 97 km. Unfortunately, the long exposure time of the selected cubes (8 seconds) saturates the detector above 3.65 μm so an important part of the data is missing.

The comparison between the VIRTIS observations of the five orbits at nadir (Figure 6.8) and at limb above the clouds top (Figure 6.9), averaged inside the bins previously considered, confirms that limb spectra mainly reproduce the upward radiance that is scattered by the layer rather than the emission of the layer himself. In fact, barring the decreasing order of magnitude with altitude and the oxygen peak, radiances have the same behaviour in corresponding cases. At 90 km only a very low feature at 1.73 μm is left, which completely disappears at 95 km, while the O_2 features dominate the spectra.

Some noise always affect the observations both at nadir and at limb, as discussed in section 5.4, but it clearly emerged only at limb, where radiances are lower. The noise in data is evident at short wavelengths where the "bottom" of the spectra gradually rises above zero. Since the comparison between limb spectra was not impeded by such a noise it was preferred to handle the original data without any approximate correction.

Figure 6.8: Nadir spectra for the five selected orbits (given in each subplot), averaged in the nine selected latitude bands; the spectra often superimpose each other.

6.4   Monte Carlo limb model: MYSTIC

Limb spectra depend on the upward radiance (that in turn is weakly dependent on the uppermost layers) and on the scattering particles at the tangent altitude. Given the limb geometry a different model is needed, able to simulate limb spectra and retrieve upper haze properties. In fact, due to the plane-parallel approximation, the CDISORT solver used in nadir geometry is not able to perform computation of radiance scattered at limb because the horizontal extension of the layers is assumed as infinite. For this reason a spherical geometry is required, together with an appropriate solver able to compute the radiative transfer with this assumptions. The radiative transfer equation in spherical geometry, in nocturnal conditions, becomes:
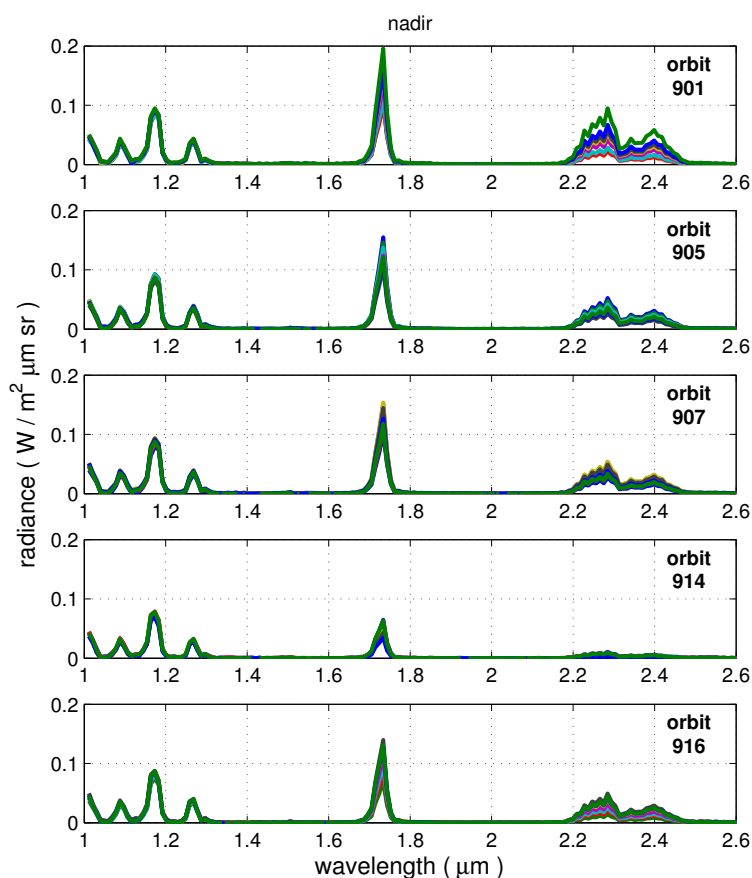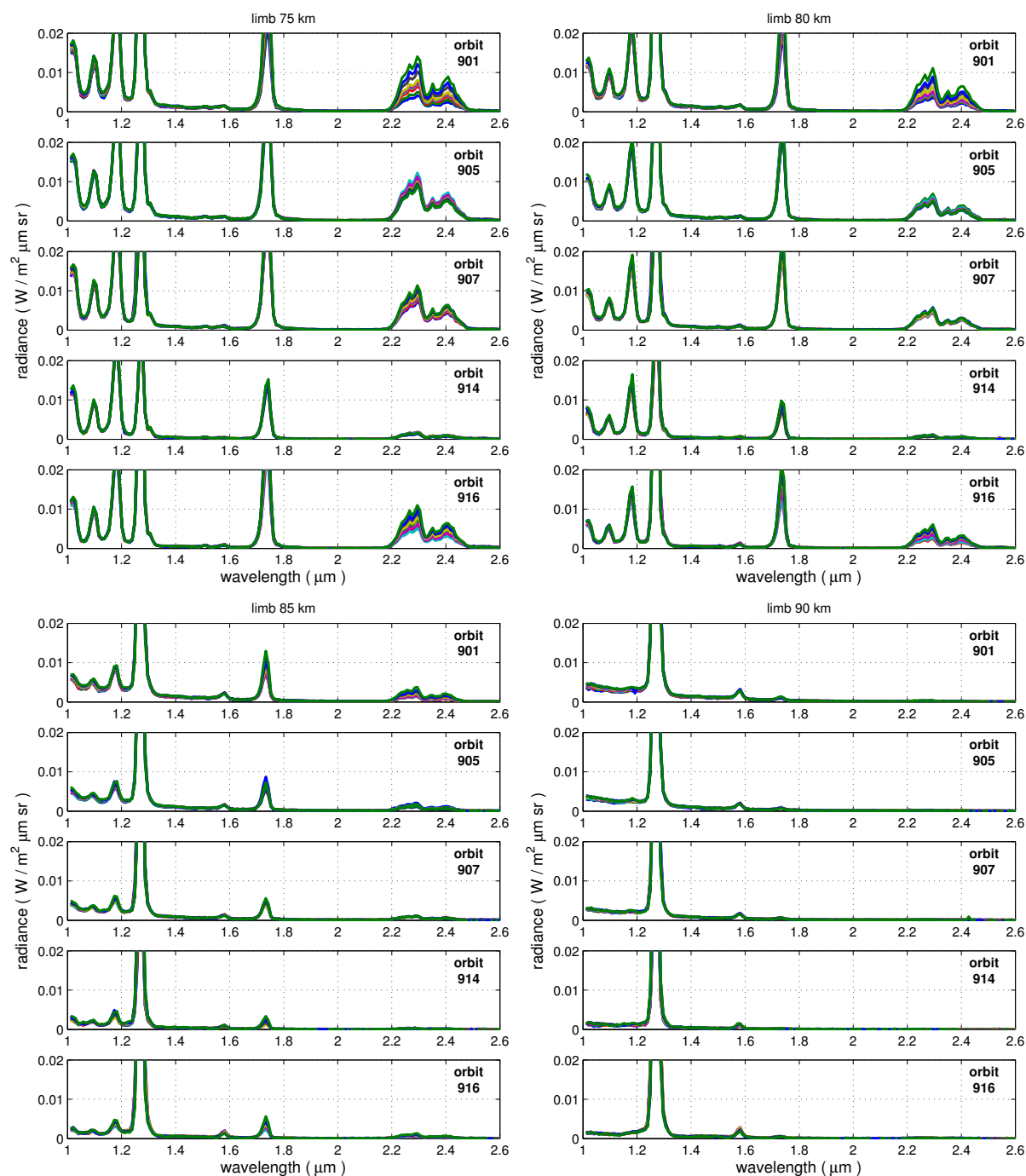
Figure 6.9: Limb spectra for the five selected orbits (given in each subplot), averaged in the nine selected latitude bands (9 curves per subplot) and in the 5 km altitude band given on each lot top.

$$-\frac{(\hat{n} \cdot \nabla)I(r,\mu,\phi)}{k_e(r)} = \quad I(r,\mu,\phi) +$$

$$-\frac{\tilde{\omega}(r)}{4\pi} \int_0^{2\pi} \int_{-1}^1 P(r,\mu,\phi;\mu',\phi')\, I(r,\mu',\phi')\, \mathrm{d}\phi' \mathrm{d}\mu' + \tag{6.3}$$

$$- (1 - \tilde{\omega}(r))B[T(r)]$$

that is similar to the equation (5.1) for the plane-parallel geometry but where the layer height z has been changed with the distance r of the spherical geometry and the streaming term $\hat{n} \cdot \nabla$, in a spherical symmetric atmosphere (spherical shells), is defined as:

$$\hat{n} \cdot \nabla = \mu\frac{\partial}{\partial r} + \frac{1 - \mu^2}{r}\frac{\partial}{\partial \mu} \tag{6.4}$$

A Monte Carlo model is the most straightforward way to calculate radiative transfer because it performs a physically correct tracing of photons even in a cloudy atmosphere and also with polarization if needed. For this reason, the Monte Carlo method is often chosen for applications where spherical geometry plays a role. The libRadtran package includes a Monte Carlo solver for radiative transfer called MYSTIC (Emde and Mayer, 2007; Mayer, 2009) that is able to perform backward tracing of thermally emitted photons in a 1D spherical atmosphere (also a fully 3D version exists but is not open access). The model inputs are the same described for the CDISORT model in the previous chapters such as, layer by layer, optical depth for gases, single scattering albedo, extinction coefficient and phase function for aerosols, pressure and temperature vertical profiles, surface albedo and geometry of observation; so the input files already defined for the nadir model were also used for the limb one. To define the geometry of the system, the viewing angle θ necessary to look at a specific tangent altitude h is calculated assuming a spherical atmosphere 100 km high (the TOA of the VIRA profiles, as for CDISORT) surrounding a spherical planet with radius R=6051.8 km:

$$\theta = \arcsin\left(\frac{R + h}{R + \mathrm{TOA}}\right) \tag{6.5}$$

This angle is then passed to the solver as the zenith angle of the outgoing radiance at TOA (Figure 6.10).

The cloud model that produced the best fit at nadir for each sampled bin was then reprocessed with MYSTIC in spherical geometry to verify if the spectra modelled at limb at different tangent altitudes are consistent with the observations.

The main parameter that affects a Monte Carlo solution is the number of traced photons. Few photons give an output radiance that is lower than "true" and an unstable solution. On the other hand, a large number of photons implies long computation time. To find the minimum number of photons necessary to have an accurate solution of
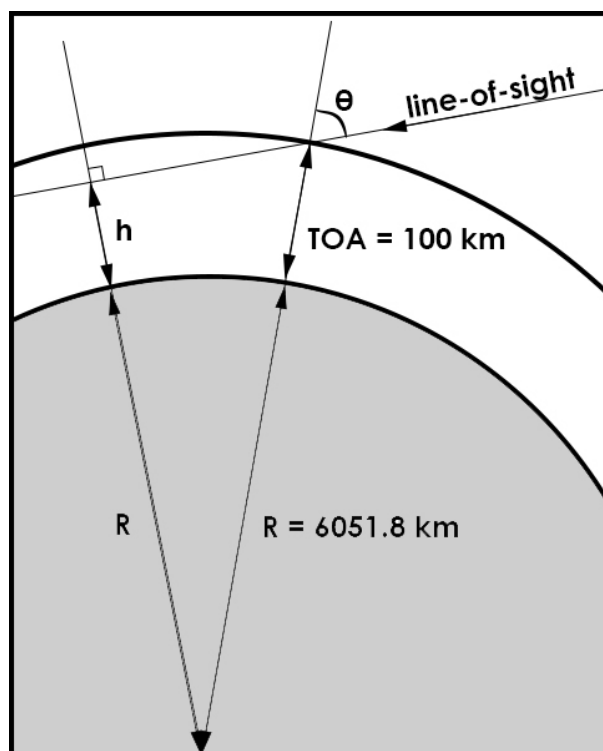
Figure 6.10: Geometry for limb observations at tangent altitude h.

the radiative transfer equations, the CDISORT solution at nadir was considered as the "truth" and a number of simulations also looking at nadir were performed with MYSTIC, for multiple numbers of photons. A compromise between effectiveness and computation speed is found for value of 10^8 photons. Such a number allows a MYSTIC result within the 1% from the CDISORT result (Figure 6.11).

6.5   Limb spectra analysis and comparison

The required number of photons to perform sufficiently accurate limb simulation does not allow a rapid computation of an entire single spectra even if parallel computing is exploited. In fact, computation times is of the order of hours even for very narrow spectral bands. For these reasons computations were restricted to one single band. The spectral interval around the 2.3 µm window was chosen to perform computations for some randomly selected observations. The above spectral band was selected considering that for large wavelengths VIRTIS data are missing and that the MYSTIC code does not allow computations in the emission/scattering configuration for wavelengths lower than 1.2 µm. Also the window around 1.73 µm was available but the 2.3 µm was preferred because it was a key window for nadir fit.
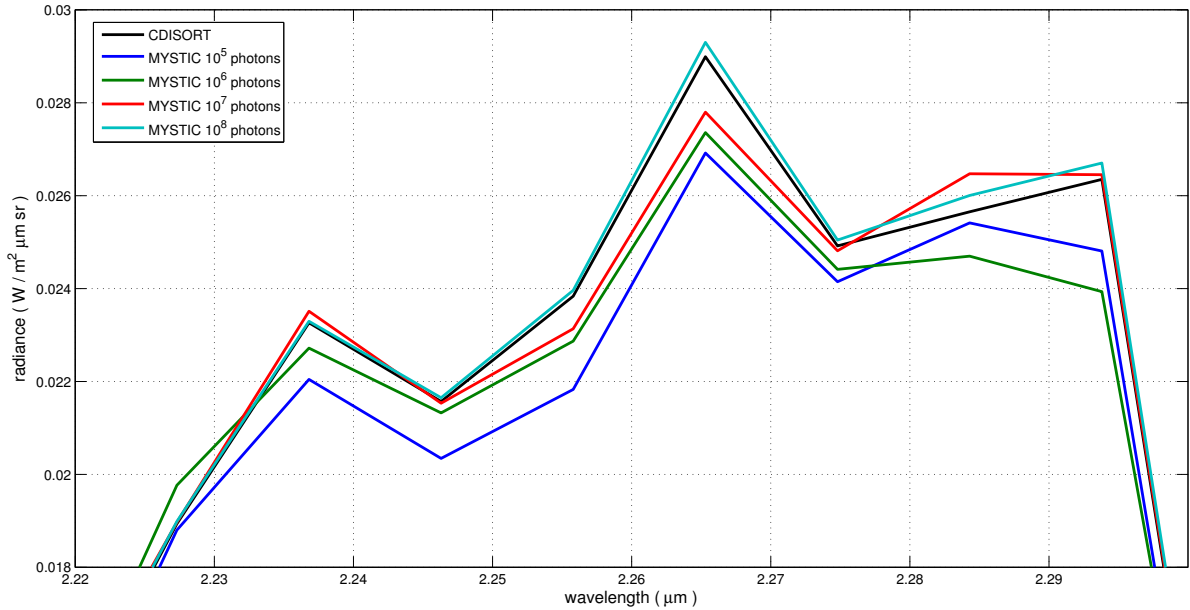
Figure 6.11: Comparison with nadir geometry between the CDISORT solver (plane-parallel) and the MYSTIC solver (Monte Carlo) with different number of traced photons.

The comparison between MYSTIC simulations and VIRTIS observations at 80 and 95 km shows that the synthetic spectra are at least three times higher in radiance units than the observations (Figure 6.12). Since the upward radiance is well described by the nadir model, the parameters which affect the limb spectra are the size and number of the upper haze particles, which is modelled with particles of modes 1 and 2 up to 86 km and of mode 1 alone from 86 to 100 km. At 95 km VIRTIS radiances drop to very low values comparable with the instrument noise level. For this reason we assume that no scattering particles are observed at this altitude. On the contrary, synthetic spectra were computed assuming a not negligible number of particles up to 100 km so they always show scaled nadir-like features, even when few small particles are considered, as in the case c) in Figure 6.12, that is zoomed in Figure 6.13. At 80 km both observations and models show the same features but the scattering is overestimated.

The computed radiances suggest that to fit the observations it is necessary to assume a smaller number density of the haze particles in the upper layers or to reduce their sizes. Small mode 1 particles are less efficient scatterer than mode 2 because both of them have a single scattering albedo close to 1 at 2.3 µm but mode 1 has a lower extinction cross section; Figure 6.14 shows extinction cross section and single scattering albedo for the four particle size distribution retrieved in the examples of Figure 6.12 (two different distributions for each mode, depending on modal radius) with a sulphuric acid solution of 75% (increasing acid concentration to 84% has only limited effects compared with changes in particles radii).
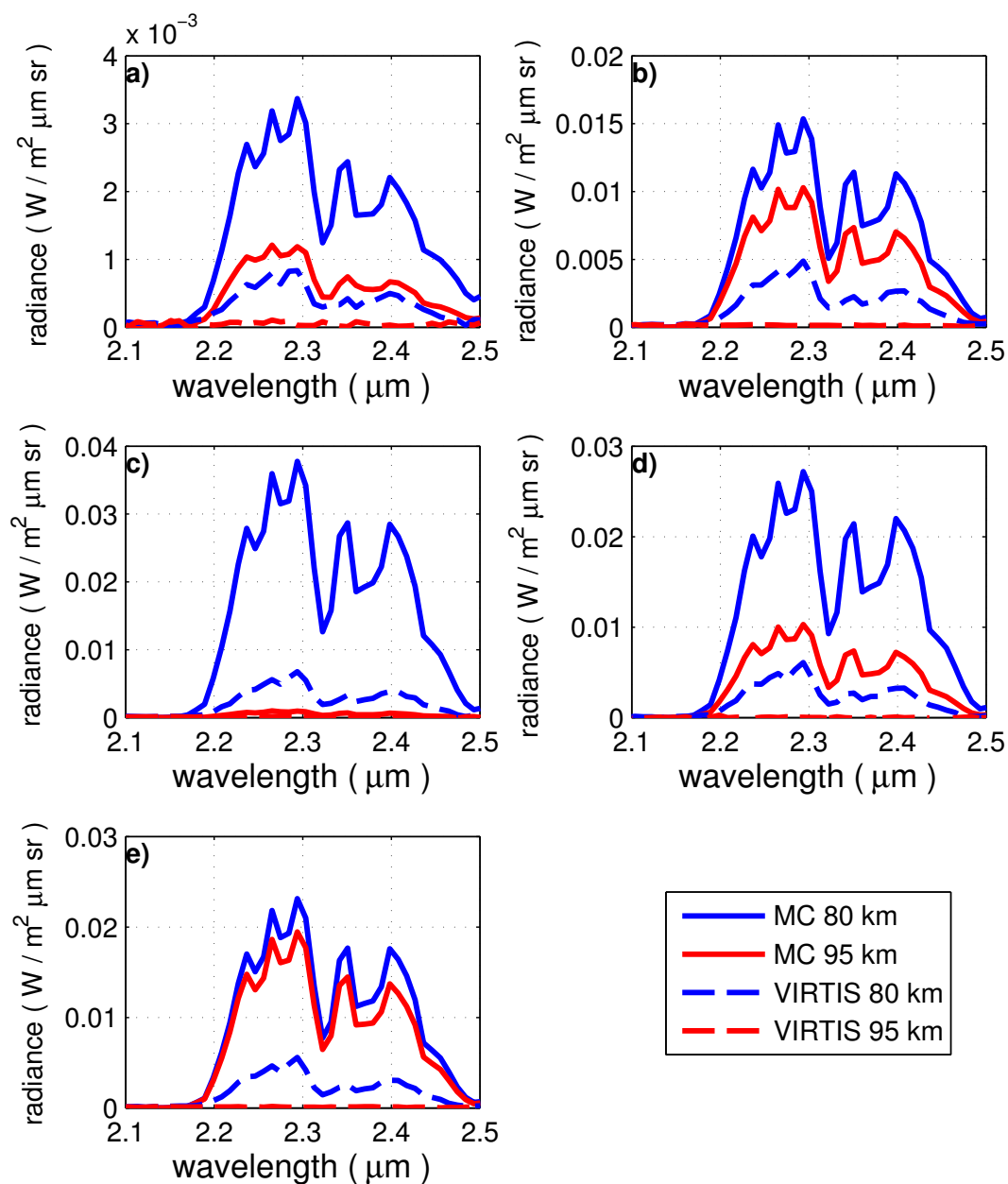
Figure 6.12: Comparison between limb observations (VIRTIS, broken lines) and synthetic spectra (Monte Carlo, solid lines) at 80 and 95 km. Parameters of modes 1 and 2:
a) 75% H_2SO_4, r_1=0.5, r_2=1.0, f_1=0.2, f_2=0.8. VIRA 30. Orbit 914, bin latitude 39.2° N.
b) 84% H_2SO_4, r_1=0.5, r_2=0.8, f_1=0.4, f_2=1.8. VIRA 30. Orbit 901, bin latitude 40.6° N.
c) 75% H_2SO_4, r_1=0.3, r_2=1.0, f_1=0.1, f_2=1.0. VIRA 45. Orbit 905, bin latitude 38.0° N.
d) 84% H_2SO_4, r_1=0.5, r_2=0.8, f_1=0.2, f_2=1.4. VIRA 45. Orbit 916, bin latitude 42.6° N.
e) 84% H_2SO_4, r_1=0.5, r_2=1.0, f_1=0.6, f_2=1.0. VIRA 45. Orbit 907, bin latitude 41.9° N.
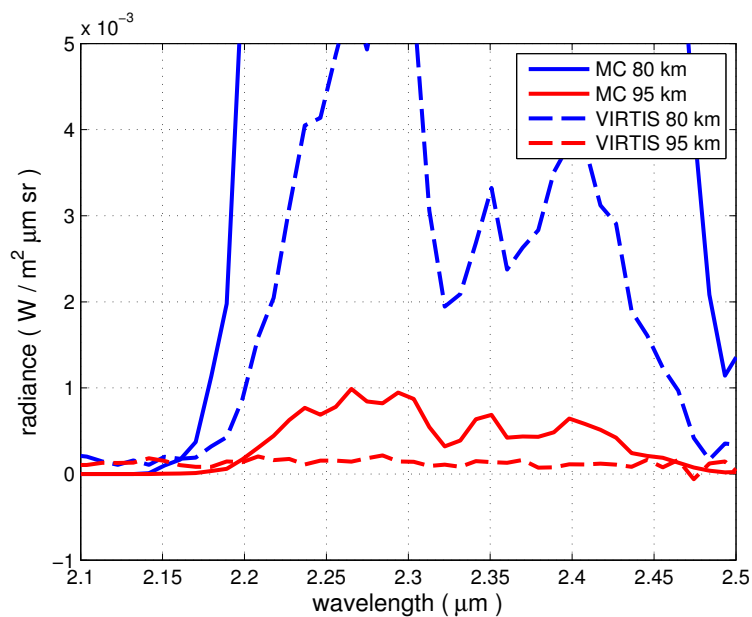
Figure 6.13: Zooming of the sub-figure c) of Figure 6.12. Even if the radiance is very low at 95 km, the Monte Carlo model always shows nadir-like features that are absent in the observations.
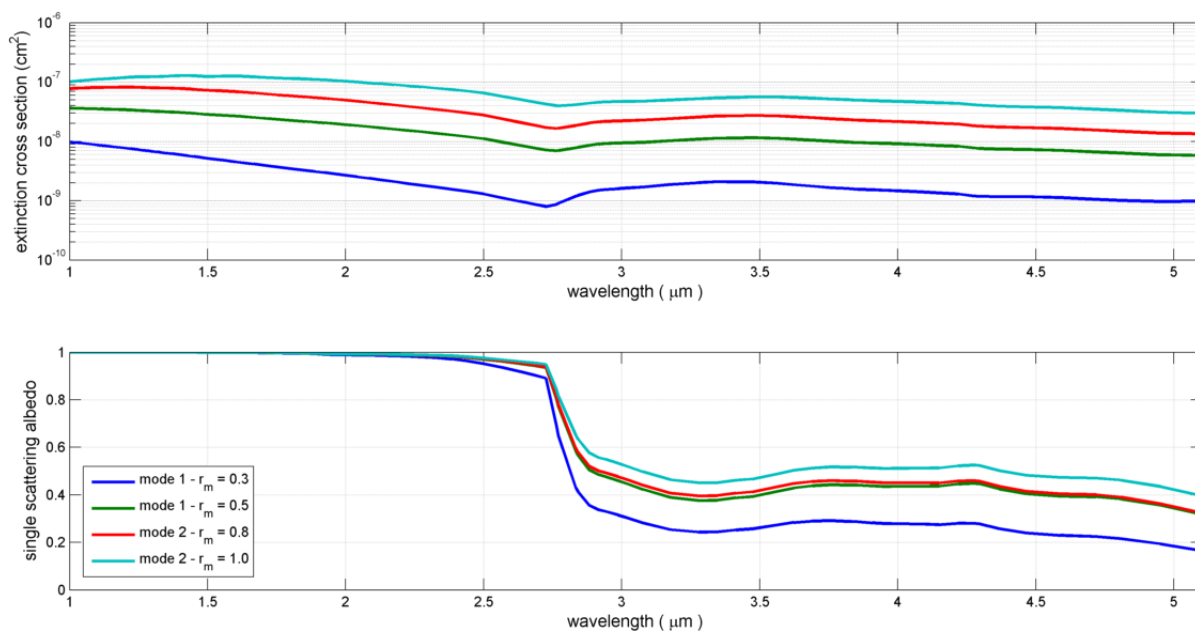
Figure 6.14: Extinction cross section (top) and single scattering albedo (bottom) for different particles modal radii of the modes 1 and 2.

Theoretical considerations shows that retrieving information about the particles size would benefit of the exploitation of the 4 µm window, since the single scattering albedoes of the considered modes are very sensitive to effective radius. Unfortunately VIRTIS data in the 4 µm window is saturated so this kind of analysis is not possible for the selected observations.

The present analysis was limited to a single window. From the obtained results the only consideration that can be drawn is that the upper haze layer has to be reduced in terms of thickness and particles number with respect to the assumptions of the model. In particular, the upper hazes observed by Wilquet et al. (2009) result inadequate to describe the analysed orbits since no scattering particles are observed in the data above 90 km altitude. The analysis of Wilquet et al. (2009) were performed on solar occultation data, so in diurnal conditions, but a gradual sinking of the high atmosphere during the night can be deduced by the oxygen emission (Gérard et al., 2008) and, as a consequence, a sinking of the hazes might happened. Another possible explanation is that the reduced amount of particles could be related with the reduced nocturnal production of sulphuric acid all over the layer, that is mainly a photochemical process. Even the intrinsic variability of Venus' atmosphere can be responsible for such changes in the observations within different orbits. The explanation might be a combination of the three hypothesis.

Chapter 7

Conclusions

VIRTIS-M IR archive span a long time interval, about 5 years long. A statistical analysis is performed on 59 orbits, containing nocturnal nadir observations in the latitude band between 35° N and 45° N. The observations are averaged into bins of 0.2° x 0.2° of longitude and latitude and a forward model is assembled to retrieve atmospheric and clouds properties for each bin. This required the computation of an extensive dataset of simulated spectra. The dataset is derived from modification of an initial reference model (defined from what accepted in literature): vertical profiles of temperature and pressure referred to the standard Venus International Reference Atmosphere (Seiff et al., 1985), VMR profiles of gases referred to Haus and Arnold (2010), clouds and hazes particle number density distributions referred to Haus et al. (2013) and Wilquet et al. (2009) respectively, clouds chemical composition and particle size distributions referred to Pollack et al. (1993). This reference model is then modified in its key parameters to obtain a series of configurations able to describe the variability of Venus' atmosphere.

The gain obtained from the fit process is evaluated with respect to a standard simulation.The mean difference between each VIRTIS spectrum and the synthetic one obtained with the reference model is always higher than the mean noise on VIRTIS data (10^{-3} $W/m^2\mu m$ sr). Therefore, the initial model is inadequate to describe the Venus' atmosphere. A best fit process is then implemented to establish the best configuration for each VIRTIS observation. The results show large improvements with respect the reference model and fit close to observation within the mean noise level.

Particle size distributions of clouds are usually considered fix in the models found in literature. In the present work slight variation of the modal radii are assumed as reasonable hypothesis due to physical or chemical processes. It is noticed that modes 2 and 2' have the best accordance with the reference model of Pollack et al. (1993). The main value of the retrieved modal radii is 0.8 µm and 1.4 µm respectively, to be compared to modal radii of 1.0 µm and 1.4 µm of the reference model, hence very similar. Mode 3, whose characteristics are still highly debated, has largest number of counts for the modal radius of 2.8 µm, hence for particles 55% smaller in volume than those assumed in the

reference literature model. Nevertheless the reference model of 3.65 μm fits well the observations for a significant percentage of the retrieved cases. Differences larger than expected are observed for the mode 1: the largest part of the bins are fitted by particles with assumed modal radius equal to 0.5 μm. It is to note that the radiance sensitivity to mode 1 is the lowest with respect to other modes. Nevertheless, it is found that mode 1 particle number density is reduced in many cases, by a scale factor of about 0.2 with respect to the reference model. Mode 2 scale factor is very variable all over the considered range, without any predominant value, even though the most common instances are 0.8 and 1 and the reference model is an adequate representation for this parameter for that analysed cases. Modes 2' and 3 are instead multiplied by a higher number density to fit the observations, about the 30% more. This is similar to results obtained by Haus et al. (2013) (who defined the initial cloud model adopted), who retrieved a mode 3 scale factor of 1.5-1.6.

Best fits all over the sample show a result that is in contrast with the generally assumed value of 75% H_2SO_4 solution for the whole cloud layer that is extensively used in literature (Pollack et al., 1993; Zasova et al., 2007; Grassi et al., 2008; Tsang et al., 2008; Bézard et al., 2011; Haus et al., 2014). None of the bins is, in fact, fitted by a synthetic simulation with such an hypothesis. Not only the 75% case but also the pure 84% case has no correspondence with the observations (except for only two cases), and about 8% of the bins are fitted by a mixed cloud 75%/84%. Therefore, the usual assumption of relatively low concentration (75%) is rejected by our analysis. On the contrary, the hypothesis of a stratified cloud with high acid concentration in the bottom layer, up to 96%, is supported (92% of the instances). In particular, the 84%/96% combination results in more than half of the observations. Using the stratified cloud also allowed to adequately fit the left side of the 4.3 μm band which is known to be problematic when the 75% concentration is assumed in the model (Grassi et al., 2014). Pure 96% models represent only a little percentage of the retrieved sample but they are not negligible and outnumber the frequency of conditions with lower uniform concentrations.

The two atmospheric profiles VIRA 30 and VIRA 45 used to model gas absorption are distributed through the sample without an evident latitude separation. The effects due to the differences between the two profiles are too small compared to aerosols effect on radiance; for this reason a pressure-temperature retrieval should be done with a different methodology and for each bin separately.

For the nadir viewing geometry, the effect of changes in both temperature and particle number density of the uppermost layers (from 80 to 100 km altitude) on the radiance spectra is very small all over the VIRTIS spectrum. Variations in radiance from 0.2% to 5% were observed, at least one order of magnitude lower than the effects on radiance due to the cloud parameters, so the actual contribution of the upper atmospheric layer is assumed secondary in the model.

The analysis of VIRTIS nocturnal limb spectra at mesospheric altitudes (70-100 km) for haze characterization is only possible by knowing the incoming nadir radiance in

the haze layer, that is retrieved with the analysis of nadir data. The analysis of limb observations is then performed. Limb data are co-located with the previous nadir data at temporal distance lower than 1 hour. An estimate of the longitudinal shift due to super-rotation is taken into account but a dynamical model would be necessary for an exact co-location. Unfortunately, only 5 orbits have the necessary requirement and the sample is extremely reduced. The analysed limb spectra shows evident features of the typical nadir-viewing spectra up to 87 km, so the scattering haze particles are expected up to that altitude. The same atmospheric and clouds model that produces the best fit for the nadir observations is set in a Monte Carlo model for limb viewing angles. Unfortunately, only the 2.3 µm window is available for the analysis. Longer wavelengths are missing in VIRTIS limb data because the long exposure time saturates the detector and the Monte Carlo model does not allow the computation of wavelengths shorter than 1.2 µm.

The synthetic limb spectra show high radiances and evident clouds features up to 95 km of tangent altitude. On the contrary, VIRTIS data at that altitude show no clouds features at all but only spectral noise and oxygen airglow emission at 1.27 µm and 1.58 µm. At 80 km of tangent altitude VIRTIS data show the typical clouds features due to the scattering of radiance into the line-of-sight by the upper hazes but the Monte Carlo model computes too high radiances even at 80 km compared to VIRTIS observations. Haze particles too large in size or in number density are suggested to explain the model results. With current results, it can be stated that the hazes observed by Wilquet et al. (2009) up to 100 km altitudes at the dayside are not observed in the nightside data at such high altitudes. Three possible explanations are suggested: a gradual sinking of the high atmosphere during the night can be deduced by the oxygen emission (Gérard et al., 2008) and, as a consequence, a sinking of the hazes might happened; the reduced amount of particles could be related with the reduced nocturnal production of sulphuric acid all over the layer, that is mainly a photochemical process; the intrinsic variability of Venus' atmosphere can be responsible for such changes in the observations within different orbits. The explanation might also be a combination of the three hypothesis.

The suggested methodology of co-locating nadir and limb spectra to exploit VIRTIS observation at night at the upper hazes altitudes reveals a satisfactory effectiveness. Unfortunately, suitable data for this kind of retrieval are not so many for VIRTIS. However, the suggested method can be implemented for data analysis of other future missions, not only devoted to Venus. For example, it will be able to be used by the Visible InfraRed Hyperspectral Imaging Spectrometer (VIRHIS) on board the JUpiter ICy moon Explorer (JUICE), scheduled for launch on 2022. The presence of high altitude scattering aerosols in a optically thin atmospheric layer is the only necessary condition for applying the suggested method.

Acronyms

ARS Atmosphere Radiation Spectrum

AU Astronomical Units

CCD Charge Coupled Device

COD Cumulative Optical Depth

DHSU Data Handling and Support Unit

ESA European Space Agency

ESAC European Space Astronomy Centre

ESOC European Space Operations Centre

EUV Extreme UltraViolet

FOV Field of View

FWHM Full Width at Half Maximum

HITEMP HIgh-TEMPerature spectroscopic absorption parameters

HITRAN HIgh-resolution TRANsmission molecular absorption database

HWHM Half Width at Half Maximum

IAPS Istituto di Astrofisica e Planetologia Spaziali

IDL Interactive Data Language

iFOV instantaneous Field of View

ILS Instrumental Line Shape

IR InfraRed

IRFPA InfraRed Focal Plane Array

LCPS large probe cloud particle size spectrometer

LESIA Laboratoire d'Études Spatiales et d'Instrumentation en Astrophysique

LTE Local Thermodynamic Equilibrium

ME Main Electronics Module

MLI Multi-Layer Insulation

MTP Medium Term Plan

NESR Noise Equivalent Spectral Radiance

OM Optics Module

PDS Planetary Data System

PEM Proximity Electronics Modules

ppmv parts per million by volume

SCET SpaceCraft Elapsed Time

SI Système International d'unités

SNR Signal to Noise Ratio

TIPS Total Internal Partition Sum

TOA Top Of the Atmosphere

UTC Universal Time Coordinated

VEx Venus Express

VIRA Venus International Reference Atmosphere

VIRTIS Visible and Infrared Thermal Imaging Spectrometer

VMOC Venus Express Mission Operations Centre

VMR Volume Mixing Ratio

VSOC Venus Express Science Operations Centre

Bibliography

Arnold, G., Haus, R., Kappel, D., Drossart, P., and Piccion, G. (2008). Venus surface data extraction from VIRTIS/Venus Express measurements: Estimation of a quantitative approach. *J. Geophys. Res.*, 113(E00B10). ↑49

Bailey, J., Meadows, V. S., Chamberlain, S., and Crisp, D. (2008). The temperature of the Venus mesosphere from O_2 ($a^1\Delta_g$) airglow observations. *Icarus*, 197:247–259. ↑72

Barstow, J., Tsang, C., Wilson, C., Irwin, P., Taylor, F., McGouldrick, K., Drossart, P., Piccioni, G., and Tellmann, S. (2012). Models of the global cloud structure on Venus derived from Venus Express observations. *Icarus*, 217:542–560. ↑36

Bézard, B., Fedorova, A., Bertaux, J.-L., Rodin, A., and Korablev, O. (2011). The 1.10- and 1.18-µm nightside windows of Venus observed by SPICAV-IR aboard Venus Express. *Icarus*, 216:173–183. ↑38, ↑62, ↑86

Bézard, B., Tsang, C. C. C., Carlson, R. W., Piccioni, G., Marcq, E., and Drossart, P. (2009). Water vapor abundance near the surface of Venus from Venus Express/VIRTIS observations. *J. Geophys. Res.*, 114(E00B39). ↑iv, ↑27, ↑28

Bodhaine, B. A., Wood, N. B., Dutton, E. G., and Slusser, J. R. (1999). On Rayleigh optical depth calculations. *J. Atmos. Ocean. Tech.*, 16:1854–1861. ↑33

Buras, R., Dowling, T., and Emde, C. (2011). New secondary-scattering correction in DISORT with increased efficiency for forward scattering. *J. Quant. Spectrosc. Radiat. Transfer*, 112:2028–2034. ↑47

Cardesin, A. (2008). *VIRTIS-M calibration document. Data calibration process for the Mapping channel of the VIRTIS instrument on Venus-Express.* Doc: VVX-VIR-RP-008, Issue 1. ↑17

de Bergh, C., Moroz, V., Taylor, F., Crisp, D., Bézard, B., and Zasova, L. (2006). The composition of the atmosphere of Venus below 100km altitude: An overview. *Planet. Space Sci.*, 54:1389–1397. ↑23

de Kok, R., Irwin, P., Tsang, C., Piccioni, G., and Drossart, P. (2011). Scattering particles in nightside limb observations of Venus' upper atmosphere by Venus Express VIRTIS. *Icarus*, 211:51–57. ↑1

Devaux, C. and Herman, M. (1975). Venus: Cloud Optical Depth and Surface Albedo from Venera 8. *Icarus*, 24:19–27. ↑49

Drossart, P., Piccioni, G., Gérard, J. C., Lopez-Valverde, M. A., Sanchez-Lavega, A., Zasova, L., Hueso, R., Taylor, F. W., Bézard, B., Adriani, A., Angrilli, F., Arnold, G., Baines, K. H., Bellucci, G., Benkhoff, J., Bibring, J. P., Blanco, A., Blecka, M. I., Carlson, R. W., Coradini, A., Di Lellis, A., Encrenaz, T., Erard, S., Fonti, S., Formisano, V., Fouchet, T., Garcia, R., Haus, R., Helbert, J., Ignatiev, N. I., Irwin, P., Langevin, Y., Lebonnois, S., Luz, D., Marinangeli, L., Orofino, V., Rodin, A. V., Roos-Serote, M. C., Saggin, B., Stam, D. M., Titov, D., Visconti, G., Zambelli, M., Tsang, C., and the VIRTIS Venus Express Technical Team (2007). A dynamic upper atmosphere of Venus as revealed by VIRTIS on Venus Express. *Nature*, 450:641–645. ↑73

Emde, C. and Mayer, B. (2007). Simulation of solar radiation during a total solar eclipse: A challenge for radiative transfer. *Atmos. Chem. Phys.*, 7:2259–2270. ↑78

Erard, S. (2010). *The VIRTIS PDS/IDL software library (lecturePDS)*. Doc: VVX-LES-SW-2264, Issue 2.8.1. ↑16

Erard, S. (2012). *VenusExpress-VIRTIS to Planetary Science Archive Interface Control Document (EAICD)*. European Space Agency, Research and Science Support Department, Planetary Missions Division. Doc: VVX-LES-IC-2269, Issue 1.6. ↑12, ↑16, ↑58

Erard, S. and Garceran, K. (2008). *VIRTIS-VEx geometry files formatting*. Doc: VVX-LES-SW-2268, Issue 1.2. ↑18

Esposito, L. W., Bertaux, J.-L., Krasnopolsky, V., Moroz, V. I., and Zasova, L. V. (1997). Chemistry of the lower atmosphere and clouds. In *Venus II*, pages 415–458. University of Arizona Press. ↑23

Esposito, L. W., Knollenberg, R. G., Marov, M. Y., Toon, O. B., and Turco, R. P. (1983). The clouds and hazes of Venus. In *Venus*, chapter 16, pages 484–564. University of Arizona Press. ↑35

Gao, P., Zhang, X., Crisp, D., Bardeen, C. G., and Yung, Y. L. (2014). Bimodal distribution of sulfuric acid aerosols in the upper haze of Venus. *Icarus*, 231:83–98. ↑35, ↑38

Gérard, J.-C., Saglam, A., Piccioni, G., Drossart, P., Cox, C., Erard, S., Hueso, R., and Sànchez-Lavega, A. (2008). Distribution of the O_2 infrared nightglow observed with VIRTIS on board Venus Express. *Geophys. Res. Lett.*, 35(L02207). ↑72, ↑83, ↑87

Grassi, D., Drossart, P., Piccioni, G., Ignatiev, N. I., Zasova, L. V., Adriani, A., Moriconi, M. L., Irwin, P. G. J., Negrão, A., and Migliorini, A. (2008). Retrieval of air temperature profiles in the Venusian mesosphere from VIRTIS-M data: Description and validation of algorithms. *J. Geophys. Res.*, 113(E00B09). ↑38, ↑62, ↑86

Grassi, D., Politi, R., Ignatiev, N. I., Plainaki, C., Lebonnois, S., Wolkenberg, P., Montabone, L., Migliorini, A., Piccioni, G., and Drossart, P. (2014). The Venus nighttime atmosphere as observed by the VIRTIS-M instrument. Average fields from the complete infrared data set. *J. Geophys. Res. Planets*, 109:837–849. ↑64, ↑86

Hashimoto, G. L. and Sugita, S. (2003). On observing the compositional variability of the surface of Venus using nightside near-infrared thermal radiation. *J. Geophys. Res.*, 108(E9). ↑49

Haus, R. and Arnold, G. (2010). Radiative transfer in the atmosphere of Venus and application to surface emissivity retrieval from VIRTIS/VEX measurements. *Planet. Space Sci.*, 58:1578–1598. ↑23, ↑25, ↑29, ↑36, ↑49, ↑85

Haus, R., Kappel, D., and Arnold, G. (2013). Self-consistent retrieval of temperature profiles and cloud structure in the northern hemisphere of Venus using VIRTIS/VEX and PMV/VENERA-15 radiation measurements. *Planet. Space Sci.*, 89:77–101. ↑27, ↑29, ↑30, ↑36, ↑65, ↑85, ↑86

Haus, R., Kappel, D., and Arnold, G. (2014). Atmospheric thermal structure and cloud features in the southern hemisphere of Venus as retrieved from VIRTIS/VEX radiation measurements. *Icarus*, 232:232–248. ↑35, ↑38, ↑62, ↑86

Ignatiev, N. I., Grassi, D., and Zasova, L. V. (2005). Planetary Fourier spectrometer data analysis: Fast radiative transfer models. *Planet. Space Sci.*, 53:1035–1042. ↑25

James, E. P., Toon, O. B., and Schubert, G. (1997). A Numerical Microphysical Model of the Condensational Venus Cloud. *Icarus*, 129:147–171. ↑51

Kalashnikova, O., Horanyi, M., Thomas, G., and Toon, O. (2000). Meteoric smoke production in the atmosphere. *Geophys. Res. Lett.*, 27:3293–3296. ↑35

Kawabata, K., Coffeen, D. L., Hansen, J. E., Lane, W. A., Sato, M., and Travis, L. D. (1980). Cloud and Haze Properties from Pioneer Venus Polarimetry. *J. Geophys. Res.*, 85(A13):8129–8140. ↑35

Kliore, A. J., Moroz, V. I., and Keating, G. M. (1985). The Venus International Reference Atmosphere. *Adv. Space Res.*, 5:1–305. ↑21

Knollenberg, R. G. and Hunten, D. (1980). The Microphysics of the Clouds of Venus: Results of the Pioneer Venus Particle Size Spectrometer Experiment. *J. Geophys. Res.*, 85(A13):8039–8058. ↑iii, ↑6, ↑35, ↑36, ↑51

Kransopolsky, V. A. (2012). A photochemical model for the Venus atmosphere at 47–112 km. *Icarus*, 218:230–246. ↑23, ↑38

Kuntz, M. (1997). A new implementation of the Humlicek algorithm for the calculation of the Voigt profile function. *J. Quant. Spectrosc. Radiat. Transfer*, 57(6):819–824. ↑27

Maiorov, B. S., Ignatiev, N. I., Moroz, V. I., Zasova, L. V., Moshkin, B. E., Khatuntsev, I. V., and Ekonomov, A. P. (2005). A new analysis of the spectra obtained by the Venera missions in the venusian atmosphere. I. The analysis of the data received from the Venera-11 probe at altitudes below 37 km in the 0.44-0.66 μm wavelength range. *Solar Syst. Res.*, 39(4):267–282. Translated from Astronomicheskii Vestnik, Vol. 39, No. 4, 2005, pp. 304–320. ↑32

Mayer, B. (2009). Radiative transfer in the cloudy atmosphere. *EPJ Web of Conferences*, 1:75–99. ↑78

Mayer, B. and Kylling, A. (2005). Technical note: The libRadtran software package for radiative transfer calculations - description and examples of use. *Atmos. Chem. Phys.*, 5(7):1855–1877. ↑47

Mills, F. P., Esposito, L. W., and Yung, Y. L. (2007). Atmospheric Composition, Chemistry, and Clouds. In *Exploring Venus as a terrestrial planet*, volume 176 of *Geophysical monograph series*, pages 73–100. American Geophysical Union. ↑1, ↑23, ↑35, ↑36, ↑51

Moissl, R. (2008). *Morphology and dynamics of the Venus atmosphere at the cloud top level as observed by the Venus Monitoring Camera*. PhD thesis, Universität Carolo-Wilhelmina zu Braunschweig. ↑69

Moroz, V. I. and Zasova, L. V. (1997). VIRA-2: a review of inputs for updating the Venus International Reference Atmosphere. *Adv. Space Res.*, 19(8):1191–1201. ↑21

Palmer, K. F. and Williams, D. (1975). Optical Constants of Sulfuric Acid; Application to the Clouds of Venus? *Appl. Optics*, 14(1):208–219. ↑38

Peña, O. and Pal, U. (2009). Scattering of electromagnetic radiation by a multilayered sphere. *Comput. Phys. Commun.*, 180:2348–2354. ↑40

Piccioni, G., Drossart, P., Suetta, E., Cosi, M., Ammannito, E., Barbis, A., Berlin, R., Boccaccini, A., Bonello, G., Bouyé, M., Capaccioni, F., Cherubini, G., Dami, M., Dupuis, O., Fave, A., Filacchione, G., Hello, Y., Henry, F., Hofer, S., Huntzinger, G., Melchiorri, R., Parisot, J., Pasqui, C., Peter, G., Pompei, C., Rèess, J., Semery, A., Soufflot, A., the VIRTIS Co-I team: A. Adriani, Angrilli, F., Arnold, G., Baines, K., Bellucci, G., Benkhoff, J., Bézard, B., Bibring, J.-P., Blanco, A., Blecka, M. I., Carlson, R., Coradini, A., di Lellis, A., Encrenaz, T., Erard, S., Fonti, S., Formisano, V., Fouchet, T., Garcia, R., Haus, R., Helbert, J., Ignatiev, N. I., Irwin, P., Langevin, Y., Lebonnois, S., Lopez Valverde, M. A., Luz, D., Marinangeli, L., Orofino, V., Rodin, A. V., Roos-Serote, M. C., Saggin, B., Sanchez-Lavega, A., Stam, D. M., Taylor, F., Titov, D., Visconti, G., and Zambelli, M. (2007). VIRTIS: The Visible and Infrared Thermal Imaging Spectrometer. Special publication SP 1295, ESA. ↑12, ↑17

Piccioni, G., Zasova, L., Migliorini, A., Drossart, P., Shakun, A., Muñoz, A. G., Mills, F. P., and Cardesin-Moinelo, A. (2009). Near-IR oxygen nightglow observed by VIRTIS in the Venus upper atmosphere. *J. Geophys. Res.*, 114(E00B38). ↑72

Politi, R., Piccioni, G., Henry, F., Erard, S., Jacquinod, S., and Drossart, P. (2014). *VIRTIS-VEX data manual*. ↑16

Pollack, J. B., Dalton, J. B., Grinspoon, D., Wattson, R. B., Freedman, R., Crisp, D., Allen, D. A., Bézard, B., DeBergh, C., Giver, L. P., Ma, Q., and Tipping, R. (1993). Near-infrared light from Venus' nightside: A spectroscopic analysis. *Icarus*, 103:1–42. ↑24, ↑36, ↑38, ↑54, ↑62, ↑65, ↑85, ↑86

Reess, J. M. and Henry, F. (2008). *VIRTIS-H calibration*. Doc: VVX-LES-RP-2333, Issue 1.4. ↑17

Rothman, L. S., Gordon, I. E., Babikov, Y., Barbe, A., Benner, D. C., Bernath, P. F., Birk, M., Bizzocchi, L., Boudon, V., Brown, L. R., Campargue, A., Chance, K., Cohen, E. A., Coudert, L. H., Devi, V. M., Drouin, B. J., Fayt, A., Flaud, J.-M., Gamache, R. R., Harrison, J. J., Hartmann, J.-M., Hill, C., Hodges, J. T., Jacquemart, D., Jolly, A., Lamouroux, J., Roy, R. J. L., Li, G., Long, D. A., Lyulin, O. M., Mackie, C. J., Massie, S. T., Mikhailenko, S., Müller, H. S. P., Naumenko, O. V., Nikitin, A. V., Orphal, J., Perevalov, V., Perrin, A., Polovtseva, E. R., Richard, C., Smith, M. A. H., Starikova, E., Sung, K., Tashkun, S., Tennyson, J., Toon, G. C., Tyuterev, V. G., and Wagner, G. (2013). The HITRAN 2012 molecular spectroscopic database. *J. Quant. Spectrosc. Radiat. Transfer*, 130:4–50. ↑23

Rothman, L. S., Gordon, I. E., Barber, R. J., Dothe, H., Gamache, R. R., Goldman, A., Perevalov, V. I., Tashkun, S. A., and Tennyson, J. (2010). HITEMP, the high-temperature molecular spectroscopic database. *J. Quant. Spectrosc. Radiat. Transfer*, 111:2139–2150. ↑24

Rothman, L. S., Jacquemart, D., Barbe, A., Benner, D. C., Birk, M., Brown, L., Carleer, M., Chackerian Jr., C., Chance, K., Coudert, L. H., Dana, V., Devi, V. M., Flaud, J.-M., Gamache, R. R., Goldman, A., Hartmann, J.-M., Jucks, K. W., Maki, A. G., Mandin, J.-Y., Massie, S. T., Orphal, J., Perrin, A., Rinsland, C. P., Smith, M. A. H., Tennyson, J., Tolchenov, R. N., Toth, R. A., Auwera, J. V., Varanasi, P., and Wagner, G. (2005). The HITRAN 2004 molecular spectroscopic database. *J. Quant. Spectrosc. Radiat. Transfer*, 96:139–204. ↑25

Schofield, J. T. and Taylor, F. W. (1983). Measurements of the mean, solar-fixed temperature and cloud structure of the middle atmosphere of Venus. *Q. J. Roy. Meteor. Soc.*, 109:57–80.

Seiff, A. (1983). Thermal structure of the atmosphere of Venus. In *Venus*, pages 215–279. University of Arizona Press.

Seiff, A., Schofield, J. T., Kliore, A. J., Taylor, F. W., Limaye, S. S., Revercomb, H. E., Sromovsky, L. A., Kerzhanovich, V. V., Moroz, V. I., and Marov, M. Y. (1985). Models of the structure of the atmosphere of Venus from the surface to 100 kilometers altitude. *Adv. Space Res.*, 5(11):3–68. ↑21, ↑85

Shettle, E. P. and Volz, F. E. (1976). Optical constants for meteoric dust aerosol models, in Atmospheric Aerosols: Their Optical Properties and Effects. A Topical Meeting on Atmospheric Aerosols sponsored by the Optical Society of America and NASA Langley Research Center, Williamsburg, VA, 13-15 Dec. 1976. NASA Conference Publication CP 2004. ↑38

Simečková, M., Jacquemart, D., Rothman, L. S., Gamache, R. R., and Goldman, A. (2006). Einstein A-coefficients and statistical weights for molecular absorption transitions in the HITRAN database. *J. Quant. Spectrosc. Radiat. Transfer*, 98(1):130–155. ↑25

Stamnes, K., Tsay, S.-C., Wiscombe, W., and Jayaweera, K. (1988). Numerically stable algorithm for discrete–ordinate–method radiative transfer in multiple scattering and emitting layered media. *Appl. Optics*, 27:2502–2509. ↑47

Stamnes, K., Tsay, S.-C., Wiscombe, W., and Laszlo, I. (2000). DISORT, a General-Purpose Fortran Program for Discrete-Ordinate-Method Radiative Transfer in Scattering and Emitting Layered Media: Documentation of Methodology. Technical report, Department of physics and engineering physics, Stevens Institute of Technology, Hoboken. ↑47

Takagi, S., Mahieux, A., Wilquet, V., Robert, S., Drummond, R., Vandaele, A. C., and Iwagami, N. (2014). Study of the Venus upper haze. Presented at Japan Geoscience Union Meeting 2014 in Pacifico YOKOHAMA, 28th April - 2nd May 2014. ↑1

Tonkov, M. V., Filippov, N. N., Bertsev, V. V., Bouanich, J. P., Van-Thanh, N., Brodbeck, C., Hartmann, J. M., Boulet, C., Thibault, F., and Doucen, R. L. (1996). Measurements and empirical modeling of pure CO_2 absorption in the 2.3-μm region at room temperature: Far wings, allowed and collision-induced bands. *Appl. Optics*, 35(24):4863–4870. ↑iv, ↑27, ↑28

Tran, H., Boulet, C., Stefani, S., Snels, M., and Piccioni, G. (2011). Measurements and modelling of high pressure pure CO_2 spectra from 750 to 8500 cm^{-1}. I–central and wing regions of the allowed vibrational bands. *J. Quant. Spectrosc. Radiat. Transfer*, 112:925–936. ↑27, ↑29

Tsang, C. C. C., Irwin, P. G. J., Taylor, F. W., and Wilson, C. F. (2008). A correlated-k model of radiative transfer in the near-infrared windows of Venus. *J. Quant. Spectrosc. Radiat. Transfer*, 109:1118–1135. ↑36, ↑38, ↑62, ↑86

Wilquet, V., Drummond, R., Mahieux, A., Robert, S., Vandaele, A. C., and Bertaux, J.-L. (2012). Optical extinction due to aerosols in the upper haze of Venus: Four years of SOIR/VEX observations from 2006 to 2010. *Icarus*, 217(2):875–881. ↑1

Wilquet, V., Fedorova, A., Montmessin, F., Drummond, R., Mahieux, A., Vandaele, A., Villard, E., Korablev, O., and Bertaux, J.-L. (2009). Preliminary characterization of the upper haze by SPICAV/SOIR solar occultation in UV to mid-IR onboard Venus Express. *J. Geophys. Res.*, 114(E00B42). ↑1, ↑36, ↑57, ↑83, ↑85, ↑87

Winters, B. H., Silverman, S., and Benedict, W. S. (1964). Line shape in the wing beyond the band head of the 4.3 μm band of CO_2. *J. Quant. Spectrosc. Radiat. Transfer*, 4:527–537. ↑27

Yamamoto, M. and Takahashi, M. (2003). The Fully Developed Superrotation Simulated by a General Circulation Model of a Venus-like Atmosphere. *J. Atmos. Sci.*, 60:561–574. ↑69

Zasova, L. (2012). Reference atmospheres: VIRA II -Venus International Reference Atmosphere update. In *39th COSPAR Scientific Assembly*, volume 39 of *COSPAR Meeting*, page 2248. ↑21

Zasova, L., Ignatiev, N., Khatuntsev, I., and Linkin, V. (2007). Structure of the Venus atmosphere. *Planet. Space Sci.*, 55:1712–1728. ↑35, ↑36, ↑38, ↑44, ↑62, ↑86